学位論文（要約）

Two-Dimensional Superconductivity

in Layered R_2O_2Bi (R: Rare Earth) with Bi^{2-} Square Net

（Bi^{2-} 正方格子を持つ層状化合物 R_2O_2Bi (R: 希土類) における
2 次元超伝導）

平成 28 年 12 月博士（理学）申請

東京大学大学院理学系研究科

化学専攻

清　良輔

Two-Dimensional Superconductivity in Layered R_2O_2Bi (R: Rare Earth) with Bi^{2-} Square Net

by

Ryosuke Sei

Department of Chemistry

Graduate School of Science

The University of Tokyo

December, 2016

Abstract

Bi square net compound is a promising platform to investigate the interaction between two-dimensional electronic nature and strong spin-orbit coupling. Layered $AM\mathrm{Bi}_2$ compounds (A: alkaline earth and rare earth, M: metal elements) with Bi^- square net have been extensively studied until today, leading to the emergence of the wide variety of quantum phenomena such as anisotropic Dirac fermion and Kondo lattice behavior, while superconducting Bi^- square net has not been realized yet. In contrast to the rich material group of Bi^- square net compounds, there are few reports about the synthesis of Bi^{2-} square net compounds except for $\mathrm{ThCr_2Si_2}$-type $R_2\mathrm{O_2Bi}$ (R: rare earth) in polycrystalline form, where only metal-to-insulator transition and antiferromagnetic ordering of R cations were reported so far. Therefore, detailed physical properties of Bi^{2-} square net is not fully understood despite the possible emergence of various attractive properties.

In this thesis, fascinating properties of Bi^{2-} square net in $R_2\mathrm{O_2Bi}$ compounds were explored via two approaches: the fabrication of epitaxial thin films and the synthesis of bulk polycrystalline powders. In thin film study, I succeeded in the fabrication of $\mathrm{Y_2O_2Bi}$ epitaxial thin films for the first time by developing two novel solid-phase epitaxy techniques, leading to the observation of intrinsic two-dimensional electronic nature. In the study about polycrystalline powders, I discovered two-dimensional superconductivity of Bi^{2-} square net in $R_2\mathrm{O_2Bi}$.

Single crystalline samples were desired to investigate the intrinsic properties of $R_2\mathrm{O_2Bi}$ rather than polycrystalline powder specimen presently available. In this thesis, $\mathrm{Y_2O_2Bi}$ epitaxial thin films were successfully obtained by developing two solid-phase epitaxy techniques: reductive solid-phase epitaxy utilizing direct reaction between (Y,Bi) mixed powders and $\mathrm{Y_2O_3}$ amorphous thin film, and multilayer solid-phase epitaxy utilizing subnanometer thick [$\mathrm{Bi/Y/Y_2O_3}$] multilayer precursor film. In both techniques,

the reduction of Bi by strong reductant Y was essential to achieve Y_2O_2Bi phase. This concept would be applicable to the epitaxial growth of not only other R_2O_2Bi compounds but also analogous layered compounds. The detailed electrical transport properties were evaluated for Y_2O_2Bi epitaxial thin film. The film showed weak anti-localization effect and two-fold symmetric angular dependent magnetoresistance. These results demonstrated the interaction between two-dimensional electronic state and strong spin-orbit coupling in Bi^{2-} square net, similar to the topological insulator which is an innovative spintronic material. Furthermore, the onset of superconductivity was observed in several samples. However, both Meissner effect and zero resistance were not obtained probably due to very small superconducting volume fraction.

According to the results about Y_2O_2Bi epitaxial thin film, polycrystalline Y_2O_2Bi samples were synthesized by varying the nominal amount of O in starting materials. As a result, abrupt *c*-axis expansion was observed only for the samples with high O content in contrast with constant *a*-axis length among all samples. This result suggested O incorporation between Bi^{2-} square net and adjacent Y termination layer in *c*-axis expanded samples. Notably, both Meissner effect and zero-resistance were observed only for the samples with high O content, indicating bulk superconductivity. This new layered superconductor showed Berezinskii-Kosterlitz-Thouless transition, indicating two-dimensional nature of the superconductivity. This was the first observation of superconducting Bi square net. Notably, the superconductivity in Y_2O_2Bi emerged concomitantly with the abrupt expansion of *c*-axis length, i.e., expansion of Bi internet distance. This result indicates that the superconductivity in Y_2O_2Bi was induced by enhancing two-dimensionality of Bi^{2-} square net. Such nonstoichiometric atom incorporation into hidden interstitial site could be a new methodology to induce superconductivity in layered compounds.

Furthermore, the superconductivity was also observed in other R_2O_2Bi (*R*: Tb, Dy, and Lu) by same driving force: enhanced two-dimensionality of Bi^{2-} square net via O incorporation was crucial to induce the superconductivity. Notably, complex phase competition among the superconductivity, antiferromagnetic ordering, and charge density wave was observed in Tb_2O_2Bi, indicating unusual mechanism of the superconductivity in Bi^{2-} square net. The universal superconductivity with rich electronic phases depending

on R in R_2O_2Bi indicates that R_2O_2Bi would provide intriguing platform to investigate the interplay between two-dimensional superconductivity and strong spin-orbit coupling.

In conclusion, I established the novel routes to investigate the physical properties of Bi^{2-} square net in R_2O_2Bi compounds. According to these techniques, I clarified the rich electronic phenomena of Bi^{2-} square net such as universal two-dimensional superconductivity and similar electronic nature to the topological insulator. These findings indicate that R_2O_2Bi was the model compound to investigate the peculiar phenomena of Bi^{2-} square net. Furthermore, obtained concepts such as two solid-phase epitaxy techniques and structural control via O incorporation would provide the insight for exploring physical properties of layered compounds.

Contents

Chapter 1

General introduction

1.1 Layered superconductors

Since the discovery of high temperature superconductivity in cuprates [1], naturally and artificially layered compounds have attracted great interest to induce fascinating superconductivity with high transition temperature and unconventional pairing mechanisms. Extensive studies have developed this field deeper and wider, resulting in the discovery of a wide variety of novel layered superconductors such as ruthenates, nitride chlorides, $LaAlO_3/SrTiO_3$ heterostructures, and Fe-based superconductors [2–6]. In this section, I introduce the properties of layered superconductors, especially the cuprate and Fe-based high temperature superconductors.

1.1.1 High temperature superconductors

The most famous and intriguing nature in layered superconductors is the high transition temperature observed in cuprates and Fe-based compounds. These compounds are composed of two-dimensional building blocks such as superconducting layer and blocking layer. The latter has large flexibility of crystal structures and constituent elements, enabling to engineer the various materials and transition temperatures.

Figure 1.1 shows the crystal structures of mother compounds of well-known cuprate superconductors: La_2CuO_4, $YBa_2Cu_3O_7$, and $Bi_2Sr_2CaCu_2O_8$. All compounds possess two-dimensional square CuO_2 sheet showing superconductivity with various block-

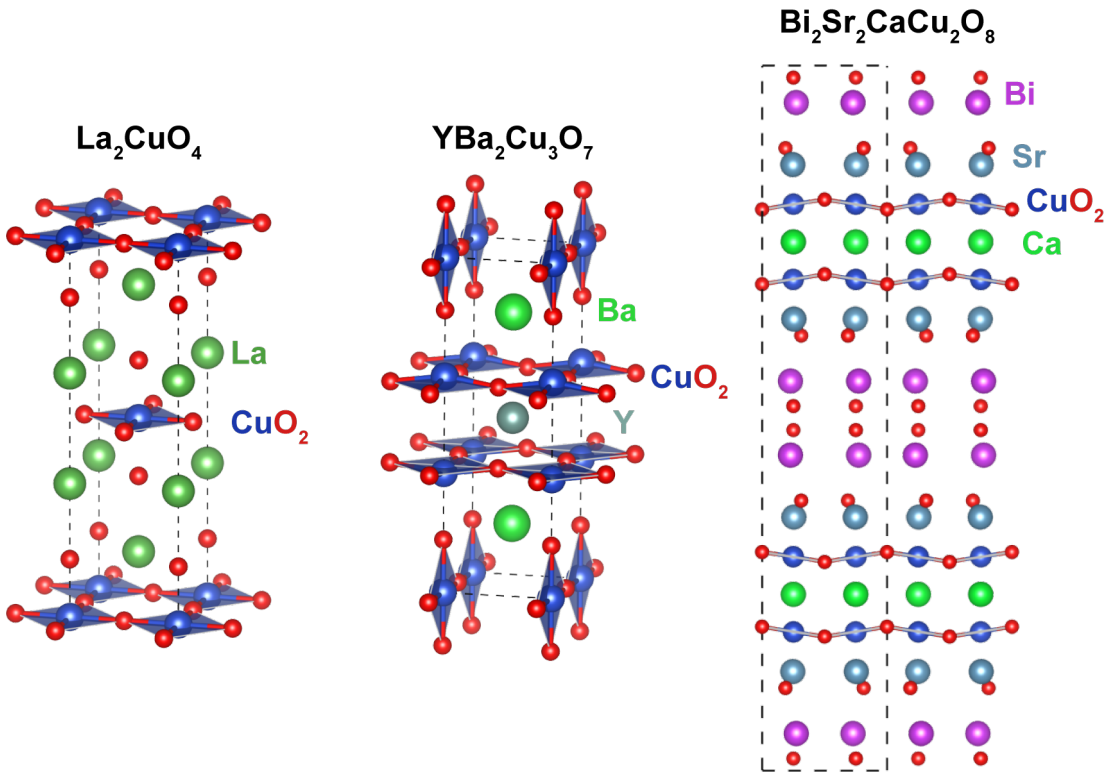

Figure 1.1: Crystal structures of mother compounds of cuprate superconductors. Broken lines denote unit cells. In this thesis, the crystal structures were drawn by VESTA [7].

ing layers. La_2CuO_4 was a first series of high temperature superconductors reported in 1986 [1] and T_c rose to around 36 K in $La_{1.8}Sr_{0.2}CuO_4$ [8]. $YBa_2Cu_3O_7$ is the first superconductor possessing higher T_c of 93 K than boiling point of liquid N_2 [9]. Bismuth-strontium-calcium-copper oxide compounds can be represented by chemical formula $Bi_2Sr_2Ca_{n-1}Cu_nO_{2n+4}$ [10]. These compounds have large blocking layers and T_c increased over 100 K for $n = 3$. These superconductors are the promising materials for the future application to transmission cables without energy loss, superconducting maglev, and so on.

Another family of high temperature superconductor is the Fe-based compounds (Fig. 1.2). First reported compound is $LaFeAsO_{1-x}F_x$ with T_c of 26 K [6]. In this compound, PbO-type FeAs layer composed of edge sharing $FeAs_4$ tetrahedron becomes superconducting, and T_c increases over 50 K by substiution of rare earth elements [11]. The Fe-based superconductors also form a wide group of materials by converting the crystal structure of blocking layer such as $BaFe_2As_2$ (T_c = 38 K) [12] and LiFeAs (T_c = 18 K) [13]. Furthermore, iso-structural layered iron chalcogenides like FeSe also

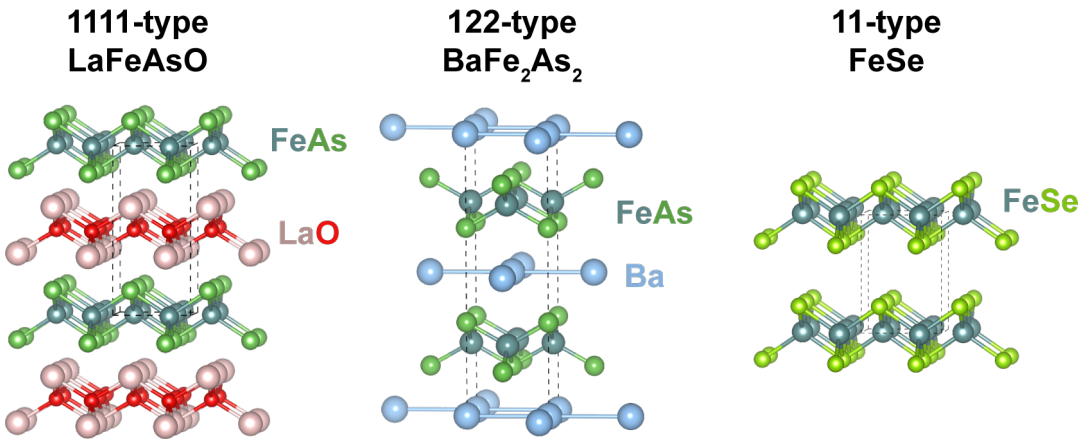

Figure 1.2: Crystal structures of mother compounds of Fe-based superconductors. Broken lines denote unit cells.

become superconducting (T_c = 8 K) [14].

1.1.2 Two-dimensional superconductivity

Layered superconductors own two-dimensional electronic nature. This leads to the novel properties, e.g. different upper critical fields between parallel and perpendicular directions of applied magnetic fields to superconducting layer [2].

One characteristic phenomenon in two-dimensional superconductor is the Berezinskii-Kosterlitz-Thouless (BKT) transition, clearly observed at the superconducting oxide interface in $LaAlO_3/SrTiO_3$ heterostructure [5]. In the two-dimensional superconducting system, vortex-antivortex pairs form the ionic-like lattice, and melt at characteristic BKT transition temperature (T_{BKT}). This behavior appear as $V \propto I^{\alpha}$ law in voltage-current characteristics where α turns from 1 (ohmic law) above T_c to 3 at T_{BKT} and more by decreasing temperature (Fig. 1.3a,b) [15, 16]. The T_{BKT} is independently derived from electrical resistivity (Fig. 1.3c) [17]. These separately derived temperatures show a same value, proving the BKT transition. This transition is also observed in both cuprate and Fe-based superconductors [18–21], confirming two-dimensional electronic nature and weak inter-layer interaction of layered superconductors.

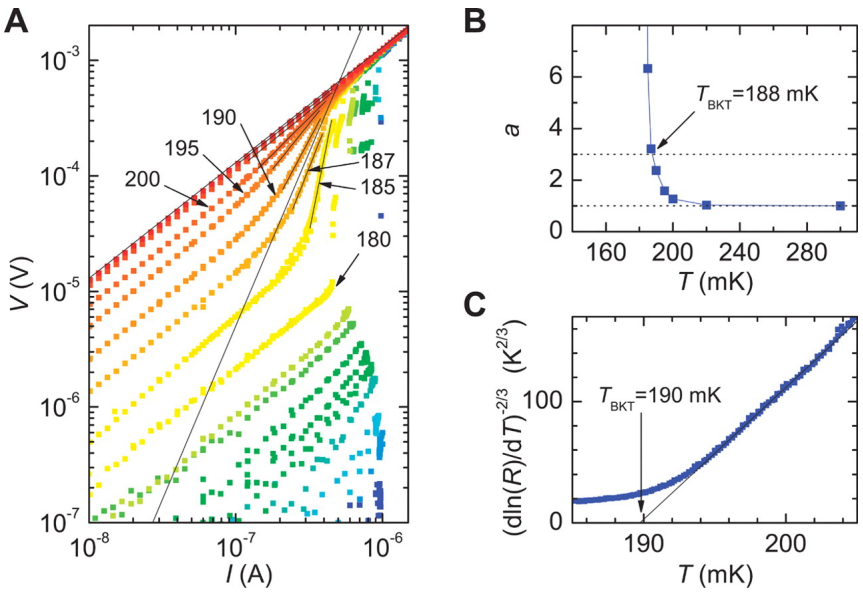

Figure 1.3: (a) Voltage-current characteristics of $LaAlO_3/SrTiO_3$ heterostructure around T_c. (b) Temperature dependence of exponent α. (c) Temperature dependence of $(\mathrm{d}\ln R/\mathrm{d}\ T)^{-2/3}$. Reprinted with permission from [5]. Copyright 2007 by American Association for the Advancement of Science.

1.1.3 Complex phase diagram

Figure 1.4a shows a schematic image of typical superconducting phase diagram in cuprate superconductors [2]. The mother compounds are antiferromagnetic (AF) Mott insulator. By introducing carriers into the CuO_2 plane, the long-range AF ordering is weakened and breaks resulting in the emergence of superconductivity. It is considered that this AF interaction is the driving force of Cooper pairing with *d*-wave symmetry in stark contrast to that by electron-phonon coupling in BCS-type *s*-wave superconductors [22]. However, recent studies report the competition between superconductivity and charge density wave order indicating the presence of strong electron-phonon coupling [23, 24]. These results complicate the elucidation of superconducting mechanism of cuprates. Fe-based superconductors also show the complex phase competition among superconductivity, antiferromagnetism with spin density wave, and structural transition, although detailed superconducting mechanism is still unclear [25, 26].

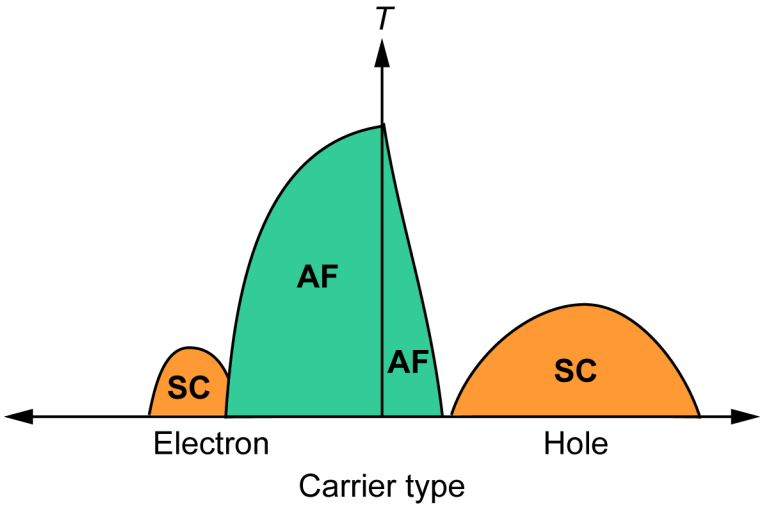

Figure 1.4: Schematic images of superconducting phase diagram for cuprates. SC and AF denote superconducting and antiferromagnetism, respectively [2].

1.1.4 Schemes to search novel layered superconductors

There are few layered compounds which show the superconductivity as its stoichiometric composition and at ambient pressure, so that carrier doping and applying pressure are widely utilized to induce the superconductivity [2]. The carrier doping techniques mainly have two approarches: alio-valent ion substitution and ionic intercalation into van del Waals gap (Fig. 1.5). Generated carriers due to charge neutrality are injected into conductive layer, changing temperature dependence of electrical resistivity (ρ-T curve) from insulating to superconducting behavior in $La_{2-x}Sr_xCuO_4$ (Fig. 1.6 left) [27]. The high pressure environment is generally realized by the diamond anvil cell up to over 700 GPa maximum [28], also resulting in the emergence of superconductivity (Fig. 1.6 right) [29].

Exploring iso-structural compounds of layered superconductors is one promising strategy to discover novel superconductors. For example, Sr_2RuO_4 has a same structure to La_2CuO_4 with quite low T_c of around 1.5 K. This compound is considered to possess spin-triplet Cooper pairing with p-wave symmetry, which will induce exotic quantum phenomena [3]. Furthermore, the exploration of the layered compounds structurally similar to Fe-based superconductors develops the generation of large variety of superconducting family such as layered Ti_2O-based and BiS_2-based superconductors [26].

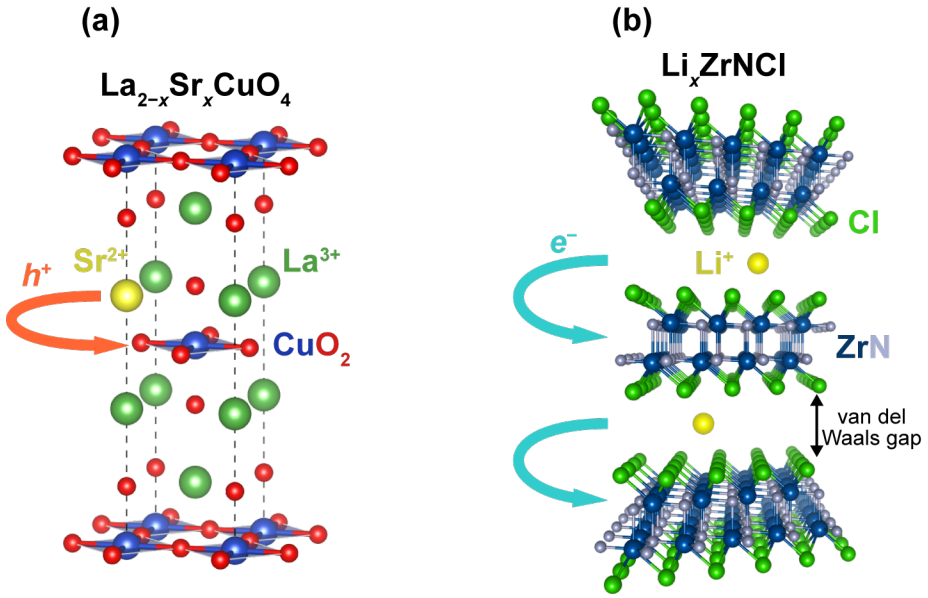

Figure 1.5: Schematic images of carrier doping techniques: (a) alio-valent ion substitution and (b) ionic intercalation into van del Waals gap.

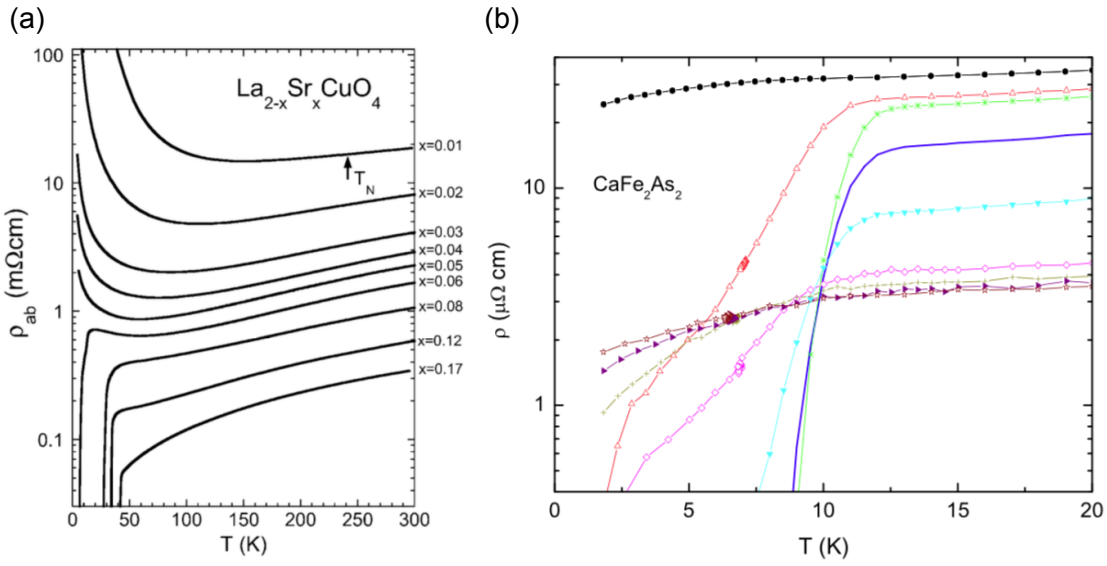

Figure 1.6: (a) The ρ-T curves of $La_{2-x}Sr_xCuO_4$ with various x (left). Reprinted with permission from [27]. Copyright 2001 by American Physical Society. (b) The ρ-T curves of $CaFe_2As_2$ under pressure at 0, 2.3, 3.5, 5.1, 5.5, 8.6, 12.7, 16.8, and 19.3 kbar. Reprinted with permission from [29]. Copyright 2008 by American Physical Society.

1.1.5 Superconductivity in strong spin-orbit coupled system

In the field of condensed matter physics, topological insulator has attracted much attention for these ten years, which is a bulk insulator but possessing conductive edge/surface state with linear band dispersion called Dirac cone [30]. The completely spin-polarized mass-less carriers can propagate at this edge/surface state without any back-scattering effects, connecting to the emergence of novel quantum phenomena like quantum spin Hall effect and the application to innovative energy-saving spintronics devices. Strong spin-orbit coupling is the driving force to emerge this new quantum state of matter, so that layered Bi compounds, especially layered Bi_2Se_3 composed of Se-Bi-Se-Bi-Se quintuple layers (Fig. 1.7), have been extensively studied to investigate the intriguing properties in topological insulators [30–32].

In 2010, the emergence of superconductivity was reported in electron doped Bi_2Se_3 via Cu intercalation into van del Waals gap (Fig. 1.7) [33]. This novel layered superconductors are now considered as a model compound of topological superconductivity which will generate Majorana fermions at its surface state connecting to the ultra high speed quantum computing [31,34]. However, relatively low sample quality of superconducting $Cu_xBi_2Se_3$ such as small superconducting volume fraction and generation of by-products hampers detailed evaluation of physical properties in spite of the many extensive works to achieve good sample quality [33–37]. This indicates that the searching novel candidates

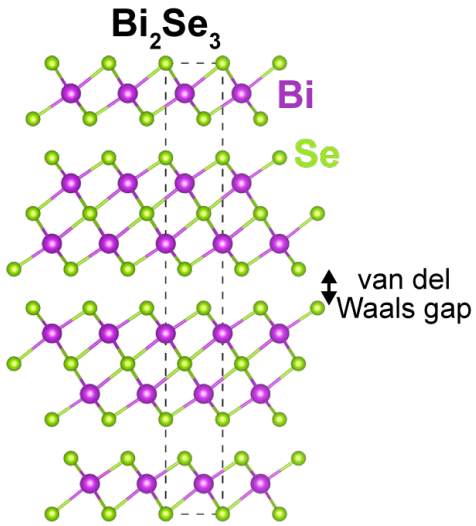

Figure 1.7: A crystal structures of Bi_2Se_3. Broken lines denote unit cells.

of topological superconductors is quite meaningful issue to investigate the interaction between (quasi) two-dimensional superconductivity and strong spin-orbit coupling in both fundamental and practical aspects.

1.2 Bi square net compounds

Bi is a heavy semimetal element whose atomic number is 83 possessing the strong spin-orbit coupling. The electronic configuration of Bi is [Xe]$4f^{14}5d^{10}6s^26p^3$, so that Bi generally possesses +5, +3, and −3 valent state with various local structures in compounds. For example, elemental Bi forms buckled honeycomb lattice [38], and Bi^{3+} and Bi^{5+} form octahedra with anions such as BiO_6 in $BaBiO_3$ [39] and $BiSe_6$ in Bi_2Se_3 [33], respectively. Bi^{3-} anions can be realized by the coexistence of highly electro-positive elements such as alkaline earth and rare earth, forming the complicated polyhedra with these cations [40]. Notably, Bi can form the monatomic square net structure with incomplete filled electron shell such as Bi^- state and unusually reductive Bi^{2-} state. This section reviews the fascinating properties of Bi square net compounds.

1.2.1 Crystal structure

There are mainly two types of Bi square net compounds whose chemical formulas are represented by $AMBi_2$ (A: alkaline earth and rare earth, M: metal element) and R_2X_2Bi (R: rare earth and actinoid, X: O and N) [40, 41]. The former possesses a Bi^- square net in stark contrast to an unusual Bi^{2-} square net in the latter.

There is a large variety of $AMBi_2$ compounds because of the flexibility of the combination between A and M. Figure 1.8 shows crystal structures of $AMBi_2$ compounds which can be further classified into two structures: $ZrCuSi_2$-type (space group: *P4/nmm*) and $SrZnBi_2$-type (*I4/mmm*) [40, 42]. In both structures, the Bi^- square net is separated from edge sharing MBi_4 tetrahedra slab (same as PbO-type structure) by the interstitial A metals, and the classification is originating from the different arrangement of A atoms adjacent to Bi^- square net (bottom of Fig. 1.8), resulting in the double sized unit cell in $SrZnBi_2$-type structure. The compounds' list of these structure types are summarized in Table 1.1. It seems that several compounds such as $RNiBi_2$ and $RPdBi_2$ show the

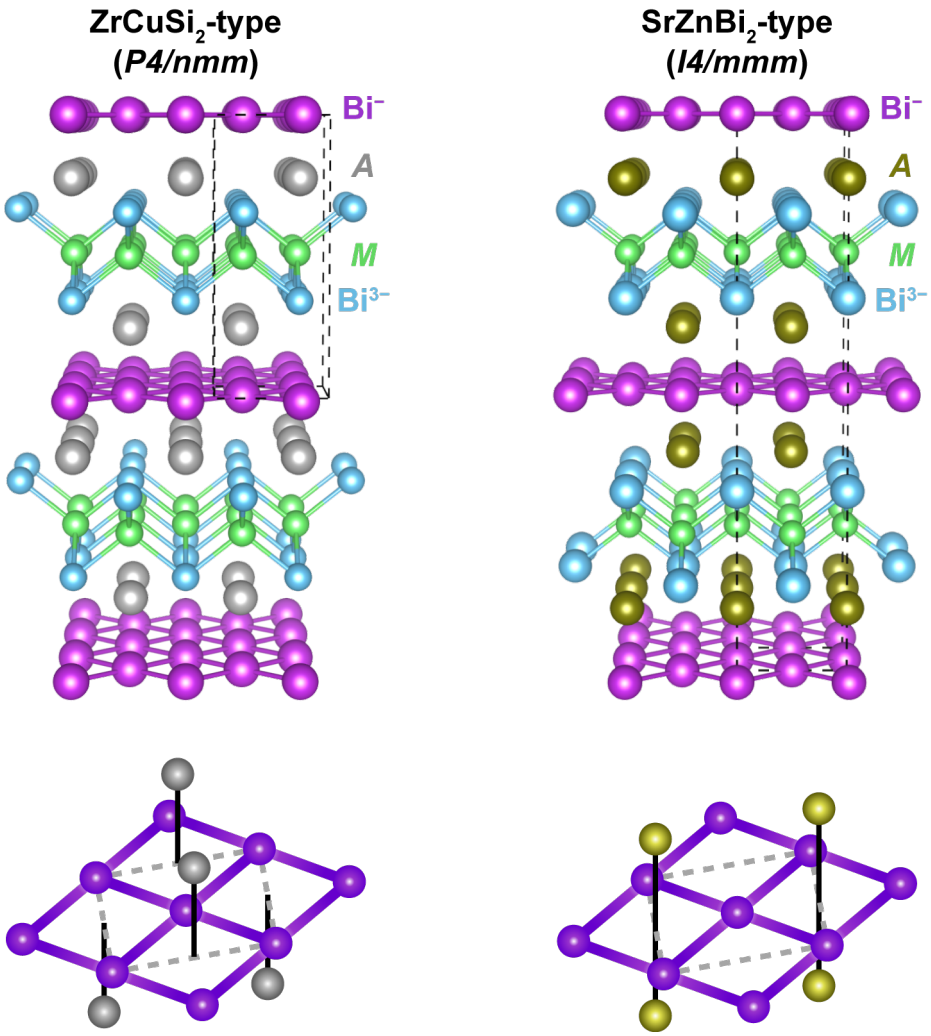

Figure 1.8: Crystal structures of $ZrCuSi_2$-type (left) and $SrZnBi_2$-type (right) $AMBi_2$ compounds. Broken lines denote unit cells. Bottoms show the local crystal structures around Bi^- square net.

Table 1.1: Crystal structure of $AMBi_2$ compounds with Bi^- square net (R: rare earth)

Structure	Compounds
$ZrCuSi_2$ (*P4/nmm*)	$CaMnBi_2$ [43], $YbMnBi_2$ [44], $LaLiBi_2$ [45], $RNiBi_2$ [46], $RPdBi_2$ [47], $RCuBi_2$ [48], $RAgBi_2$ [49], $RAuBi_2$ [50], $RZnBi_2$ [51]
$SrZnBi_2$ (*I4/mmm*)	$SrMnBi_2$, $BaMnBi_2$ [52], $EuMnBi_2$ [53], $CeGeBi_2$ [40], $BaZnBi_2$, $SrCdBi_2$, $BaCdBi_2$ [54]

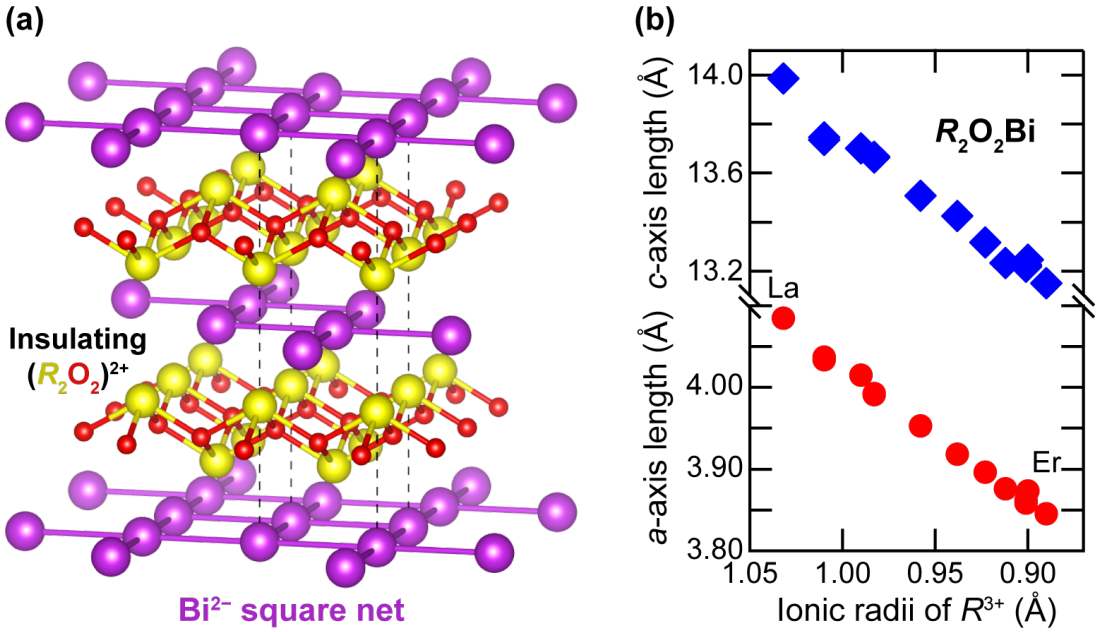

Figure 1.9: (a) Crystal structure of $ThCr_2Si_2$-type R_2O_2Bi. Broken line denotes unit cell. (b) Lattice constant variation of R_2O_2Bi. Structural data refers to [41, 57–59].

intrinsic defect in M site, so that they are often represented as $AM_{1-x}Bi_2$ [46, 47].

In contrast to a large variation of Bi^- square net compounds, there are a few reports of Bi^{2-} square net compounds: Ac_2N_2Bi (Ac: Th, U, Am, Cm) [55, 56] and R_2O_2Bi (R: rare earth) [41, 57–59]. Both groups have anti-$ThCr_2Si_2$-type structure composed of $[R_2O_2]^{2+}$ (or $[Ac_2N_2]^{2+}$) slab with PbO-type structure and Bi^{2-} square net (Fig. 1.9a). Here, "anti-" means that the positions of anions and cations are inverted from normal $ThCr_2Si_2$-type compounds, e.g. $BaFe_2As_2$ high temperature superconductor. The space group is *I4/mmm*. The Bi^{2-} square net is rotated by 45° on PbO-type layer compared with the Bi^- square net in $AMBi_2$. Figure 1.9b shows lattice constants plotted as a function of ionic radii of R^{3+} [60] in R_2O_2Bi reported in previous studies [41, 57–59]. The lattice constants show systematical variation according to the lanthanoid contraction, evidencing the R^{3+} state which indirectly confirms highly reductive Bi^{2-} state. Furthermore, larger Bi–Bi bond length in Bi^{2-} square net, i.e. a-axis length, than that in Bi^- square net (~3.2 Å) [58] also supports Bi^{2-} state as discussed later.

The multinary compounds composed of electropositive elements (e.g. alkaline earth and rare earth) and electronegative elements (e.g. group 13–16 elements) are called as Zintl phase where the former donates their electrons to the latter [61, 62]. Each

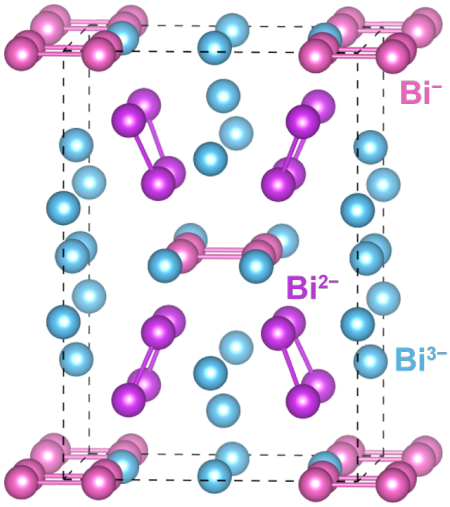

Figure 1.10: Bi framework in $Ca_{11}Bi_{10}$. Ca cations are not shown here. Broken line denotes unit cell.

electronegative element forms cluster structure according to the octet rule, so that Bi anions generally form the following frameworks: isolated square or zig-zag chain for Bi^{-}, dimer for Bi^{2-}, and isolated atom for Bi^{3-}. One typical example is $Ca_{11}Bi_{10}$ [63] whose charges of each element are assigned as $(Ca^{2+})_{22}(Bi^{-})_4(Bi^{2-})_8(Bi^{3-})_8$, where four Bi^{-} anions form one isolated square, eight Bi^{2-} anions form four dimers, and eight Bi^{3-} anions are isolated (Fig. 1.10). Both $AMBi_2$ and R_2O_2Bi compounds are considered as a kind of Zintl phase, while a monatomic Bi square net layer cannot be explained by semiclassical Zintl concept.

These nonclassical structures can be explained by introducing the hypervalent bonding rule [62]. The simplest example is Bi_3^{7-} forming a linear trimer, whose electronic configuration is equal to typical hypervalent product I_3^{-}. By assuming the bonding axis along x direction, there are four electrons in three Bi p_x orbitals with fully occupied s, p_y, and p_z orbitals (Fig. 1.11a). These electrons occupy only bonding and non-bonding molecular orbitals, resulting in the formation of Bi_3^{7-} linear trimer. Increase of the number of Bi atoms leads to the formation of $Bi_n^{(2n+1)-}$ linear chain (Fig. 1.11a), converging to one-dimensional Bi^{2-} linear chain structure in the crystal ($n \to \infty$). The next step is the formation of Bi square net by considering the array of one-dimensional Bi^{2-} linear chain along y direction (Fig. 1.11b). In order to make Bi–Bi bond between filled p_y orbitals of Bi^{2-} anions, it is necessary to remove one electron per one Bi^{2-} anion, resulting in two-dimensional Bi^{-} square network. Therefore, only Bi^{-} anions

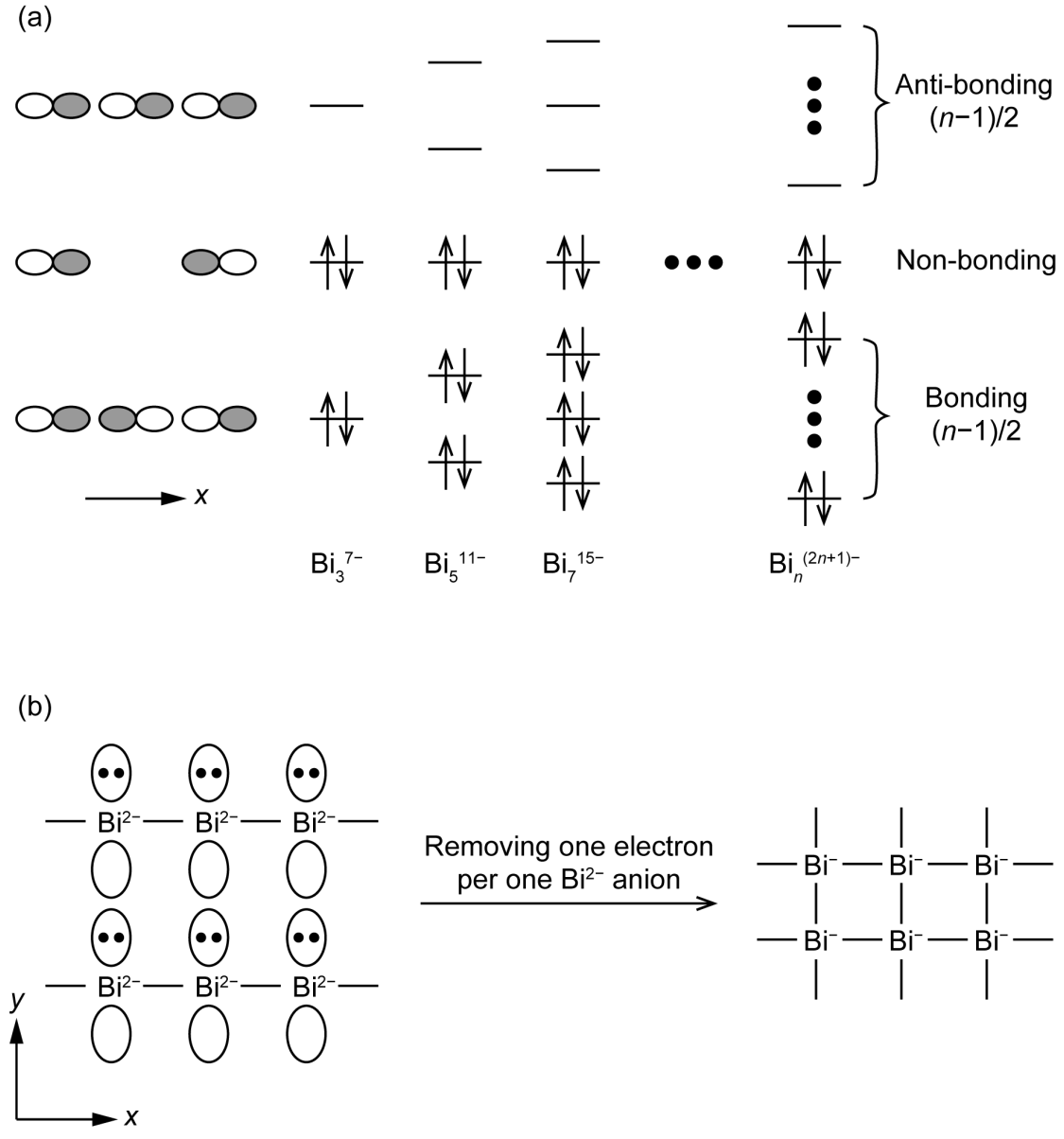

Figure 1.11: Hypervalent bonding rule to form (a) one-dimensional Bi^{2-} linear chain and (b) two-dimensional Bi^{-} square net [62].

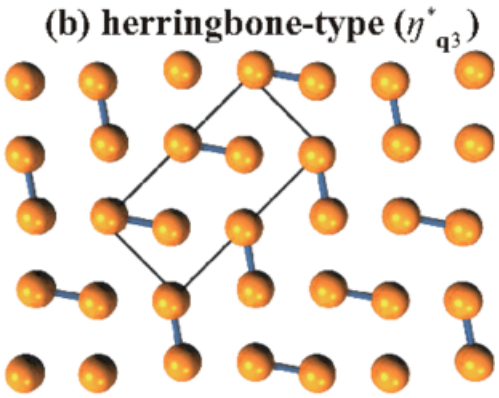

Figure 1.12: Schematic image of herringbone-type structure. Reprinted with permission from [66]. Copyright 2016 by American Physical Society.

can form the square net structure even in hypervalent bonding rule, indicating unusual condition of Bi^{2-} square net in R_2O_2Bi.

The similar electronic configurations to Bi^{2-} square net are widely observed in chalcogen compounds such as RTe_2 and RTe_3 [62] where Te^- anions should form square net. However, observed square net is quite unstable and incidentally shows Peierls distortion, i.e., charge density wave (CDW) transition, because one excess electron occupies an anti-bonding orbital in addition to the favorable dimerization of Te^- due to the octet rule. Indeed, the analogous compounds R_2O_2Sb also shows CDW transition where Sb^{2-} anions form dimers resulting in herringbone-type Sb layer (Fig. 1.12) [64, 65]. On the other hand, surprisingly, there are no CDW transition in R_2O_2Bi compounds [57–59]. Theoretical report indicates that strong spin-orbit coupling and chemical pressure effect suppress CDW instability, unusually retaining the complete Bi^{2-} square net [66]. The longer Bi–Bi bond length in R_2O_2Bi than that in $AMBi_2$ is due to the presence of one anti-bonding electron, evidencing Bi^{2-} state.

1.2.2 Anisotropic Dirac fermion in Bi square net compounds

Although the existence of Bi square net has been known for half a century ago, recent discovery of anisotropic Dirac fermion in Bi square net explosively accelerated its research. Figure 1.13 shows angle-resolved photoelectron spectroscopy (ARPES) images of $SrMnBi_2$ [67]. Along Γ-M line (cut 2), the sharp needle-like band dispersion is observed both near Fermi level and at high binding energy, indicating the existence of

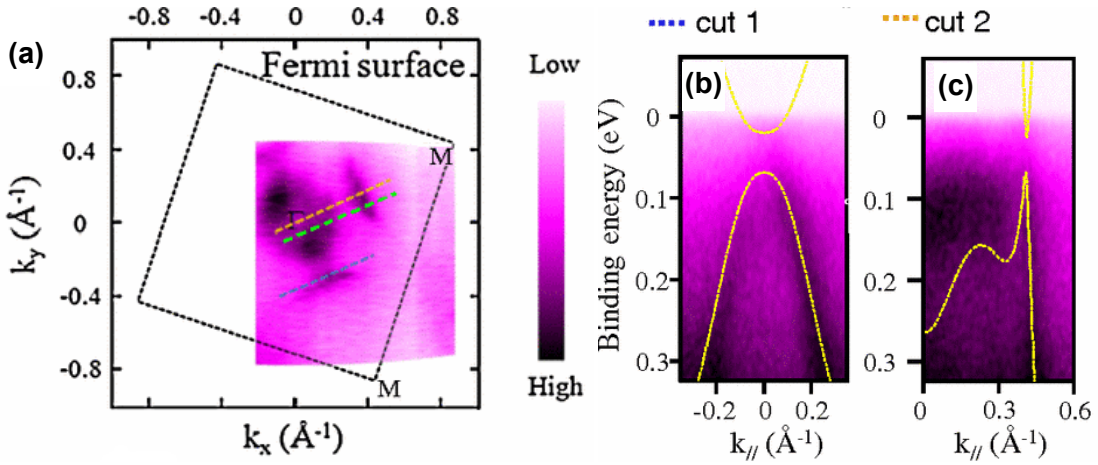

Figure 1.13: The results of ARPES of $SrMnBi_2$. (a) Fermi surface. Band dispersion (b) perpendicular to Γ-M line (blue broken line in (a)) and (c) parallel to Γ-M line (orange broken line in (a)). Reprinted with permission from [67]. Copyright 2011 by American Physical Society.

Dirac fermions. The estimated Fermi velocity of $v_F^{\parallel} \approx 1.1 \times 10^6\,\mathrm{m\,s^{-1}}$ is comparable to the value of graphene. On the other hand, band dispersion shows curvature near Fermi level perpendicular to Γ-M line (cut 1) with almost linear dispersion at high binding energy resulting in relatively small Fermi velocity of $v_F^{\perp} \sim 2 \times 10^5\,\mathrm{m\,s^{-1}}$. This result indicates the large anisotropy of Dirac-like band dispersion with $v_F^{\parallel}/v_F^{\perp} \gtrsim 5$, consistent with the theoretical calculation [42,67,68]. This anisotropic Dirac fermion has been only theoretically proposed in such as bent graphene and some nanocomposites [67], probably connecting to the exotic quantum phenomena and application to novel electronic devices with different direction of carrier conduction path. Therefore, naturally formed anisotropic Dirac fermion in $SrMnBi_2$ is valuable and attracts much attention.

The existence of Dirac fermions in Bi^- square net are also characterized in electrical transport properties [69]. Figure 1.14a shows angular dependence of magnetoresistance (MR) of $SrMnBi_2$. The MR showed two-fold symmetry with complete fitting by $|\cos\theta|$ function, demonstrating two-dimensional carrier conductive path, i.e., Bi^- square net. Notably, MR shows unsaturated linear behavior confirmed by constant $\mathrm{d}MR/\mathrm{d}B$ at high field, contrary to a saturation at high field in normal metals (Fig. 1.14bc). This unsaturated linear MR is a typical phenomenon of linear band dispersive compounds which are experimentally observed and theoretically explained [69, 70]. In addition, small effective mass of carriers ($0.29m_e$) and high carrier mobility ($250\,\mathrm{cm^2\,V\,s^{-1}}$ [67]

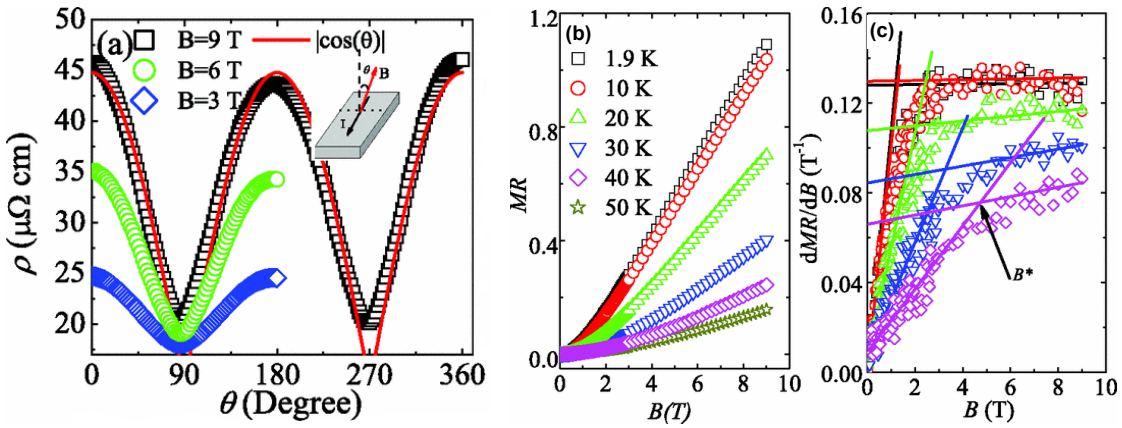

Figure 1.14: (a) Angular dependence of MR. Inset shows measurement configuration. (b) MR at various temperatures. (c) The field derivative of MR at various temperatures. Reprinted with permission from [69]. Copyright 2011 by American Physical Society.

and 3400 $cm^2\ V\ s^{-1}$ [69]) are estimated from the MR data. These results strongly support the existence of Dirac fermions in Bi^- square net.

The anisotropic Dirac fermions are also observed in other $AMBi_2$ compounds such as $CaMnBi_2$ [71,72], $LaAgBi_2$ [73], $EuMnBi_2$ [53,74], $BaMnBi_2$ [75], and $YbMnBi_2$ [44]. It was initially considered that magnetic ordering mediated the formation of anisotropic Dirac fermions because first compounds such as $SrMnBi_2$ and $CaMnBi_2$ show AF ordering of $MnBi_4$. However, the similar behavior in non-magnetic $LaAgBi_2$ suggests the universal existence of anisotropic Dirac fermions in Bi^- square net. Indeed, theoretical studies support this scenario [42,67,68]. A single Bi square net can possess Dirac like band dispersion composed of Bi $6p_x$ and $6p_y$ orbitals. The Dirac band is weakly hybridized with adjacent atoms A in $AMBi_2$ compounds especially perpendicular to Γ-M line, resulting in the anisotropy of Dirac band between parallel and perpendicular to Γ-M line. Furthermore, there are mainly two effects of A atoms to Dirac band. First, the different arrangement of A atoms adjacent to Bi square net (bottom of Fig. 1.8) causes different hybridization effect demonstrating the flatter band shape of $CaMnBi_2$ than that of $SrMnBi_2$. Second, different kinds of atoms change the strength of spin-orbit coupling of Bi square net, resulting in the larger bang gap of $SrMnBi_2$ than that of $CaMnBi_2$. These results indicate that the properties of Bi square net can be engineered by designing surrounding environment of Bi square net.

The AF ordering of $MnBi_4$ in $SrMnBi_2$ and $CaMnBi_2$ seems not to affect the Dirac

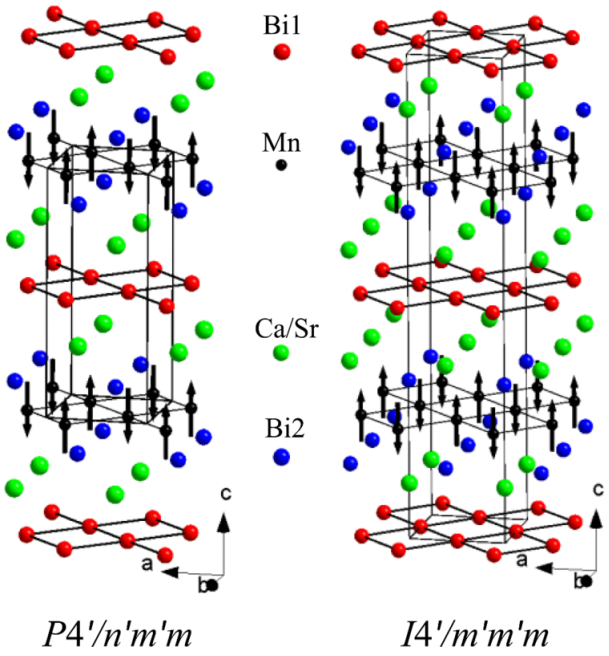

Figure 1.15: Magnetic structures of $CaMnBi_2$ (left) and $SrMnBi_2$ (right). Reprinted with permission from [76]. Copyright 2014 by American Physical Society.

band formation. However, their different spin ordering states possibly have some influence on electrical transport properties with (without) kink at T_N in electrical resistivity in $CaMnBi_2$ ($SrMnBi_2$), where $CaMnBi_2$ has ferromagnetic inter-layer coupling and $SrMnBi_2$ has AF one (Fig. 1.15) [76, 77]. Recent study claims that $YbMnBi_2$ is a first compound possessing magnetic Weyl fermion [78]. In addition, buckled Bi square net is theoretically proposed as a novel two-dimensional topological insulator with large band gap, connecting to the possible application to room temperature innovative device [79]. The exploration of Dirac band in Bi square net is still developing, so that various exotic phenomena will continue to be induced.

1.2.3 Kondo lattice behavior in Ce*M*Bi$_2$

Several CeMBi$_2$ compounds such as $CeNiBi_2$ and $CePd_{1-x}Bi_2$ show Kondo lattice behavior originating from Ce^{3+} moment [80, 81]. These compounds show AF ordering of Ce $4f^1$ moment at low temperature (~6 K) with strong anisotropy in temperature dependence of magnetic susceptibility (χ-T curve). The magnetic easy axes are [001] directions. Notably, the deviation of χ-T curves from Curie-Weiss law is observed below 50 K for $CeNiBi_2$ and 75 K for $CePd_{1-x}Bi_2$, attributed to the strong effect of crystalline-

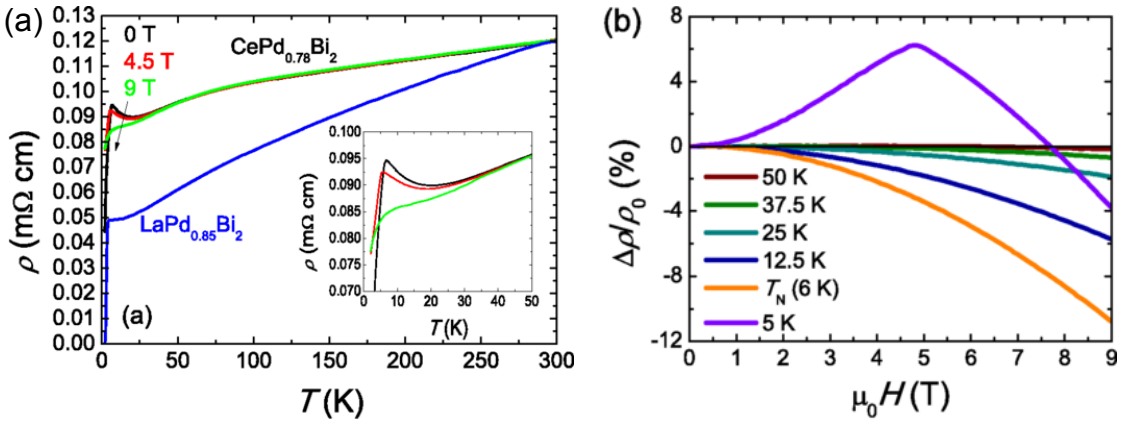

Figure 1.16: (a) The ρ-T curves of $CePd_{1-x}Bi_2$ at various fields. (b) Magnetoresistance data of $CePd_{1-x}Bi_2$ below 75 K. Reprinted with permission from [81]. Copyright 2015 by American Physical Society.

electric-field. The interaction between Kondo and crystalline-electric-field effect cause interesting phenomena in electrical transport properties. Figure 1.16a shows ρ-T curves of $CePd_{1-x}Bi_2$ at various fields. The broad shoulder-like anomaly is observed around 75 K originating from the interaction between Kondo and crystalline-electric-field effect, which is widely observed in Ce-based compounds [81]. The ρ minimum at 20 K is attributed to the typical Kondo effect. In addition, abrupt ρ drop at 6 K is due to the AF ordering, and this anomaly shifts to lower temperature followed by suppression with increasing magnetic field, because AF ordering connects to metamagnetic transition induced by the field. The MR shows small positive values (~0.2 %) at $T > 75$ K in $CePdBi_2$. On the other hand, the MR turns to negative values with larger absolute values at $T < 75$ K (Fig. 1.16b), except for anomaly at $T < T_N$ attributed to the AF to metamagnetic transition. The polarity change of MR is due to the Fermi surface reconstraction caused by interaction between Kondo and crystalline-electric-field effect around 75 K. The similar complicated interaction is also observed in $CeNiBi_2$ [80].

1.2.4 Potential for superconducting Bi square net

The induction of superconductivity in Bi square net is fascinating issue because it should become intriguing platform to investigate the interaction between superconductivity and Dirac fermion, probably connecting to the topological superconductivity. In 2011, $CeNi_{1-x}Bi_2$ was reported as a first compound possessing superconducting Bi^- square

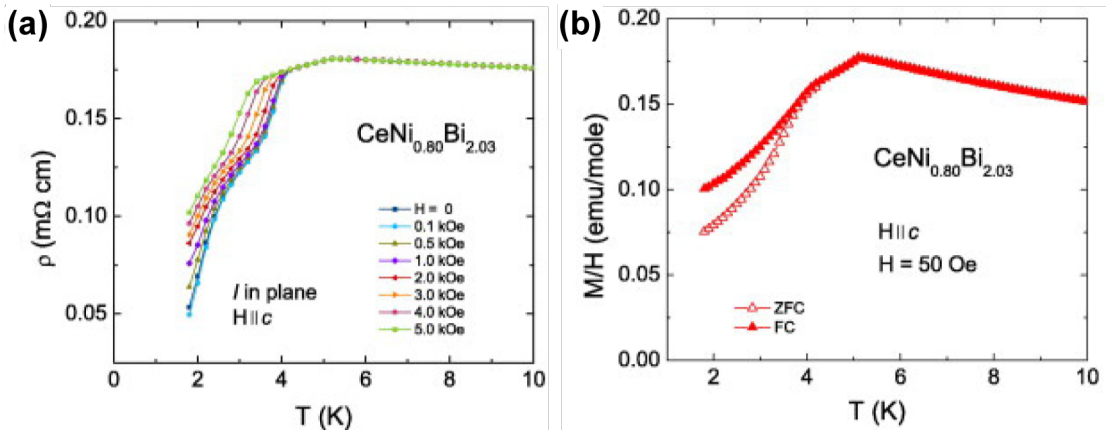

Figure 1.17: (a) The ρ-T curves at various fields and (b) χ-T curve of $CeNi_{0.8}Bi_2$ single crystal. Reprinted with permission from [46]. Copyright 2013 by Elsevier.

net with T_c of 4.2 K [82]. Authors claimed that superconductivity associated with the light carriers in Bi^- square net coexisted with the AF ordering at ~5 K of heavy carriers in Ce^{3+}, and Ni deficiency was essential to induce superconductivity. However, this result is not reproduced in subsequent reports [46, 83, 84]: the samples show no Ni deficiency dependence of superconducting properties, no reproducibility of the emergence, and small superconducting volume fraction (Fig. 1.17). Furthermore, T_c of 4.2 K is a similar value to those of NiBi and $NiBi_3$ [85, 86], and $LaNi_{1-x}Bi_2$ shows the same T_c and H_{c2} with small superconducting volume fraction [46, 82]. These results indicate that superconductivity of $CeNi_{1-x}Bi_2$ is not intrinsic but originating from impurity phases such as NiBi and $NiBi_3$.

$LaPd_{1-x}Bi_2$ is reported as superconducting at 2.1 K although rare earth substituted $CePd_{1-x}Bi_2$ shows AF ordering of Ce^{3+} at 6 K without superconductivity as shown in previous subsection (Fig. 1.18) [47]. Band calculation indicates that Pd orbital has the dominant contribution to form Fermi surface. In addition, Pd vacancy suppress the Fermi surface nesting, i.e., CDW instability, which seems essential to induce superconductivity. The small residual resistivity ratio (RRR) is attributed to the strong scattering by Pd vacancy, supporting the carrier conduction at Pd layer. Furthermore, the superconductivity is suppressed by compensating Pd vacancy and also the substitution of Fe for Pd, consistent with the band calculation [87]. These results confirm that the superconducting path is the Pd layer.

The superconductivity is also observed at 5.7 K in $SrMnBi_2$ with blob-like Bi

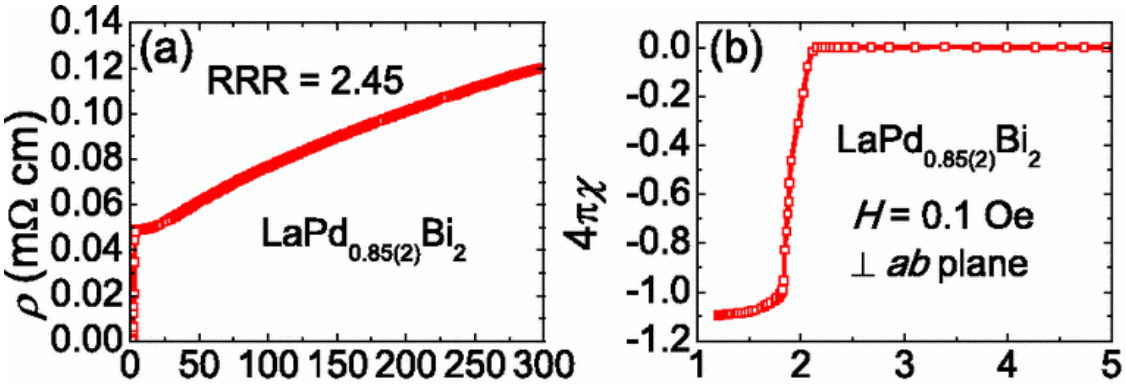

Figure 1.18: (a) The ρ-T curve and (b) χ-T curve of $LaPd_{0.85(2)}Bi_2$ single crystal. RRR is derived by ρ_{300K}/ρ_{T_c}. Reprinted with permission from [47]. Copyright 2013 by American Physical Society.

residue [88]. However, this superconductivity shows strong sample dependence and is not reproduced. It is considered that the superconductivity is originating from the strained Bi grown on the $SrMnBi_2$ crystals, and not from intrinsic Bi^- square net [88].

To summarize the above contents, superconducting Bi square net has not been discovered in spite of the extensive studies in $AMBi_2$ compounds.

1.2.5 Physical properties of R_2O_2Bi (R: rare earth)

In contrast to the case of Bi^- square net, the physical properties of Bi^{2-} square net is still not well known. Ferromagnetic ordering was observed at 154 K in U_2N_2Bi originating from U^{4+} [89] around 40 years ago, but there are no follow-up reports about actinoid compounds.

The promising platform to investigate the intrinsic properties of Bi^{2-} square net is R_2O_2Bi, which was systematically synthesized in polycrystalline powder form in 2011 [58]. Figure 1.19 shows temperature dependence of normalized electrical resistivity $\rho(T)/\rho_{300K}$ in various R_2O_2Bi compounds. Electrical transport property shows insulator-to-metal transition induced by chemical pressure: variation from insulating in La_2O_2Bi to metallic behavior in Er_2O_2Bi. However, the superconductivity is not observed down to 1.8 K [26, 58]. The origin of the insulator-to-metal transition was considered to be attributed to a Mott transition [58], but subsequent theoretical report suggested that this is due to the stronger electron-phonon coupling resulting in increased electron-phonon scattering in La_2O_2Bi than that in Er_2O_2Bi [66]. The band calculation indicates that the

Fermi surface is composed of Bi $6p_x$ and $6p_y$ orbitals of Bi^{2-} square net in R_2O_2Bi, suggesting two-dimensional electronic nature [58,66]. The χ-T curves shows sharp drop around 10 K in magnetic R_2O_2Bi (R: Pr, Gd, Er) indicating the AF ordering of $4f$ spins in R cations [58]. The χ-T curves are well fitted by Curie-Weiss law $\chi = \chi_0 + C/(T-\theta)$ at $T > T_N$, demonstrating similar effective Bohr magneton values P_{eff} to theoretical values of R^{3+} state (Table 1.2), evidencing unusual Bi^{2-} state.

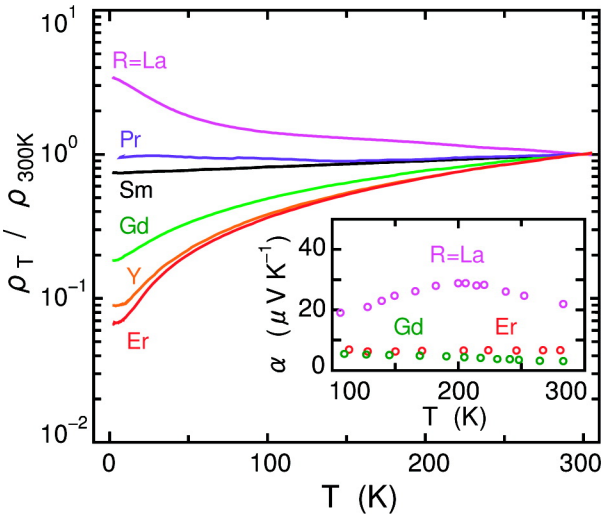

Figure 1.19: Normalized ρ-T curves of R_2O_2Bi compounds. The inset shows Seebeck coefficients α demonstrating p-type conduction. Reprinted with permission from [58]. Copyright 2011 by American Chemical Society.

Table 1.2: Magnetic parameters for R_2O_2Bi compounds. Reprinted with permission from [58]. Copyright 2011 by American Chemical Society.

cmpd	T_N (K)	χ_0 (emu mol-R^{-1})	θ (K)	C (emu mol-R^{-1})	P_{eff} (μ_B)
Pr_2O_2Bi	15.0	0.0008	−25.1	1.71	3.70
Gd_2O_2Bi	10.1	0.0011	−25.0	7.80	7.90
Er_2O_2Bi	3.0	0.0021	−19.4	12.32	9.90

1.3 Purpose of this study

As mentioned in previous section, Bi square net compounds are good platform to investigate the exotic quantum phenomena originating from two-dimensional electronic nature and strong spin-orbit coupling, while superconducting Bi square net have not been realized yet. In contrast to the well-studied $AM\mathrm{Bi}_2$ compounds with Bi^- square net, there are few reports about Bi^{2-} square net compounds probably due to the instability of unusual electronic configuration. The electrical resistivity and magnetic susceptibility are evaluated in $R_2\mathrm{O}_2\mathrm{Bi}$, but detailed physical properties of unusual Bi^{2-} square net is not fully understood despite the possible emergence of various attractive properties owing to Bi^{2-} square net.

The motivation of this study was to unveil the intrinsic properties and to induce the novel phenomena of Bi^{2-} square net in $R_2\mathrm{O}_2\mathrm{Bi}$ via two approaches: the fabrication of epitaxial thin films and the synthesis of bulk polycrystalline powders. The main aim of first topic was the establishment of universal fabrication method for $R_2\mathrm{O}_2\mathrm{Bi}$ epitaxial thin films which are ideal samples to evaluate the intrinsic physical properties. I succeeded in achievement of the epitaxial thin films by developing two novel fabrication techniques utilizing solid-phase epitaxy. In addition, the influence of two-dimensional electronic nature and the strong spin-orbit coupling on electrical transport properties were investigated for the first time. The purpose of second topic was the control of physical properties of Bi^{2-} square net by tuning the composition and the crystal structure of $R_2\mathrm{O}_2\mathrm{Bi}$ in the form of polycrystalline powders, which are relatively easy to synthesize in comparison with epitaxial thin film. I aimed to construct a guideline to for properties engineering of Bi^{2-} square net compounds as a counterpart of various Bi^- square net compounds described above, resulting in the discovery of universal two-dimensional superconductivity of Bi^{2-} square net.

Chapter 2

Experimental techniques

2.1 Sample preparation

2.1.1 Pulsed laser deposition

Pulsed laser deposition (PLD) is widely utilized to obtain high quality oxide epitaxial thin film [90]. Figure 2.1 shows a schematic image of PLD method. In vacuum chamber, the pulsed laser of KrF excimer (λ = 248 nm) is irradiated on the sintered target of sample. The target material is vaporized and deposited on the substrate fixed at a face-to-face position. The substrate temperature is controllable by using infrared semiconductor laser up to ~1000 °C. In addition, the background pressure is adjustable by introducing gases such as O_2 and Ar, although the deposition was conducted at high vacuum without any gas introduction in this study. The PLD chamber is equipped with the reflection high

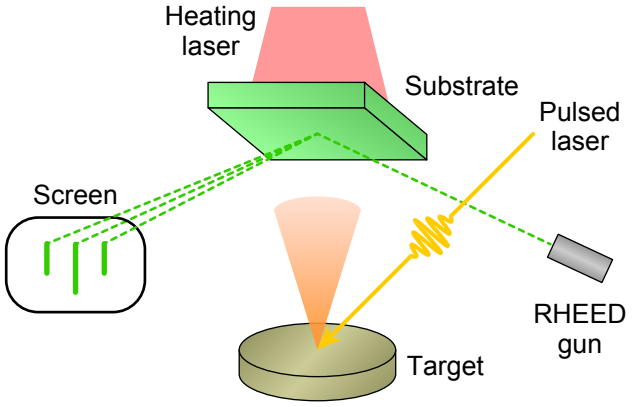

Figure 2.1: A schematic image of PLD equipment.

energy electron diffraction (RHEED) system which enables *in situ* monitoring of the thin film growth: the single crystalline sample yields in the streak or dot pattern while the amorphous film projects halo pattern according to their surface structures.

2.1.2 Sputtering

Constituent atoms of solid are ejected from the target surface when high-energy gas ion collide with the target. This phenomenon is called sputtering evaporation or just sputtering [91, 92]. Currently, sputtering is widely used in semiconductor and spintronic device manufacturing process such as surface cleaning, micromachining, thin film and junction formation, and surface analysis. It is also applied to the thin film growth in basic research since it is possible to fabricate the large area thin film in addition to no limitation of material selection.

Sputtering generates a glow discharge. Its generation mechanism is as follows. Electrons accelerated to the anode by the electric field collide with the gas molecules such as Ar to generate the cations. The cations are accelerated to collide with the target on cathode resulting in the emission of secondary electrons. The glow discharge is generated during a steady state by repeating the above process. When the cations collide

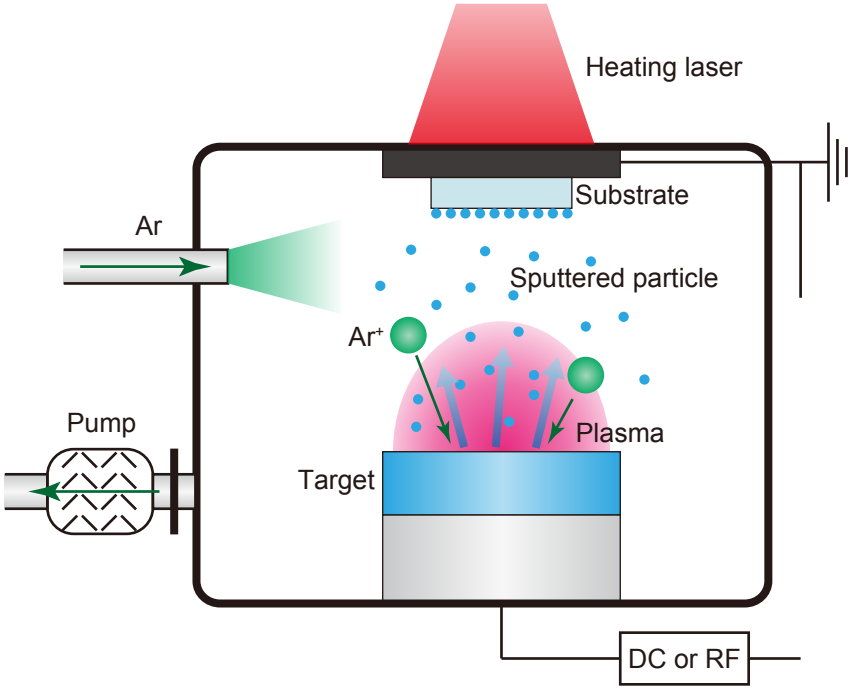

Figure 2.2: A schematic image of sputtering chamber.

with the target on cathode, not only secondary electrons but also the substances of the target on cathode are emitted from the surface. These sputtered particles are deposited on the substrate and form the thin film.

Figure 2.2 shows a schematic image of the sputtering chamber. Sputtering is performed by introducing Ar gas into the vacuum chamber. The target material is evaporated by the irradiation of the ionized Ar and deposited on the substrate positioned in opposite side. This chamber is equipped with a substrate heating laser, so thin film growth can be performed at ~1000 °C maximum. There are two-types of power sources: direct current (DC) and radio frequency (RF) modes. In DC sputtering, the target material is applied to the negative bias and the substrate is placed on anode side. This approach is utilized in conducting materials such as a metal. However, DC sputtering cannot be applied to insulating materials due to the positively charged target by the collision with the cations. This charge-up can be suppressed by using RF power source because electrons and cations collide alternately by applying RF bias. The mobility of electrons in plasma is larger than that of cations, so the target surface is biased to a negative DC potential. RF sputtering can be used for the thin film growth of any materials from conductor to insulator.

In general, the deposition rate of the sputtering is slow due to the scattering of the sputtered particles in the high operating pressure. Magnetron sputtering is effective to increase the deposition rate. Magnets are arranged in order to produce magnetic field line on the target surface as shown in Fig. 2.3. Secondary electrons are confined in the vicinity of the target along the magnetic field line, therefore it is possible to form a high density plasma efficiently, resulting the decrease of operating pressure. A disadvantage

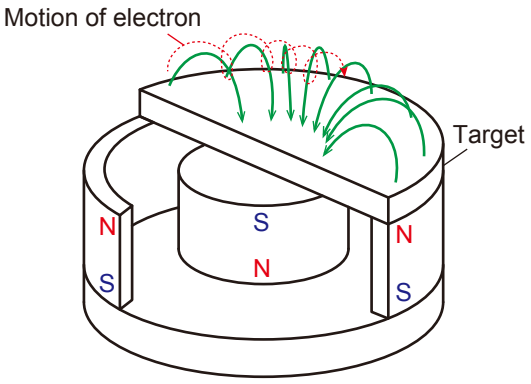

Figure 2.3: A schematic image of magnetron sputtering.

of the magnetron sputtering is the reduced efficiency of the use of target because of nonuniform sputtering at target surface.

2.1.3 Vacuum sealing

The polycrystalline powders of R_2O_2Bi cannot be obtained by the solid state reaction in air because of too excess amount of O in atmosphere to achieve unusual reductive Bi^{2-} state. Therefore, polycrystalline samples must be heated in vacuum sealed quartz tubes. The starting materials are weighed, mixed, pelletized and sealed into the quartz tubes by using vacuum valve in Ar- or N_2-filled glovebox (O_2, $H_2O < 1$ ppm) in order to avoid the oxidation. The sample pellets are covered with Ta foil (0.04 mm thick, purity: 3Nup) to suppress the side reactions and contamination with Si. Then, the quartz tubes are transferred to air and connected to the rotary pump. Finally, the quartz tubes are sealed with a city/propane and O_2 mixed gas burner under evacuation. By heating those vacuum sealed samples in electric furnace, it is possible to limit the O supply from only starting materials and quartz.

2.2 Crystallographic characterization

2.2.1 X-ray diffraction

X-ray diffraction (XRD) is a powerful method to characterize the crystal structure of solids [93]. The solid crystal has a periodic structure with angstrom order. When X-ray having same wavelength to the periodicity is incident on the crystal, X-ray is diffracted from the lattice plane according to the following Blagg's law (Fig. 2.4),

$$2d \sin\theta = n\lambda \tag{2.1}$$

where d is the distance between lattice planes, θ is the incident angle of X-ray, n is the integer, and λ is the wavelength of X-ray. Each substance possess its own diffraction pattern including the structural information such as constituent elements, lattice constants, and Miller indices. Therefore, XRD measurement enables the analysis of detailed crystal

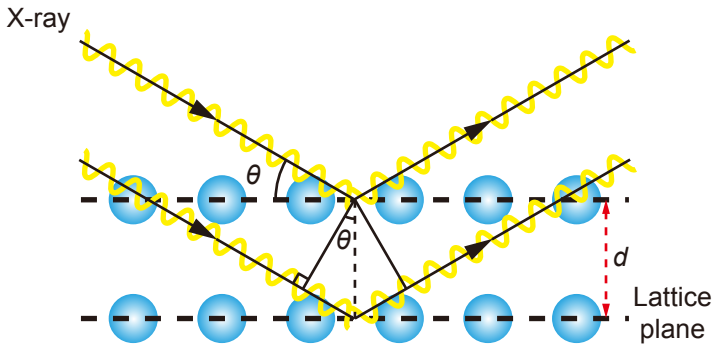

Figure 2.4: A schematic image of Bragg's law.

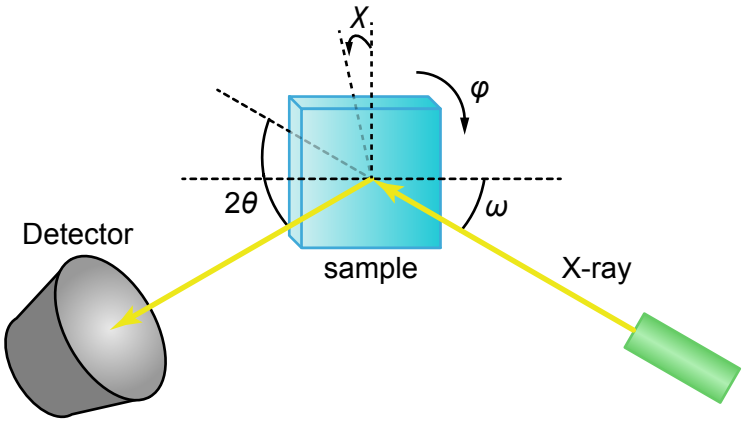

Figure 2.5: A schematic image of measurement configuration of XRD equipment.

structure and the identification of the substance.

Figure 2.5 shows a schematic image of the diffractometer utilized in this study (D8 DISCOVER, Bruker AXS). The equipment owns four movable axes: ω corresponds to the incident angle of X-ray, 2θ corresponds to the angle between incident and diffracted X-ray, and ϕ and χ correspond tilt angles along in-plane and out-of-plane directions to sample surface, respectively. In general 2θ-θ scan, the diffraction pattern is corrected by moving 2θ with fixed $\omega = \theta$. As a result, all Bragg diffraction peaks can be corrected in polycrystalline samples, while only the diffraction peaks of a specific plane orientation (hkl) are detected in single crystalline samples by adjusting ϕ and χ axes. The rocking curve measurement is performed to evaluate the crystallinity of the crystal. The 2θ, ϕ, and χ axes are fixed in order to observe a specific Bagg hkl peak, then only ω is scanned. The smaller full width at half maximum (FWHM) of diffraction peak corresponds to the higher crystallinity. The ϕ scan is conducted to evaluate rotational symmetry and plane orientation of the crystal by fixing ω, 2θ, and χ. In this study, Cu Kα ($\lambda = 1.5418$ Å) or

monochromated CuKα_1 radiation (λ = 1.5405 Å) was used for the measurement.

2.2.2 Rietveld refinement

The Rietveld refinement is a powerful technique to analyze the structural parameters of solids such as lattice constants, fractional coordinates, and atomic displacement parameters [93, 94]. The measured powder X-ray or neutron diffraction pattern is refined by theoretical pattern of assumed structural model by nonlinear least-squares method. In other words, the Rietveld refinement minimize the residual sum of squares $S(\boldsymbol{x})$ represented by following equation,

$$S(\boldsymbol{x}) = \sum_{i=1}^{N} w_i [y_i - f_i(\boldsymbol{x})]^2 \tag{2.2}$$

where $\boldsymbol{x}$ is refined parameters, N is total number of datapoint, y_i is observed measured intensity, $f_i(\boldsymbol{x})$ is calculated intensity, and w_i is statistical weight which usually adopts $1/y_i$. Furthermore, the $f_i(\boldsymbol{x})$ is described by the following equation,

$$f_i(\boldsymbol{x}) = S_{\mathrm{R}}(\theta_i) A(\theta_i) D(\theta_i) s \sum_K m_K |F(\boldsymbol{h}_K)|^2 P_K L(\theta_K) G(\Delta 2\theta_{iK}) + y_b(2\theta_i) \tag{2.3}$$

where $S_{\mathrm{R}}(\theta_i)$ is correlation factor for surface roughness, $A(\theta_i)$ is absorption factor, $D(\theta_i)$ is correlation factor for the constant irradiation width, s is scale factor, K is reflection number, m_K is multiplicity, $F(\boldsymbol{h}_K)$ is structure factor, $\boldsymbol{h}_K$ is reflection indices hkl, P_K is correlation factor for preferred orientation, $L(\theta_K)$ is Lorentz and polarization factor, θ_K is Bragg angle, $G(\Delta 2\theta_{iK}) = G(2\theta_i) - G(2\theta_K)$ is profile function, and $y_b(2\theta_i)$ is background correlation. Although the $f_i(\boldsymbol{x})$ seems to have a complicated formula, most of factors are automatically and uniquely determined, and generally there are only four parameters which need to be refined: s, $y_b(2\theta_i)$, $F(\boldsymbol{h}_K)$, and $G(\Delta 2\theta_{iK})$. Hereafter, I explain the each function used in the Rietan-FP program [95].

Scale factor s

The scale factor s just multiplies the calculated intensity to fit into the observed in tensity. The quantitative analysis in multiphase system is based on the s values of each phase.

Background correlation $y_b(2\theta_i)$

There is no method to estimate the background accurately, so that the function of Bragg angle is widely utilized to approximate the observed background. The Rietan-FP adopts the sum of Legendre polynomials as the fitting function for the background described by the following equation,

$$y_b(2\theta_i) = \sum_{j=0}^{11} b_j P_j(q_i) \tag{2.4}$$

$$P_j(q_i) = \left(\frac{2j-1}{j}\right) q_j P_{j-1}(q_j) - \left(\frac{j-1}{j}\right) P_{j-2}(q_i) \tag{2.5}$$

where $P_j(q_i)$ is the Legendre polynomial and b_j is background parameter. The $y_b(2\theta_i)$ is fitted by refining coefficients b_j although there is no physical meaning.

Crystal structure factor $F(\boldsymbol{h}_K)$

The $F(\boldsymbol{h}_K)$ is the main component to determine the peak intensity of each reflection and described by the following equation,

$$F(\boldsymbol{h}_K) = \sum_j f_j g_j T_j \exp[2\pi i(hx_j + ky_j + lz_j)] \tag{2.6}$$

where j denote the atom in unit cell, f_j is atomic form factor, g_j is occupancy, T_j is the Debye-Waller factor, and x_j, y_j, z_j are fractional coordinates. The f_j is the scattering power of each atom which is almost proportional to the atomic number, derived by the Fourier transform the electron density,

$$f\left(\frac{\sin\theta}{\lambda}\right) \simeq f_0\left(\frac{\sin\theta}{\lambda}\right) = \int_{\text{atom}} \rho(\boldsymbol{r}) \exp[2\pi i(\boldsymbol{k} - \boldsymbol{k}_0)\cdot\boldsymbol{r}]\mathrm{d}v \tag{2.7}$$

where $\rho(\boldsymbol{r})$ is the electron density of the atom at $\boldsymbol{r}$, $\boldsymbol{k}$ and $\boldsymbol{k}_0$ are wave number vectors of scattered and incident waves, respectively. The f becomes small with increasing θ which is the main reason of 2θ dependence of diffraction intensity. The T_j indicates the attenuation of scattering amplitude du to the static disorder and thermal oscillation of the

atoms, described by the following equation,

$$T_j = \exp\left[-B_j\left(\frac{\sin\theta_K}{\lambda}^2\right)\right] \tag{2.8}$$

where B_j is atomic displacement parameter indicating the mean square displacement from mean position. The $F(\boldsymbol{h}_K)$ is calculated by refining structural parameters such as lattice constants, occupancy, fractional coordinates, and atomic displacement parameters, demonstrating the crystal structure of the sample.

Profile function $G(\Delta 2\theta_{iK})$

The pseudo-Voigt function is widely used to fit the peak shape, which is a linear combination between the Lorentzian and Gaussian described by the following equation,

$$G(\Delta 2\theta_{iK}) = \eta\frac{2}{\pi H_K}\left[1+4\left(\frac{\Delta 2\theta_{iK}}{H_K}\right)^2\right]^{-1} + (1-\eta)\frac{2\sqrt{\ln 2}}{\sqrt{\pi}H_K}\exp\left[-4\ln 2\left(\frac{\Delta 2\theta_{iK}}{H_K}\right)\right] \tag{2.9}$$

where H_K is FWHM and η is the Lorentzian fraction. The $G(\Delta 2\theta_{iK})$ varies from Lorentzian to Gaussian by changing η. The crystalline size and microstrain affect both Lorentzian and Gaussian components of peak shapes, so that these information can be obtained from the refined result of profile functions.

Reliability indices

In order to judge the convergence of the Rietveld refinement, there are several indicators as called reliability indices. The most important one is R_{wp} defined by the following equation,

$$R_{\mathrm{wp}} = \left\{\frac{\sum_{i=1}^{N}[y_i - f_i(\boldsymbol{x})]}{\sum_{i=1}^{N} w_i y_i^2}\right\}^{\frac{1}{2}} \tag{2.10}$$

where the numerator corresponds to the residual sum of squares $S(\boldsymbol{x})$. Therefore, the Rietveld refinement is performed to minimize the R_{wp}. The R_{e} is the theoretical minimum of R_{wp} where the statistical deviation of the observed intensity is included, and it is

described by the following equation,

$$R_e = \left\{ \frac{N-P}{\sum_{i=1}^{N} w_i y_i^2} \right\}^{\frac{1}{2}} \tag{2.11}$$

where P is the number of refined parameters. Accordingly, the ratio of R_{wp} to R_e, i.e., $S = R_{wp}/R_e$ is utilized to judge the reliability of refined results: $S = 1$ indicates the perfect fitting, and $S < 1.3$ is desired to regard as a sufficiently reliable result. However, the larger observed intensity results in the larger S, so that it is needed to cross-check the convergence of the refinement, e.g. by checking the reproducibility of the result from the different initial parameters.

2.2.3 Atomic force microscope

Atomic force microscopy (AFM) which is one of the scanning probe microscopy is used to evaluate surface morphology of solids [96]. We can get the information about the surface structure in the order of nanometers by utilizing atomic force between the solid surface and probe called cantilever. There is no restriction about the measurable sample for AFM because atomic force always exists between two objects in proximity.

Measurement principle of AFM is shown in Fig. 2.6. In order to detect the change of cantilever position, optical lever method is widely applied. Diode laser is irradiated on the back-miller of cantilever, and angular variation of the reflected light is detected

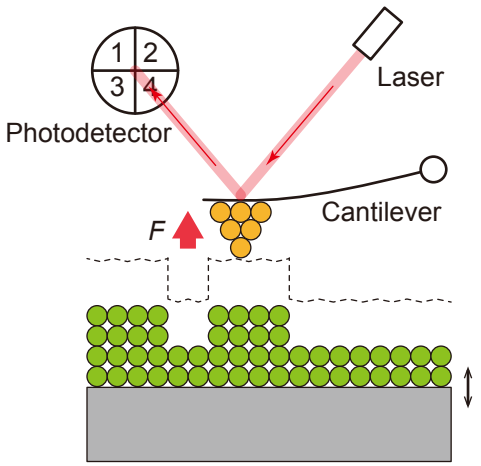

Figure 2.6: A schematic image of AFM.

by photodetector to evaluate deflection of cantilever. Measurement is performed by fixing the deflection and moving sample stage up and down in the feedback control. In this study, E-Sweep (Hitachi Nanotechnology Science) was used to observe the surface morphology of thin film samples.

2.3 Composition analysis

2.3.1 X-ray photoemission spectroscopy

When monochromatic radiation is irradiated to the substance, electrons are emitted by the photoelectric effect. These electrons are called photoelectron. X-ray photoemission spectroscopy (XPS) is a technique which measure the energy spectrum of photoelectron by utilizing X-ray as a probe [97].

The photoelectric effect is represented by the following equation,

$$E_{\mathrm{K}} = h\nu - E_{\mathrm{B}} - \phi \tag{2.12}$$

where E_{K} is the kinetic energy of emitted photoelectron, $h\nu$ is the energy of incident photon, E_{B} is the binding energy of emitted photoelectron, and ϕ is the work function. A schematic image of a relationship between photoelectric effect and XPS spectrum is

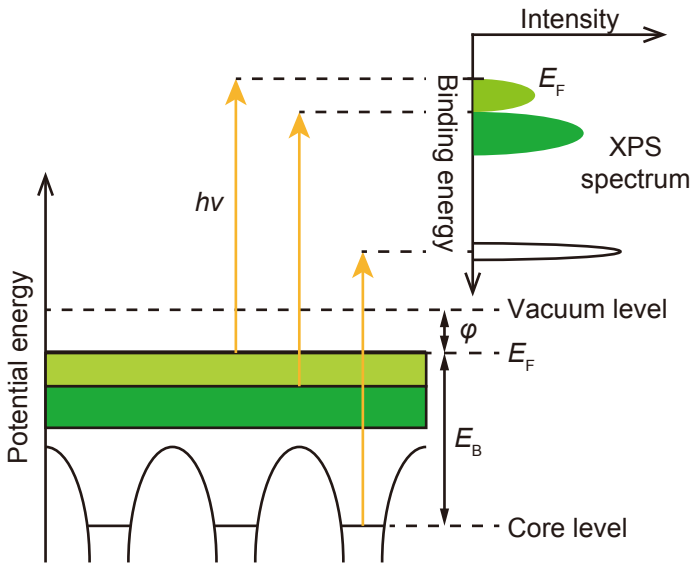

Figure 2.7: A schematic image of photoelectric effect and XPS spectrum.

shown in Fig. 2.7. Since a spectrometer and conductive samples possess same Fermi level in the actual measurement, E_B is corrected to the following equation,

$$E_B = h\nu - E_K - \phi_{eq} \tag{2.13}$$

where ϕ_{eq} is the work function of an equipment. Therefore, E_B can be derived from Eq. 2.13 by using monochromatic light source which have a constant $h\nu$ and pre-measured ϕ_{eq}. In case of the measurement of insulating samples, charge-up hampers the correct evaluation of the Fermi level. It is needed to prevent the sample from charge-up by depositing conductive film and/or irradiating electron neutralizing beam.

As can be seen in Fig. 2.7, XPS spectrum have the information of the electrons in both core level and valence band. Each element has the characteristic E_B for each orbital electron, leading to the identification of the elements from peak positions of XPS spectrum. Quantitative analysis is also possible from peak intensity. E_B is shifted due to the surrounding chemical conditions, so that the value of this chemical shift represents the valence state of the element. In this way, qualitative, quantitative, and chemical state analyses van be performed by XPS.

XPS is a highly surface sensitive because the most photoelectrons lose their energy due to the scattering in the solid internal and are absorbed into the solid. We can obtain the information in the depth direction by sputtering the sample surface. In this study, XPS measurements was performed by using Al Kα radiation as the probe in PHI 5000 VersaProbe (Ulvac-Phi, Inc.) equipped with sputtering system.

2.3.2 Electron probe microanalyzer

Electron probe microanalyzer is powerful tool to perform qualitative and quantitative analysis of constituent elements in the solid [98]. When accelerated electrons with energy of 1–20 keV are irradiated on the surface of the substance, inner shell electrons are excited to generate holes in the orbit. Then, outer shell electrons fall into this empty orbit, resulting in the generation of characteristic X-ray. Since the energy of the characteristic X-ray has a unique value for each element, qualitative analysis can be performed by detecting it. In addition, quantitative analysis is performed from the

intensity of characteristic X-ray. Mapping analysis is also possible by scanning the electron probe two-dimensionally.

Energy dispersive X-ray spectrometer (EDX) is widely utilized to detect the characteristic X-ray as follows. The incident X-ray into the semiconductor device generates electron-hole pairs whose numbers are proportional to the energy of the X-ray. These electrons are amplified by a strong electric field, resulting in pulses with intensity proportional to the energy of incident X-ray. In this study, the qualitative analysis of polycrystalline samples was mainly conducted by EDX installed in scanning electron microscopy (JEOL Ltd., JSM-7100F). The energy of electron probe was 15 keV.

2.3.3 Inductively coupled plasma mass spectrometry

Inductively coupled plasma (ICP) is a form of discharge caused by the induced current of the high frequency coil [99]. When Ar gas flows through the discharging high frequency coil, a large amount of ions and electrons, so-called plasma, are generated by the following chain reaction,

$$\begin{aligned} e^- + \mathrm{Ar} &\longrightarrow 2\,e^- + \mathrm{Ar}^+ \\ 2\,e^- + 2\,\mathrm{Ar} &\longrightarrow 4\,e^- + 2\,\mathrm{Ar}^+ \end{aligned} \tag{2.14}$$

where e^- denotes electron. The temperature of the generated plasma reaches 10 000 K, and it is used for atomization and thermal excitation of the sample. ICP mass spectrometry (ICP-MS) is a composition analysis method by utilizing this generated chemical species with mass spectrometer. The detection limit is very high as about ppb, although it is necessary to dissolve samples in acid for the analysis. In this study, ICP-MS was performed by Foundation for Promotion of Material Science and Technology of Japan.

2.4 Magnetic measurements

Electromagnetic induction method is utilized to evaluate the magnetic moment of material [100]. When the sample moves in homogeneous magnetic field, the electromotive force V is induced in pick up coil due to the change of magnetic flux density Φ, that is,

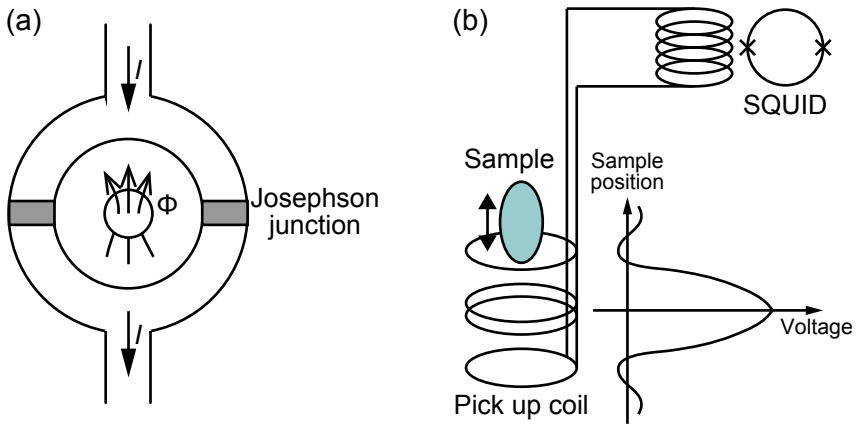

Figure 2.8: (a) A schematic images of SQUID magnetometer. (b) Measurement configuration of MPMS. Inset shows schematic image of output voltage.

$V = -\mathrm{d}\Phi/\mathrm{d}t$. According to the relationship $\Phi = km$ where m is the magnetic moment of the sample and k is the factor of proportionality which depends on measurement system, the m is obtained by the integral calculus of V,

$$m = \frac{1}{k}\int_0^t V\mathrm{d}t. \tag{2.15}$$

Superconducting quantum interference device (SQUID) is a powerful tool to evaluate the magnetic moment with high sensitivity [100, 101]. The SQUID magnetometer is composed of a superconducting ring where two Josephson junctions are connected in parallel (Fig. 2.8). In this system, the maximum of superconducting current is given by the following formula,

$$I_{\mathrm{max}} = 2I_{\mathrm{c}}\left|\cos\pi\frac{\Phi}{\Phi_0}\right| \tag{2.16}$$

where I_{c} is the critical current of each Josephson junction and $\Phi_0 \approx 2.07 \times 10^{-15}$ Wb is the flux quantum. Since the current is a periodic function with the periodicity of Φ_0, high sensitive detection of magnetic moment is possible with the magnetic quantum as a unit. In the actual measurement, a steady bias current larger than I_{c} flows in the SQUID ring, and thereby the voltage fluctuation with the periodicity of Φ_0 is detected.

In this study, magnetic property measurement system (MPMS, Quantum Design, Inc.) equipped with SQUID magnetometer was utilized to evaluate the magnetic properties. Figure 2.8b shows a schematic image of measurement configuration. The sample moved in the pick up coil and the changed magnetic flux is indirectly detected by SQUID

magnetometer. This is because the SQUID magnetometer needs to be shielded with the superconductor in order to avoid the influence from noise such as external magnetic field.

2.5 Electrical measurements

2.5.1 Four-probe method

Electrical resistance $R = V/I$ can be evaluated by wiring current and voltage electrodes properly. However, if both current and voltage are measured in same electrode, i.e. two-probe method, the obtained R contains contribution not only from sample but also wires and electrodes (Fig. 2.9a). Therefore, four-probe method is better to evaluate correct R value of sample where electrodes for current and voltage are separated (Fig. 2.9b) [102]. In this configuration, obtained R corresponds to the resistance between electrodes for voltage because current does not flow the voltmeter in ideal condition.

The obtained sample resistance R can be converted to electrical resistivity ρ by the following equation,

$$\rho = R\frac{wt}{L} \tag{2.17}$$

where w is a width of the sample perpendicular to the current direction, t is the sample thickness, L is the distance between electrodes for voltage.

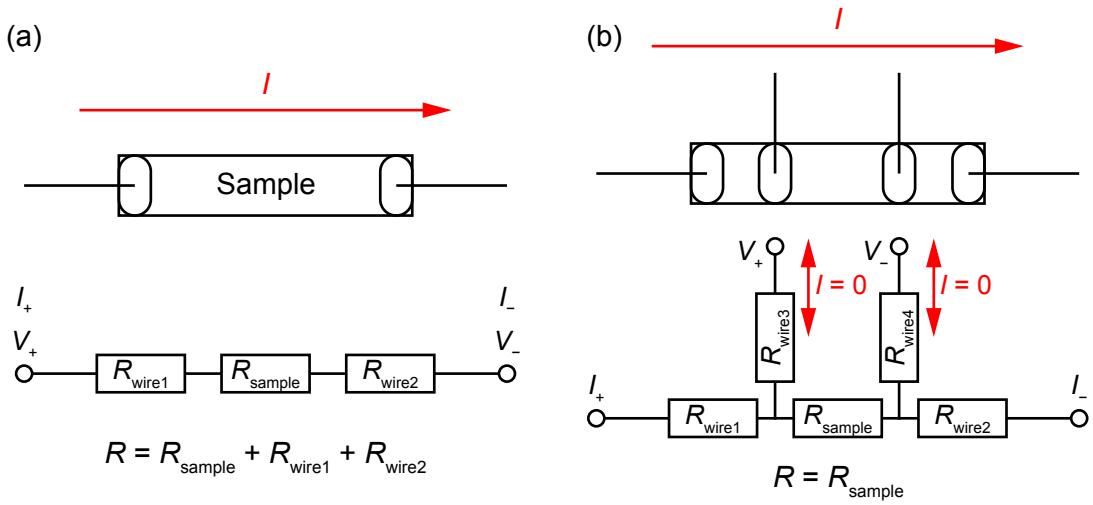

Figure 2.9: Schematic images of (a) two-probe and (b) four-probe configuration. I: current, V: voltage.

2.5.2 Hall measurement

Hall measurement is an useful technique to derive carrier type, density, and mobility. When a magnetic field $\mu_0 \boldsymbol{H} = \boldsymbol{B}$ is applied perpendicularly to the current $\boldsymbol{I}$, the charge carriers are accumulated in $\boldsymbol{I} \times \boldsymbol{B}$ direction due to the Lorentz force, resulting in the generation of electric field $\boldsymbol{E}$. This phenomenon is called Hall effect. By assuming that current flows along x ($\boldsymbol{I} = (I_x, 0, 0)$) and field is applied along z direction ($\boldsymbol{B} = (0, 0, B_z)$), the Hall coefficient R_H is defined by the following equation,

$$R_\mathrm{H} \equiv \frac{E_y}{j_x B_z} \tag{2.18}$$

where E_y is the so-called Hall electric field and j_x is the current density. The carrier polarity is derived from the sign of R_H: $R_\mathrm{H} > 0$ corresponds to the hole carrier and *vice versa*. Here, $E_y = V_y/w$ and $j_x = I_x/wt$ are obtained due to their definition, the R_H can be transformed to the following equation,

$$R_\mathrm{H} = \frac{V_y t}{I_x B_z} = \frac{R_{yx} t}{B_z} \tag{2.19}$$

where $R_{yx} = V_y/I_x$ is the Hall resistance. In addition, the carrier density n and mobility μ are represented by using R_H as follows,

$$n = \left| \frac{1}{R_\mathrm{H} e} \right| \tag{2.20}$$

$$\mu = \left| \frac{R_\mathrm{H}}{\rho} \right| \tag{2.21}$$

where e is the elementary charge. Therefore, we can obtain the carrier type, density, and mobility by measuring Hall resistance.

2.5.3 Measurement configuration

Figure 2.10 shows a schematic image of measurement configuration in this study. Both film and polycrystalline samples were processed into bar shape and the electrodes were fabricated by Au deposition with In crimp, only In crimp, or Ag paste. All electrical

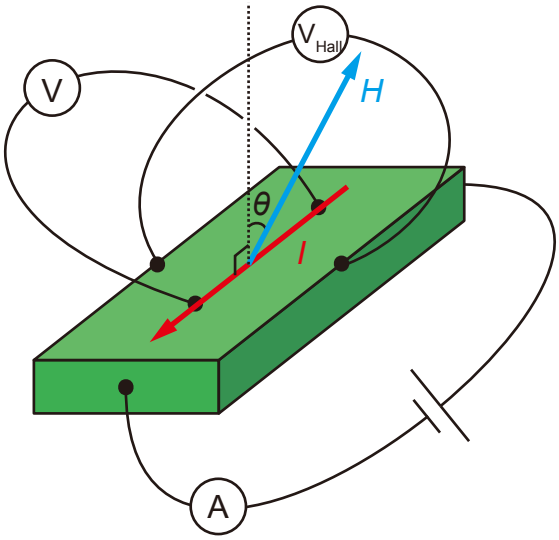

Figure 2.10: A schematic image of electrical measurement configuration in this study.

measurements were conducted by physical property measurement system (PPMS, Quantum Design, Inc.) equipped with sample rotator system. Temperature range was from 1.8 K without rotator system or 1.85 K with it to 300 K, and magnetic field was varied in the range of $-9 \leq \mu_0 H \leq 9$ T by superconducting magnet. The direction of applied magnetic field could be changed by rotating the samples in order to evaluate the angular dependence of MR.

2.6 Specific heat measurements

Specific heat measurements were conducted by the thermal relaxation method [103] with a ^{3}He/^{4}He dilution refrigerator [104] with the help of Kawaji group in Tokyo Institute of Technology.

2.6.1 Thermal relaxation method

Figure 2.11a shows measurement configuration of the thermal relaxation method composed of sample, holder, and heat bath. The holder equipped with heater and thermometer is connected to the heat bath by thermal resistance possessing thermal conductivity k. When the quantity of heat per unit time $Q = RI^2$ is applied to the sample system, the

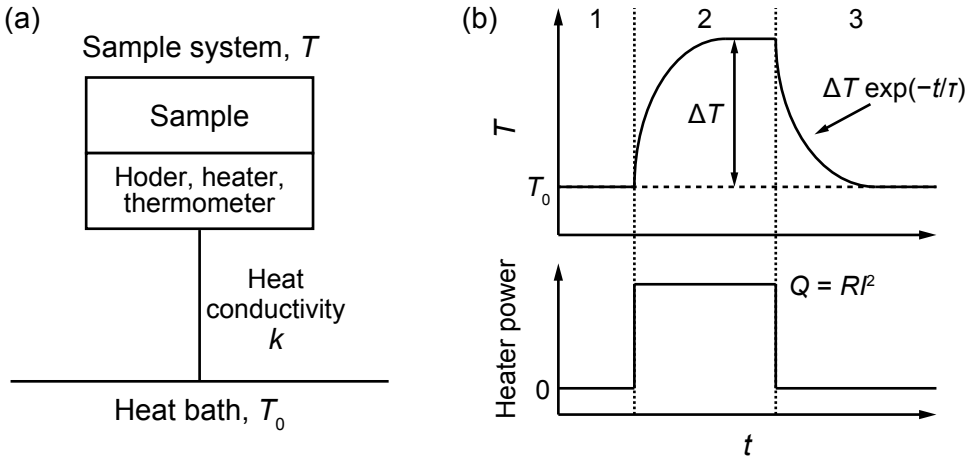

Figure 2.11: (a) A schematic image of measurement configuration for thermal relaxation method. (b) Time dependence of temperature change of the sample system (top) and heater power (bottom).

energy balance is represented by the following equation,

$$C_p \frac{\mathrm{d}T}{\mathrm{d}t} = Q - k(T - T_0) \tag{2.22}$$

where C_p is the heat capacitance of sample system, T and T_0 are the temperature of sample system and heat bath, respectively. In a steady state denoted by process 2 in Fig. 2.11b, Eq. 2.22 is transformed into the relationship $Q = k(T - T_0) = k\Delta T$ due to the situation of $\mathrm{d}T/\mathrm{d}t = 0$, enabling to evaluate k. When the heat supply is stopped ($Q = 0$), temperature of the sample system gradually relaxes down to T_0 by following the relationship $C_p \mathrm{d}T/\mathrm{d}t = -k(T - T_0)$. By solving this differential equation, the function of relaxation curve (process 3 in Fig. 2.11b) is obtained as follows,

$$T = \Delta T \exp\left(-k\frac{t}{C_p}\right) = \Delta T \exp\left(-\frac{t}{\tau}\right) \tag{2.23}$$

where $\tau = C_p/k$ is the time constant. Therefore, C_p can be derived from τ or the fitting of relaxation curve. It is noted that obtained C_p contains the contribution from both sample itself and holder, so that it is necessary to subtract the latter signal measured beforehand.

2.6.2 Dilution refrigerator

The ^{3}He/^{4}He dilution refrigerator is utilized in order to realize extremely low temperature of 0.5 K or less. The He has two stable isotopes, i.e. ^{3}He which is Fermion and ^{4}He which is Boson. At very low temperature, their mixed solution undergoes phase separation into two phases; c phase which contains rich ^{3}He (~100 mol%) and d phase where ^{3}He is dilute (~6.4 mol%). In dilution refrigerator, these two phases are in contact. Here, ^{3}He has larger vapor pressure than ^{4}He, so that it can be selectively vaporized in the d phase. This results in the melting of ^{3}He from c phase into d phase with the endothermic process, enabling the continuous realization of extremely low temperature.

Chapter 3

Development of solid-phase epitaxy techniques

3.1 Introduction

Epitaxial thin film growth of R_2O_2Bi is a challenging issue because of high vapor pressure and strongly reductive state of Bi^{2-}. Indeed, PLD method was not applicable to the fabrication of Y_2O_2Bi epitaxial thin films on various lattice-matched substrates even in high vacuum ($< 4 \times 10^{-6}$ Pa), resulting in the preferential formation of cubic C-rare earth type $(Y,Bi^{3+})_2O_3$ epitaxial thin film (Fig. 3.1). In order to obtain Y_2O_2Bi epitaxial thin film, solid-phase epitaxy (SPE) is one promising technique because various layered oxide epitaxial thin films were successfully achieved for the first time via SPE [105, 106]. The main difficulties in fabrication of Y_2O_2Bi epitaxial thin film are high vapor pressure and unusual reductive state of Bi. Thus, ingenious approach overcoming the above problems will be desired.

In this chapter, two SPE methods were newly developed for Y_2O_2Bi: reductive SPE and multilayer SPE (Fig. 3.2). In the first method, Y_2O_2Bi epitaxial thin film was obtained through direct reaction between Y_2O_3 amorphous thin film and (Y,Bi) mixed powders via two-step heating in highly reductive condition, connecting to suppression of oxidation and evaporation of Bi (Section 3.2). However, low crystalline quality of the film hampered the evaluation of fundamental physical properties, especially the electrical conduction. Therefore, SPE method was improved by utilizing multilayered precursor

(Section 3.3). Highly crystalline Y_2O_2Bi epitaxial thin film enabled to observe intrinsic physical properties, demonstrating the two-dimensional electronic state with strong spin-orbit coupling.

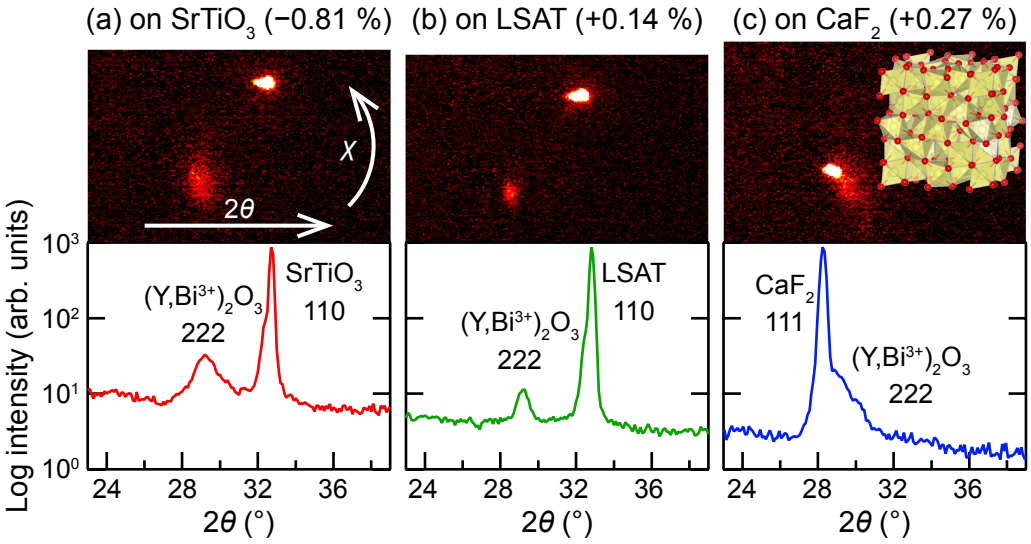

Figure 3.1: Two-dimensional XRD patterns (upper) and their projections (bottom) of films fabricated by PLD method deposited on (a) $SrTiO_3$, (b) $(LaAlO_3)_{0.3}(SrAl_{0.5}Ta_{0.5}O_3)_{0.7}$ (LSAT), and (c) CaF_2 substrates. Numerals between brackets denote lattice mismatch. Inset of (c) shows crystal structure of cubic Y_2O_3.

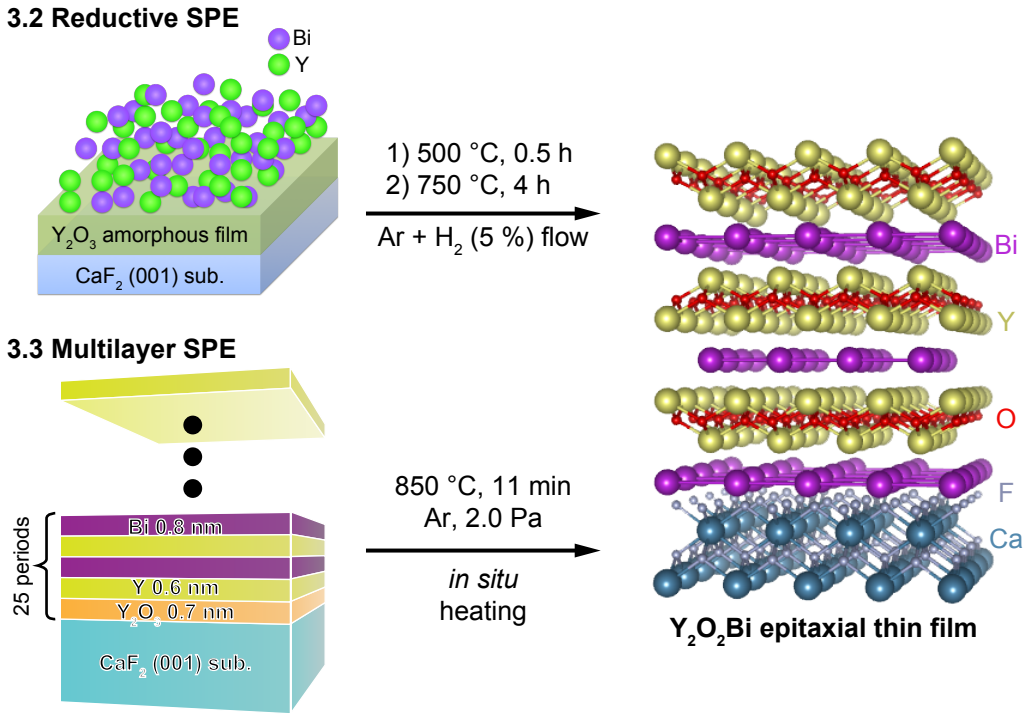

Figure 3.2: Schematic images of newly developed two SPE methods.

3.2 Development of reductive solid-phase epitaxy*

3.2.1 Experimental

A schematic procedure of reductive SPE is shown in Fig. 3.3. Y_2O_3 precursor films were deposited by PLD method on CaF_2 (001) substrate ($a/\sqrt{2}$ = 3.863 Å, 0.27 % of lattice mismatch) at room temperature under high vacuum ($< 10^{-6}$ Pa). The typical thickness of Y_2O_3 film was ~40 nm without any XRD peaks, indicating amorphous nature. Then, Y and Bi (purity: 3N) mixed powders with a molar ratio of 1 : 1 were sandwiched between two Y_2O_3 amorphous thin films. The sandwiched structure was covered with Ta foil in order to fix the structure. These operation was conducted in an Ar-filled glovebox. Finally, the product was heated by two-step at 500 °C for 0.5 h and at 750 °C for 4 h in $Ar + H_2$ (5 %) gas flow. Crystal structures of fabricated films were characterized by XRD with a two-dimensional detector using Cu Kα radiation.

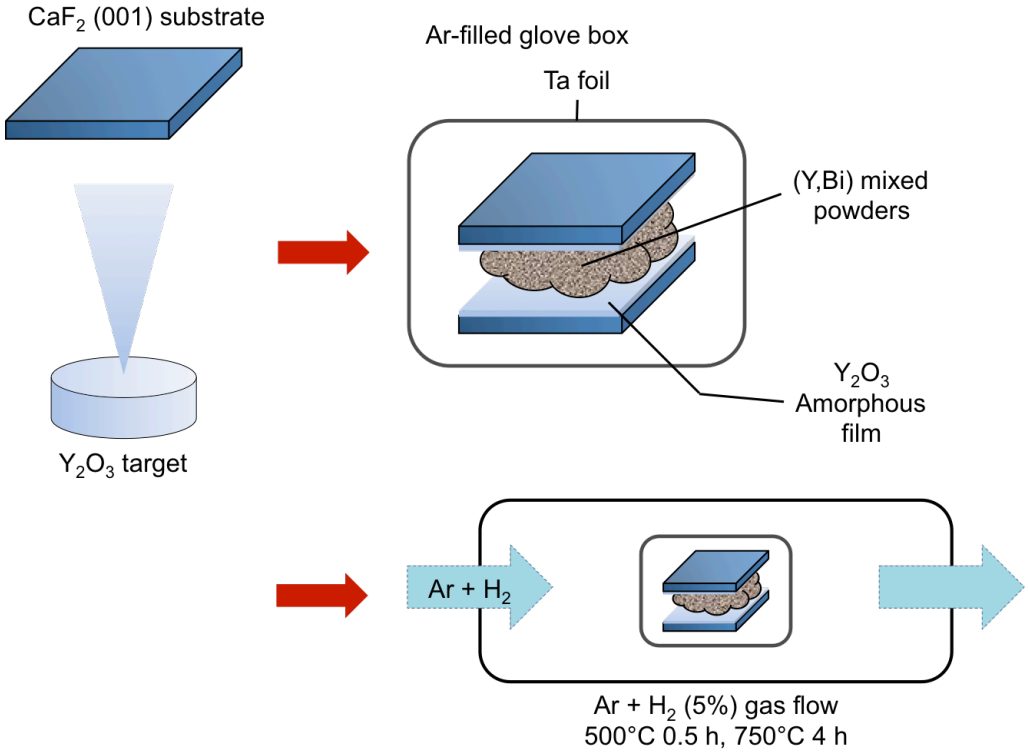

Figure 3.3: A schematic procedure of reductive SPE.

*This section contains the contents of the following publication. Reprinted with permission from R. Sei, T. Fukumura, T. Hasegawa, *Crystal Growth & Design* **14**, 4227 (2014). Copyright 2014 by American Chemical Society.

3.2.2 Fabrication results

Figure 3.4a-c shows a typical two-dimensional XRD pattern and its projections of an asymmetric plane for fabricated film. A spot-like peak corresponding to Y_2O_2Bi 103 diffraction was clearly observed adjacent to CaF_2 111 diffraction peak, indicating the single crystalline growth of Y_2O_2Bi phase. Furthermore, Y_2O_2Bi 00*l* diffraction peaks were observed along CaF_2 002 diffraction peak in the 2θ-θ XRD pattern of a symmetric plane (Fig. 3.4d), exhibiting *c*-axis oriented growth of the film. The calculated lattice constants were $a = 3.87$ Å and $c = 13.1$ Å, where the *c*-axis length showed small contraction in contrast to that in previous study ($a = 3.8734$ Å and $c = 13.2469$ Å) [58]. The reason will be discussed in Section 3.3. The epitaxial relationship between the film and the substrate was determined from Fig. 3.4a,d: Y_2O_2Bi [100] || CaF_2 [110] and Y_2O_2Bi [001] || CaF_2 [001]. These results represent the successful fabrication of Y_2O_2Bi epitaxial thin film with *c*-axis orientation. This is the first fabrication report of single crystalline R_2O_2Bi.

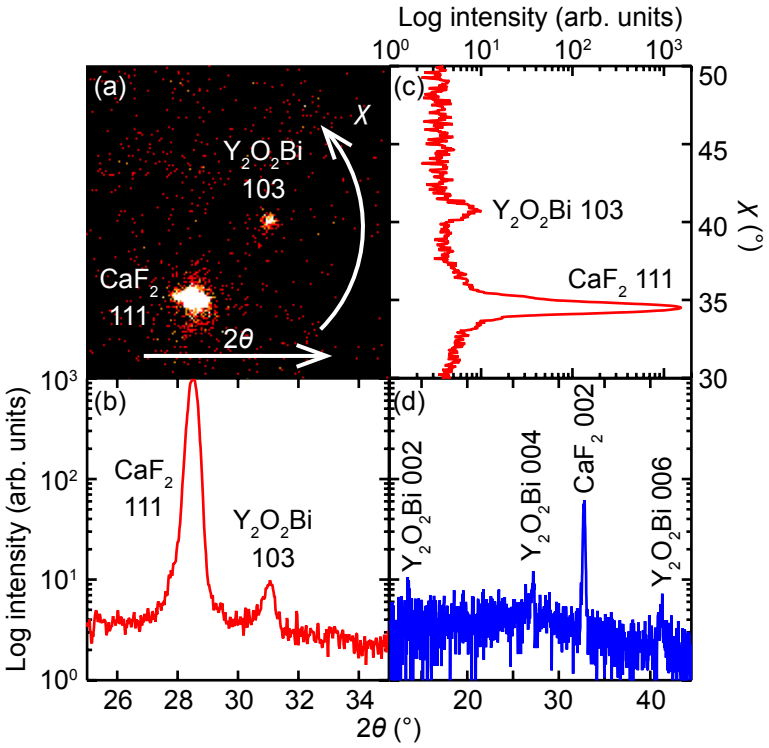

Figure 3.4: XRD patterns of the film fabricated by reductive SPE. (a) Two-dimensional XRD pattern of the asymmetric plane and its projection along (b) 2θ and (c) χ axes. (d) XRD pattern of the symmetric plane projected along 2θ axis.

3.2.3 Reaction mechanism

In this study, two-step heating process was utilized to grow Y_2O_2Bi epitaxial thin film. This technique was generally applied to the fabrication of polycrystalline R_2O_2Bi powders: mixed starting materials (Bi, R, and R_2O_3) with a stoichiometric composition were heated in evacuated silica tube at 500 °C, followed by heating at 750 °C [58]. A role of the first heating step can be considered as the formation of rare earth bismuthides RBi referring to R-Bi binary phase diagram [107]. Besides, other researchers have synthesized polycrystalline R_2O_2Bi and analogous R_2O_2Sb from the mixtures of Bi (Sb), RBi (RSb), and R_2O_3 [57, 59, 108]. These facts suggest that the formation of RBi was a key to achieve R_2O_2Bi phase. Furthermore, Y_2O_3 film was kept as the amorphous state even after the first heating step, confirmed by solely heating Y_2O_3 amorphous thin film under vacuum (Fig. 3.5); no RHEED image with the slight diffraction peak intensity indicates the mostly amorphous nature of Y_2O_3 film at the first heating step, followed by the complete crystallization at the second heating step. Therefore, reaction process of the reductive SPE can be represented by a following formula.

$$\begin{aligned} &[Y_2O_3 \text{ amorphous thin film}] + [\text{(Y,Bi) powders}] \\ &\xrightarrow[\text{Ar} + H_2\,(5\,\%)\text{ flow}]{500\,^\circ\text{C},\,0.5\,\text{h}} [Y_2O_3 \text{ amorphous thin film}] + \text{YBi} \\ &\xrightarrow[\text{Ar} + H_2\,(5\,\%)\text{ flow}]{750\,^\circ\text{C},\,4\,\text{h}} [Y_2O_2Bi \text{ epitaxial thin film}] \end{aligned} \tag{3.1}$$

In order to consider the details of formation mechanism of Y_2O_2Bi epitaxial thin

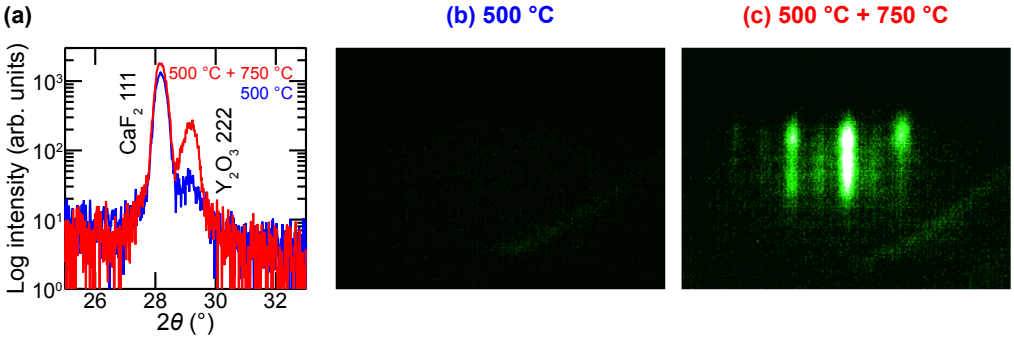

Figure 3.5: (a) XRD pattern of asymmetric plane for Y_2O_3 film on CaF_2 substrate heated at 500 °C and then at 750 °C. RHEED patterns of Y_2O_3 film after heating at (b) 500 °C and then at (c) 750 °C, representing the mostly amorphous phase and the crystallized phase, respectively.

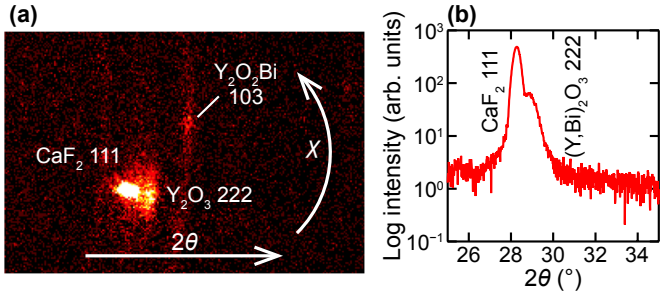

Figure 3.6: (a) Two-dimensional XRD pattern of the film after heating Bi and Y powders sandwiched between Y_2O_3 (001) epitaxial films. (b) The XRD pattern along the 2θ direction of the films fabricated from only Bi powder and Y_2O_3 amorphous film on CaF_2 substrate.

film, two referential experiments were conducted. The first topic was the replacement of precursor Y_2O_3 thin film from amorphous one to epitaxial one. Other conditions such as the mixing ratio of (Y,Bi) powders and the heating process was unchanged. This reaction can be summarized by a following formula.

$$\begin{aligned}&[Y_2O_3 \text{ epitaxial thin film}] + [(Y,Bi) \text{ powders}]\\ &\xrightarrow[Ar + H_2\ (5\,\%)\ \text{flow}]{1)\ 500\,^\circ\text{C},\ 0.5\,\text{h},\ \ 2)\ 750\,^\circ\text{C},\ 4\,\text{h}} [Y_2O_3 \text{ epitaxial thin film}]\\ &\qquad + [Y_2O_2Bi \text{ polycrystalline thin film}]\end{aligned} \tag{3.2}$$

Obtained film showed strong diffraction peak of single crystalline Y_2O_3 with a small amount of polycrystalline Y_2O_2Bi (Fig. 3.6a), implying that the growth of Y_2O_2Bi phase was hampered once Y_2O_3 was crystallized because of the high thermodynamical stability of Y_2O_3 phase.

The second topic was the role of Y. The film was fabricated from Y_2O_3 amorphous thin film and only Bi powder with the same heating condition, as represented by a following formula.

$$\begin{aligned}&[Y_2O_3 \text{ amorphous thin film}] + [\text{Bi powder}]\\ &\xrightarrow[Ar + H_2\ (5\,\%)\ \text{flow}]{1)\ 500\,^\circ\text{C},\ 0.5\,\text{h},\ \ 2)\ 750\,^\circ\text{C},\ 4\,\text{h}} [(Y,Bi^{3+})_2O_3 \text{ epitaxial thin film}]\end{aligned} \tag{3.3}$$

Obtained film was $(Y,Bi^{3+})_2O_3$ epitaxial thin film (Fig. 3.6b). Accordingly, Y served as a reductant for Bi in the first heating at 500 °C prior to the crystallization of the Y_2O_3

amorphous film. In other words, the presence of Bi^{2-} might be indispensable for the subsequent formation of Y_2O_2Bi.

With the above results taken into account, the formation mechanism of the Y_2O_2Bi epitaxial thin film is advocated as follows. The first heating at 500 °C promotes the formation of YBi with the reduction of Bi, while keeping the amorphous state of the Y_2O_3 film. The second heating at 750 °C stimulates the epitaxial growth of Y_2O_2Bi with the help of the lattice matched CaF_2 substrate. Hence, the first heating at 500 °C is indispensable to circumvent the formation of Y_2O_3 prior to the formation of Y_2O_2Bi.

3.2.4 Drawbacks of reductive solid-phase epitaxy

It was difficult to measure physical properties and to evaluate them properly due to some problems although Y_2O_2Bi epitaxial thin film was successfully obtained for the first time by developing reductive SPE. Figure 3.7 shows dark field optical microscope image of the film fabricated by reductive SPE method, indicating the large amount of powder residue at film surface. In addition, weak intensity of XRD peak (Fig. 3.4) indicated quite small crystalline volume of Y_2O_2Bi phase. These drawbacks hampered the fundamental evaluation of physical properties. Novel fabrication technique is desired to improve crystalline quality and to eliminate surface residue.

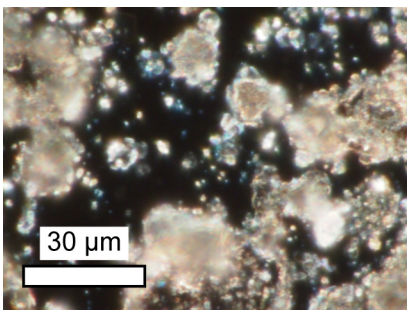

Figure 3.7: Dark field optical microscope image of the film fabricated by reductive SPE.

3.3 Development of multilayer solid-phase epitaxy[†]

3.3.1 Experimental

In order to overcome the above problems of reductive SPE, all of the reaction precursor was converted to the thin film form (Fig. 3.8). The multilayered precursor composed of Bi (0.8 nm thick), Y (0.6 nm), and Y_2O_3 (0.8 nm) layers was deposited on cubic CaF_2 (001) single-crystal substrate (lattice mismatch: 0.27 %) at ambient temperature by magnetron sputtering in Ar gas atmosphere as shown in Fig. 3.8. The subnanometer thick layers were crucial to enhance reaction efficiency and to preserve flat film morphology. The base and working pressure of sputtering chamber were less than 3.3×10^{-5} and 2.0 Pa, respectively. The each layer was deposited from pure Bi (4Nup), Y (3N), and Y_2O_3 (3N) targets in a sequence of [Y_2O_3/Y/Bi/Y/Bi] as a multilayer unit with 25 periods, followed by the deposition of Y cap layer because of volatile Bi. Subsequently, the precursor was *in situ* heated with heating rate of 30 °C/min up to 850 °C, and then the temperature was held for 11 min. The typical film thickness was around 90 nm.

Crystal structure was evaluated by XRD using Cu Kα_1 radiation. Surface morphology was observed by AFM. Electronic state was evaluated by XPS using Al Kα radiation in ultrahigh vacuum ($\sim 1 \times 10^{-6}$ Pa) after surface cleaning by *in situ* Ar sputtering. Samples were mounted on sample holder by using conducting carbon tape in order to prevent

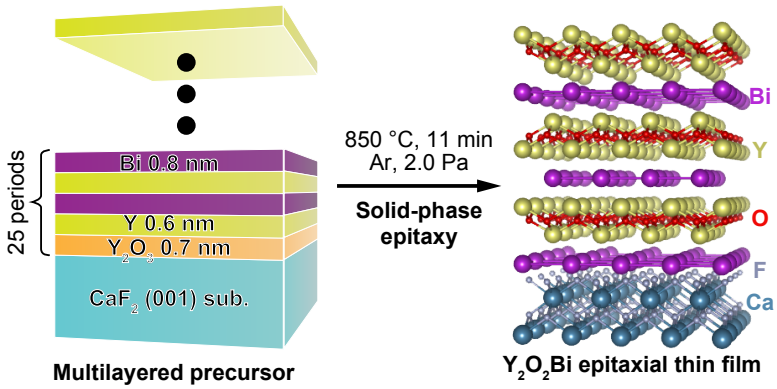

Figure 3.8: A schematic image of multilayer SPE. Right panel shows the crystal structure of Y_2O_2Bi (001) epitaxial thin film on CaF_2 (001) substrate.

[†]This section contains the contents of the following publication. Reprinted with permission from R. Sei, T. Fukumura, T. Hasegawa, *ACS Applied Materials & Interfaces* **7**, 24998 (2015). Copyright 2015 by American Chemical Society.

the sample from charge-up. In addition, the electron beam was irradiated for charge neutralization during the measurement. The XPS peak positions were calibrated by C 1s peak position (284.8 eV) [109]. Electronic transport properties were measured by standard four-probe method by PPMS equipped with sample rotator system.

3.3.2 Crystal Structure and valence state of Bi

Figure 3.9a shows XRD out-of-plane 2θ-θ scan of fabricated thin film. Sharp Y_2O_2Bi $00l$ peaks without any secondary phases were observed in contrast the result in reductive SPE. The lattice constants were $a = 3.880$ Å and $c = 13.129$ Å. The a-axis length was similar to that of polycrystalline powder ($a = 3.8734$ Å), whereas the c-axis length was slightly shorter ($c = 13.2469$ Å) [58] as discussed later. The FWHM of 0.53° for the Y_2O_2Bi 006 rocking curve in inset of Fig. 3.9a also indicated the high crystallinity. Four fold symmetry in XRD in-plane ϕ scan of the Y_2O_2Bi 103 peak (Fig. 3.9b) indicated the epitaxial relationships as Y_2O_2Bi [100] || CaF_2 [110] and Y_2O_2Bi [001] || CaF_2 [001], consistent with the result in reductive SPE. The film surface roughness was 1.1 nm in root mean square at 2 μm square (Fig 3.9c) without any surface residue. These results indicate the remarkable improvement of the Y_2O_2Bi epitaxial thin film than those with reductive SPE. Y_2O_2Bi epitaxial thin films were not obtained on oxide substrates such as $SrTiO_3$ and $LaAlO_3$ like reductive SPE.

From the comparison between two precursors with different sequences, [Y_2O_3/Y/Bi]

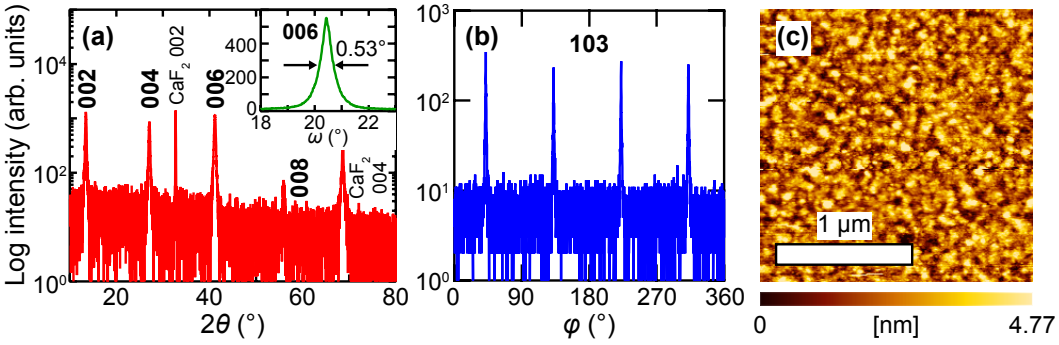

Figure 3.9: (a) XRD out-of-plane 2θ-θ scan of the Y_2O_2Bi epitaxial thin film on the CaF_2 substrate. Inset shows 006 rocking curve. (b) XRD in-plane ϕ scan of 103 peak. $\phi = 0°$ corresponded to the CaF_2 (100) plane. (c) Atomic force microscope planar image of the Y_2O_2Bi epitaxial thin film.

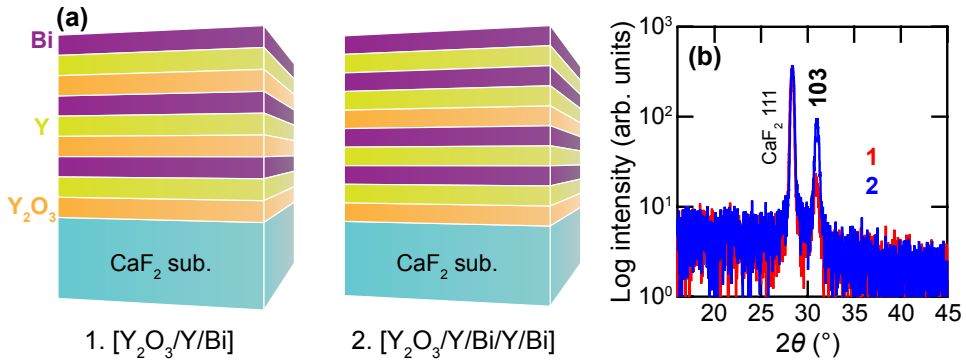

Figure 3.10: (a) Schematic images of two-types of multilayered precursors. (b) The comparison of XRD patterns of the Y_2O_2Bi epitaxial thin films fabricated from both types of multilayered precursors.

multilayer and [Y_2O_3/Y/Bi/Y/Bi] multilayer, the latter showed larger XRD peak intensity (Fig. 3.10). This result suggests that the latter multilayer promoted an efficient formation of YBi alloy due to the larger number of Y/Bi interface in addition to high reaction efficiency of these multilayers compared with powder precursor. These factors were indispensable to achieve Y_2O_2Bi phase, enabling one step heating procedure and highly crystalline quality.

Figure 3.11 shows an XPS spectrum of Y_2O_2Bi epitaxial thin film fitted by two doublet peaks of Bi 4f and Y 3d. The Bi $4f_{7/2}$ peak was located at 156.7 eV, which is lower than that of Bi metal (157.0 eV) [109] and comparable with that of Bi anionic state (Bi^-–Bi^{3-}) in $LaGaBi_2$ (156.6 eV) [110] and R_3MnBi_5 (156.7–156.8 eV) [111], indicating anionic state of Bi in Y_2O_2Bi. The Y $3d_{5/2}$ peak was located at 157.9eV, which was between those of Y_2O_3 (156.7eV) [112] and YF_3 (159.7 eV) [113], confirming Y^{3+} state as well as the coexistence of Y–O and Y–F bonds in $[Y_2O_2]^{2+}$ layer as explained below. These results verify Bi^{2-} state in Y_2O_2Bi.

Figures 3.12a–c show XPS depth profile along film growth direction. Near the film surface, Bi loss due to the volatility under heating treatment was observed (Fig. 3.12a). The chemical composition was almost constant inside the film (Fig. 3.12b). In Fig. 3.12a,b, no peak shift was observed. At the film/substrate interface, all peaks were abruptly shifted about 2 eV to lower binding energy (93 nm in depth, Fig. 3.12c). This shift was attributed to the sample charge-up probably due to too small volume of sputtered conducting Y_2O_2Bi film, because another Y_2O_2Bi film without ground by carbon tape showed similar shift

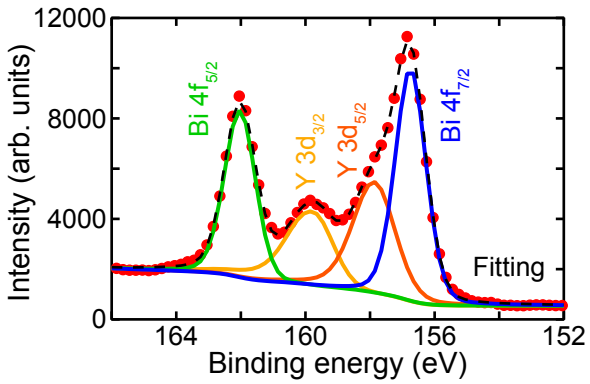

Figure 3.11: XPS spectrum of the Y_2O_2Bi epitaxial thin film fitted by Bi 4f and Y 3d doublet peaks.

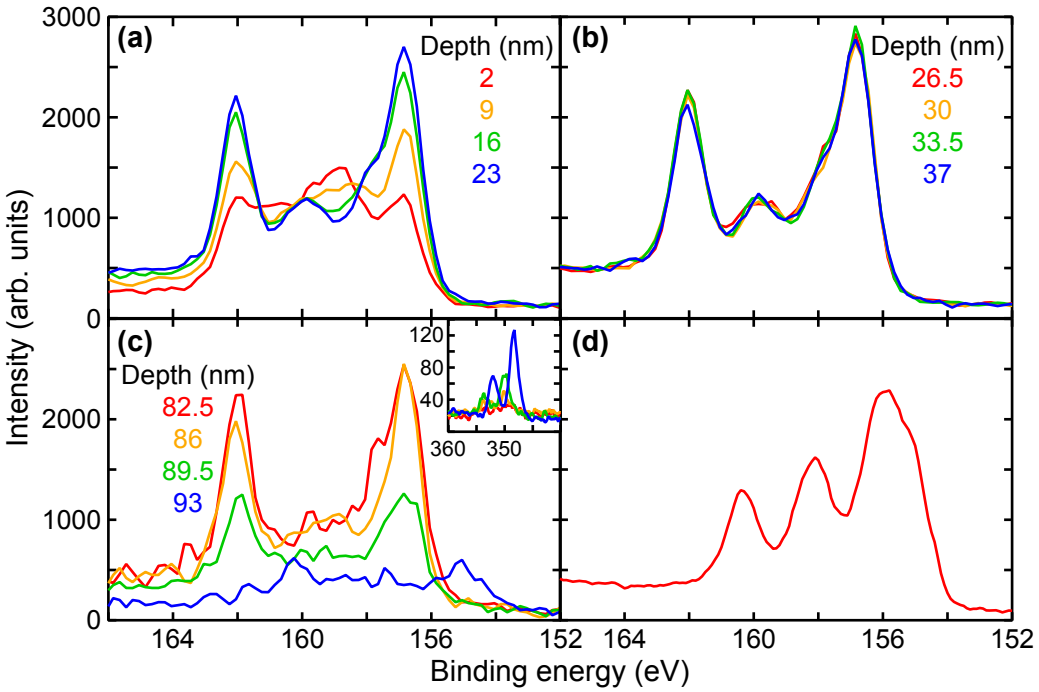

Figure 3.12: XPS depth profile of Bi 4f and Y 3d peaks (a) near film surface, (b) inside the film, and (c) at the film/substrate interface. The inset of (c) shows Ca 2p spectra. (d) XPS spectrum of Bi 4f and Y 3d peaks measured without ground by carbon tape.

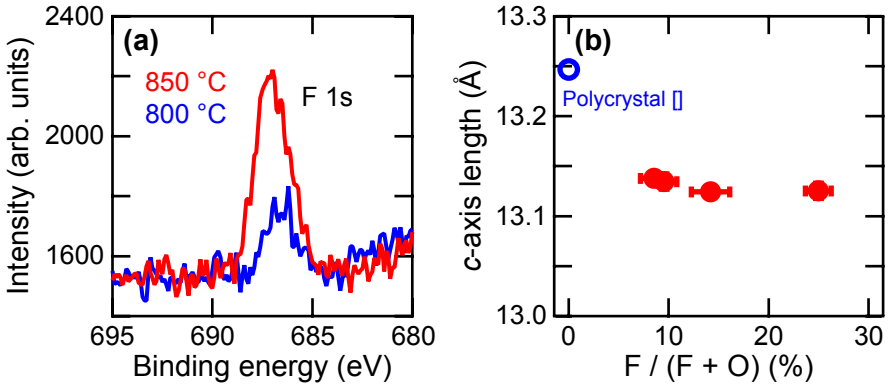

Figure 3.13: (a) F 1s spectra of the Y_2O_2Bi epitaxial thin films with different heating temperature. (b) F content dependence of *c*-axis length of the Y_2O_2Bi epitaxial thin films.

(Fig. 3.12d). Accordingly, XPS spectra measured in this study without that of excessively sputtered film were not influenced by the sample charge-up and the fluctuation of stoichiometry, hence these spectra indicated Bi^{2-} valence state.

It is noted that F was incidentally doped into the film due to the migration from the CaF_2 substrate during heating, confirmed by XPS measurement as shown in Fig. 3.13a. The amount of F in the film was higher for higher heating temperature. The *c*-axis length of Y_2O_2Bi film decreased with the presence of F (Fig. 3.13b), suggesting the substitution of F for O site due to the smaller ionic radius of F^- than that of O^{2-}, as was observed in structurally similar *R*FeAsO [6] and *R*OBiS$_2$ [114].

3.3.3 Electronic transport properties

Figure 3.14a shows the ρ-T curve of Y_2O_2Bi epitaxial thin film. The film showed metallic behavior with one order smaller ρ than that of polycrystalline powder sample ($\sim 10^3$ μΩ cm) [58] as a result of single crystallization of Y_2O_2Bi. The magnetic field dependence of Hall resistance (Fig. 3.14c) showed negative slope at any temperature indicating the *n*-type conduction. This result is contradictory to the *p*-type conduction derived from the Seebeck measurement in the previous report [58]. The F content of $\sim 5 \times 10^{21}$ cm^{-3} evaluated from XPS measurement was apparently smaller than that of maximum electron carrier density $\sim 5 \times 10^{22}$ cm^{-3} (Fig. 3.14b), suggesting either the intrinsic *n*-type conduction like other Bi square net compounds $CaMnBi_2$ [72] and $LaPd_{1-x}Bi_2$ (3.7×10^{22} cm^{-3}) [47] or the complicated multiband conduction although the

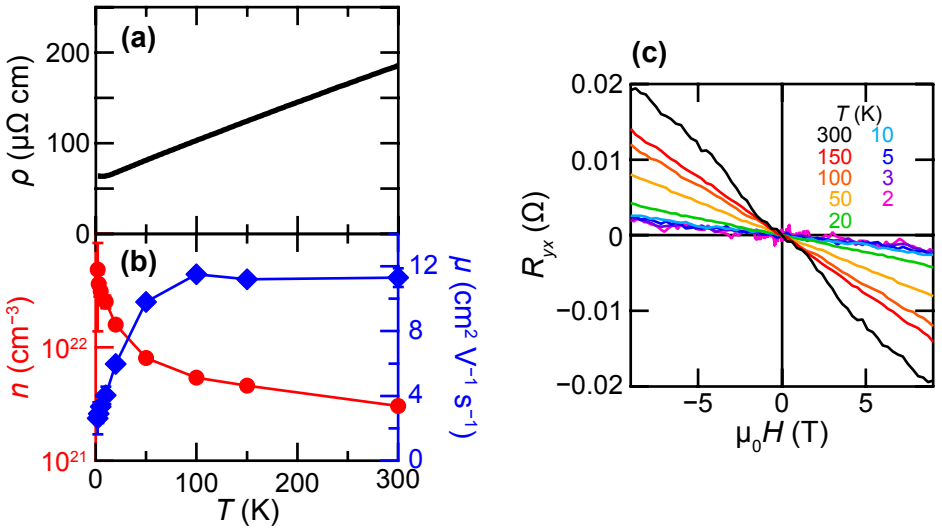

Figure 3.14: Temperature dependences of (a) electrical resistivity, (b) carrier density (red), and carrier mobility (blue) of the Y_2O_2Bi epitaxial thin film. (c) Magnetic field dependence of Hall resistance (R_{yx}). R_{yx} was derived from $R_{yx} = [R_{yx}(+H) - R_{yx}(-H)]/2$ in order to eliminate R_{xx} component that is even function of H.

Hall resistance was linear with magnetic field. The Hall mobility except below 50 K was over 10 $cm^2\ V^{-1}\ s^{-1}$ (Fig. 3.14b), which is higher than those of normal metals.

Figure 3.15a shows magnetoconductance at 2 K in out-of-plane magnetic field. The rapid reduction of conductance from zero field was scarcely observed in the other Bi square net compounds. This cusp-like variation is typical behavior of weak anti-localization (WAL) effect. The WAL effect was usually observed in strong spin-orbit coupling system such as two-dimensional electron gas in narrow gap semiconductor heterostructure [115] and the topological insulator [116, 117]. In two-dimensional electronic system, the Hikami-Larkin-Nagaoka (HLN) model can be applied to the WAL effect [118]. In the magnetic field range up to 9 T in this study, the magnetoconductance is described by the original HLN equation [118–120] expressed as,

$$\Delta G(B) = -\alpha \frac{e^2}{2\pi^2\hbar}\left[2\eta\left(\frac{B_e}{B}\right) - 2\eta\left(\frac{B^z_{SO} + 2B^x_{SO} + B_\phi}{B}\right) + \eta\left(\frac{B_\phi}{B}\right) - \eta\left(\frac{4B^x_{SO} + B_\phi}{B}\right)\right] \tag{3.4}$$

where $\Delta G(B) = G(B) - G(0)$, α is the WAL coefficient equal to -0.5 in ideal two-dimensional limit of symplectic case such as surface state of topological insulator [116–118][‡], e is the elementary charge, $\hbar$ is the Dirac's constant, η function is defined as

[‡]The α equal to 1 or 0 corresponds to orthogonal or unitary case, respectively [118].

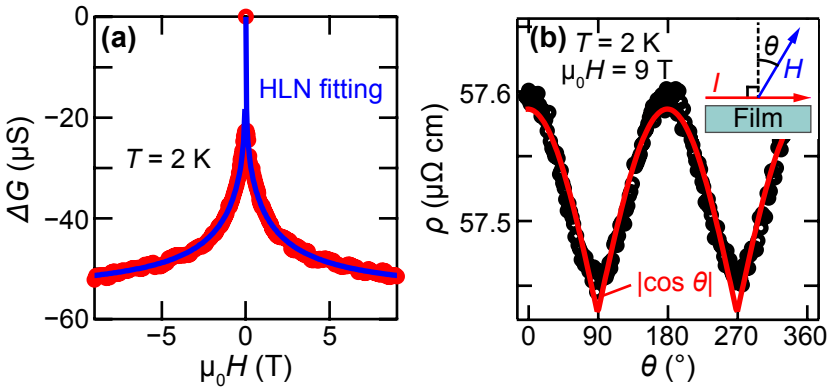

Figure 3.15: (a) Magnetoconductance at 2 K superposed with fitting curve by the HLN model. (b) Angular dependence of MR at 2 K and 9 T. Inset shows the measurement configuration: I denotes current along the ab-plane, and θ denotes the tilt angle between the film normal and applied magnetic field H.

$\eta(x) = \ln(x) - \psi((1/2) + x)$, ψ is the digamma function, $B_i = 1/4eL_i^2 (i = \mathrm{e}, \mathrm{SO}, \phi)$, L_e is the elastic scattering length, L_SO is the spin-orbit scattering length along x or z direction, L_ϕ is the phase coherence length, and $B = \mu_0 H$ (μ_0: vacuum permeability). Fitting parameters were α and L_i. Here, the x and z directions correspond to the a- (or b-) and c-axis direction of Y_2O_2Bi, respectively [118, 120]. The blue line in Fig. 3.15a represents the fitting result of the HLN model. The obtained $\alpha = -0.49$ was close to the ideal two-dimensional limit of symplectic case and similar to that of the bulk insulating topological insulator Bi_2Se_2Te (−0.56) [117] rather than that of the bulk conducting topological insulator Bi_2Te_3 (−0.39) [116]. The obtained scattering lengths were $L_\mathrm{SO}^x = 71.9$ nm, $L_\mathrm{SO}^z = 14.5$ nm, and $L_e = 31.3$ nm. The relations $L_\mathrm{SO}^x > L_\mathrm{SO}^z$ and $L_e > L_\mathrm{SO}^z$ indicated the two-dimensional nature and the strong spin-orbit coupling, respectively [118, 120]. The obtained $L_\phi = 724$ nm comparable to those of Bi_2Se_2Te and Bi_2Te_3 (318 and 331 nm, respectively) [116, 117] ensured the reasonable fitting result. These results indicated not only two-dimensional nature but also strong spin-orbit coupling in Y_2O_2Bi originating from Bi^{2-} square net, similar to the topological insulator. The two-dimensional electronic transport was also confirmed in angular dependence of magnetoresistance (MR). Figure 3.15b shows angular dependence of MR at 2 K and 9 T. MR was well-fitted to $|\cos\theta|$, indicating that MR varied by field component perpendicular to conducting channel [69, 121], i.e. Bi^{2-} square net. The small change in MR compared with $SrMnBi_2$ and $CaMnBi_2$ was probably due to the absence of the spin

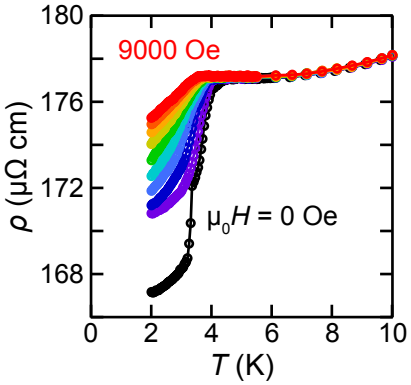

Figure 3.16: Onset of superconductivity observed in a certain Y_2O_2Bi epitaxial thin film.

fluctuation [69, 71].

3.3.4 Onset of superconductivity

Figure 3.16 shows the ρ-T curves at low temperature and various fields of a certain Y_2O_2Bi epitaxial thin film. Notably, a sudden resistance drop was observed around 4.0 K for the first time in this compound and the transition was suppressed by applying magnetic field, suggesting superconducting transition. The onset of superconductivity was observed in several samples with varied transition temperature T_c from 3 to 4 K. In various compounds composed of Bi, Y, and O elements, only a simple Bi shows superconductivity: Bi element (T_c = 5.2 μK) [122], high pressure phase (3.9 K for > 2.55 Pa, 7.2 K for > 2.7 Pa, 8.3 K for > 7.7 Pa) [123–126], nanowire (7.2 and 8.3 K) [126], granular film (4.3 K) [127], and amorphous phase (6.12 K) [128]. Observed T_c of Y_2O_2Bi was different from those in superconducting Bi, indicating intrinsic superconductivity in Y_2O_2Bi. However, Meissner effect and zero-resistance confirming bulk superconducting nature were not observed. Therefore, superconducting volume fraction seemed to be very small and the driving force to induce superconductivity was unclear.

3.4 Conclusion

I succeeded in the fabrication of $ThCr_2Si_2$-type Y_2O_2Bi epitaxial thin film for the first time by developing two novel SPE methods: reductive SPE and multilayer SPE. In reductive SPE, Bi metal was reduced by Y metal without the formation of the C-rare

earth type Y_2O_3 at the first heating, followed by the epitaxial growth of Y_2O_2Bi with the Bi^{2-} square net on the lattice matched CaF_2 substrate at the second heating. This concept would be useful for the epitaxial growth of not only layered $ThCr_2Si_2$-type and analogous compounds, but also other reductive compounds. However, the surface residue hampered the fundamental evaluation of physical properties.

Therefore, I improved reductive SPE by utilizing multilayered precursor. Crystalline quality of Y_2O_2Bi epitaxial thin film was dramatically enhanced and unusual valent of Bi^{2-} state was directly observed. This multilayer SPE was universally applicable to epitaxial growth of other R_2O_2Bi such as Ce_2O_2Bi [129] and Dy_2O_2Bi (Appendix D). Magnetotransport measurements indicated the two-dimensional electronic nature in addition to strong spin-orbit coupling in the Bi^{2-} square net, reminiscent of the topological insulator. Onset of superconducting transition was observed around 4 K although superconducting volume fraction was quite small. R_2O_2Bi is expected to be a good platform to investigate the exotic two-dimensional electronic system with the strong spin-orbit coupling.

Chapter 4

Two-dimensional superconductivity in polycrystalline Y_2O_2Bi*

4.1 Introduction

Superconducting Bi square net would provide a new platform to explore the interaction between low-dimensional superconductivity and strong spin-orbit coupling such as topological superconductivity [130], owing to the possibility of two-dimensional topological insulator [79]. So far, $AMBi_2$ compounds with Bi^- square net have been extensively studied and several compounds were reported to be superconducting [47, 82, 88]. However, the superconductivity was often subject to small superconducting volume fraction or was attributed to neighboring layer rather than Bi^- square net (see Subsection 1.2.4 and Table 4.1), indicating little hope to achieve superconducting Bi square net in $AMBi_2$ compounds.

$ThCr_2Si_2$-type layered R_2O_2Bi (R: rare earth) is a new series of compounds composed of conducting Bi^{2-} square net and insulating $[R_2O_2]^{2+}$ layer [58]. This compound can be regarded as a counterpart of iso-structural FeAs-based high temperature superconductor $BaFe_2As_2$ [12] with their inverted carrier conduction paths, Bi^{2-} square net and $[Fe_2As_2]^{2+}$ layer, respectively (Fig. 4.1), possibly connecting to the emergence of superconductivity. However, R_2O_2Bi has been already concluded as non-superconducting [26],

*This section contains the contents of the following publication. Reprinted with permission from R. Sei, S. Kitani, T. Fukumura, H. Kawaji, T. Hasegawa, *Journals of the American Chemical Society* **138**, 11085 (2016). Copyright 2016 by American Chemical Society.

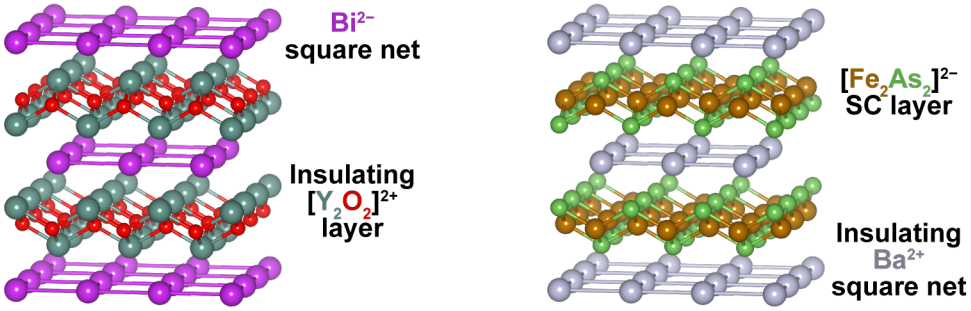

Figure 4.1: The crystal structures of $ThCr_2Si_2$-type Y_2O_2Bi (left) and $BaFe_2As_2$ (right). SC: superconducting.

and the application of chemical pressure just changes the electrical transport properties from insulating in La_2O_2Bi to metallic in Er_2O_2Bi [58]. In addition, quite large carrier density ($\geq 10^{22}\,cm^{-3}$, Subsection 3.3.3), which is consistent with one anti-bonding electron per one Bi^{2-} anion (Subsection 1.2.1), demonstrates no effect of further carrier doping, indicating conventional approach was not applicable to induce superconductivity in R_2O_2Bi.

In iso-structural $BaFe_2As_2$, decreasing inter-layer distance by applying uniaxial pressure along *c*-axis direction weakens the superconducting properties, similarly observed in cuprate high temperature superconductor [131, 132]. This is consistent with the very small superconducting volume in F doped Y_2O_2Bi epitaxial thin film with *c*-axis shrinking (Subsection 3.3.4). Therefore, inverted effect, i.e., expanding *c*-axis length would be one alternative route to induce superconductivity in Bi^{2-} square net of R_2O_2Bi. In this study, I discovered two-dimensional superconductivity of Bi^{2-} square net in polycrystalline Y_2O_2Bi at about 2 K via chemical control of structure. It is noted that the superconductivity was not observed in pristine Y_2O_2Bi but induced by expanding Bi^{2-} inter-net distance through excessive O incorporation into hidden interstitial site. This result indicates an important role of enhanced two-dimensionality of Bi^{2-} square net in emergence of the superconductivity, and provides new chemical approach to explore the superconductivity in layered compounds.

Table 4.1: Properties of Bi square net compounds. SC: superconducting

Compounds	T_c (K)	Crystal structure (space group)	Principle SC component	Notes	References
$CeNi_xBi_2$	4.2	$ZrCuSi_2$ (*P4/nmm*)	Bi^- square net [82] or $NiBi_3$ impurity [46, 83, 84] (under debate)	Small SC volume fraction (< 17 %) except for ref. [82]. No Ni deficiency dependence of T_c, irreproducible superconductivity, and the same T_c with that of $NiBi_3$.	[46, 82–84]
$LaPd_xBi_2$	2.1	$ZrCuSi_2$ (*P4/nmm*)	Pd	Effect of Pd vacancy on Fermi surface and CDW.	[47, 87]
$Bi/SrMnBi_2$	5.7		Strained Bi	Blob-like Bi on $SrMnBi_2$ single crystal showed superconductivity due to the strain. Large sample dependence.	[88]
$RENi_xBi_2$ (*RE*: Y, La, Nd)	~4	$ZrCuSi_2$ (*P4/nmm*)	Bi^- square net [82] or $NiBi_3$ impurity [46] (under debate)	Small SC volume fraction (1–17 %) and similar T_c with that of $NiBi_3$	[46, 82]
$RENi_xBi_2$ (*RE*: Pr, Nd, Sm, Gd, Tb, Dy)	–	$ZrCuSi_2$ (*P4/nmm*)	–	AF transition at 3–10 K.	[46]
$CePd_xBi_2$	–	$ZrCuSi_2$ (*P4/nmm*)	–	AF transition at 6 K.	[47]
$SrMnBi_2$	–	$SrZnBi_2$ (*I4/mmm*)	–	AF transition at 290 K. Anisotropic Dirac fermion.	[67, 69]
$CaMnBi_2$	–	$ZrCuSi_2$ (*P4/nmm*)	–	AF transition at 250 K. Anisotropic Dirac fermion.	[71, 72]

4.2 Experimental

Polycrystalline Y_2O_2Bi samples were synthesized as follows. The starting materials were Bi (3N), Y (3N), and Y_2O_3 (3N) powders. The Y_2O_3 powder was heated at 350 °C for 1 day before use in order to eliminate absorbed moisture. Nominal amount of $Y_2O_xBi_{1.5}$ ($1.1 \leq x \leq 2.0$) mixed powders were pressed into pellets by ~5 MPa and covered with Ta foil. The excess amount of Bi was added in order to compensate volatile Bi and remove burnable Y residue in air by forming YBi, and Bi residue evaporated from sample pellets[†]. This operation was performed in Ar-filled glovebox. The pellets were heated in evacuated quartz tubes at 500 °C for 7.5 h, followed by heating at 1000 °C for 20 h. The products were ground in the glovebox, pressed into pellets in air by ~30 MPa, covered with Ta foil, and heated in evacuated quartz tubes at 1000 °C for 10 h. Crystal structures were evaluated by powder XRD using Cu Kα radiation. Rietvelt refinements were performed by RIETAN-FP [95]. Magnetic properties were measured by SQUID magnetometer. Electrical transport properties were evaluated by standard four-probe method. Specific heat measurements were conducted by the thermal relaxation method using a homemade calorimeter with a ^{3}He/^{4}He dilution refrigerator [133]. Out-of-plane and in-plane magnetic field (H) direction was defined to be H parallel to and normal to the pellet surface, respectively, because of the preferential c-axis orientation as discussed later.

4.3 Crystal sructure

Figure 4.2 shows powder XRD patterns of all Y_2O_2Bi samples ($1.1 \leq x \leq 2.0$). Refined structural parameters were summarized in Table 4.2. Most of diffraction peaks were completely fitted by simulation as $ThCr_2Si_2$-type Y_2O_2Bi phase (Fig. 4.3a), while several non-superconducting minor phases appeared depending on prescribed amount of O; YBi for reductive condition ($1.1 \leq x \leq 1.4$) and Y_2O_3 for oxidative condition ($1.5 \leq x \leq 2.0$) (Fig. 4.3b). The typical atomic ratio of Y/Bi in Y_2O_2Bi phase was almost stoichiometric, e.g. 2.02 for both reductive ($x = 1.2$) and oxidative ($x = 1.6$) conditions, evaluated

[†]The nominal amount of Bi was changed to 1.8, 1.7, and 1.6 for $x = 1.1$, 1.2, and 1.3, respectively, in order to compensate increased Y residue.

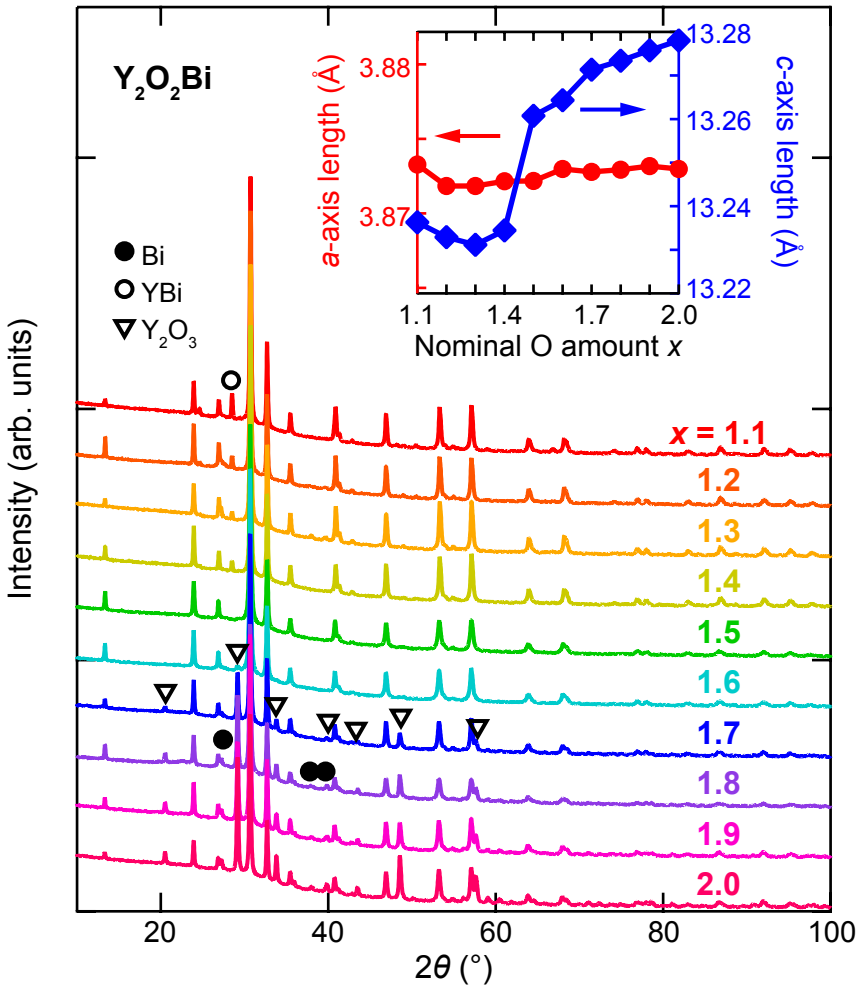

Figure 4.2: XRD patterns of Y_2O_2Bi samples. Inset shows lattice constant of each sample. Results of the Rietveld refinements are seen in Table 4.2 and Fig. 4.3.

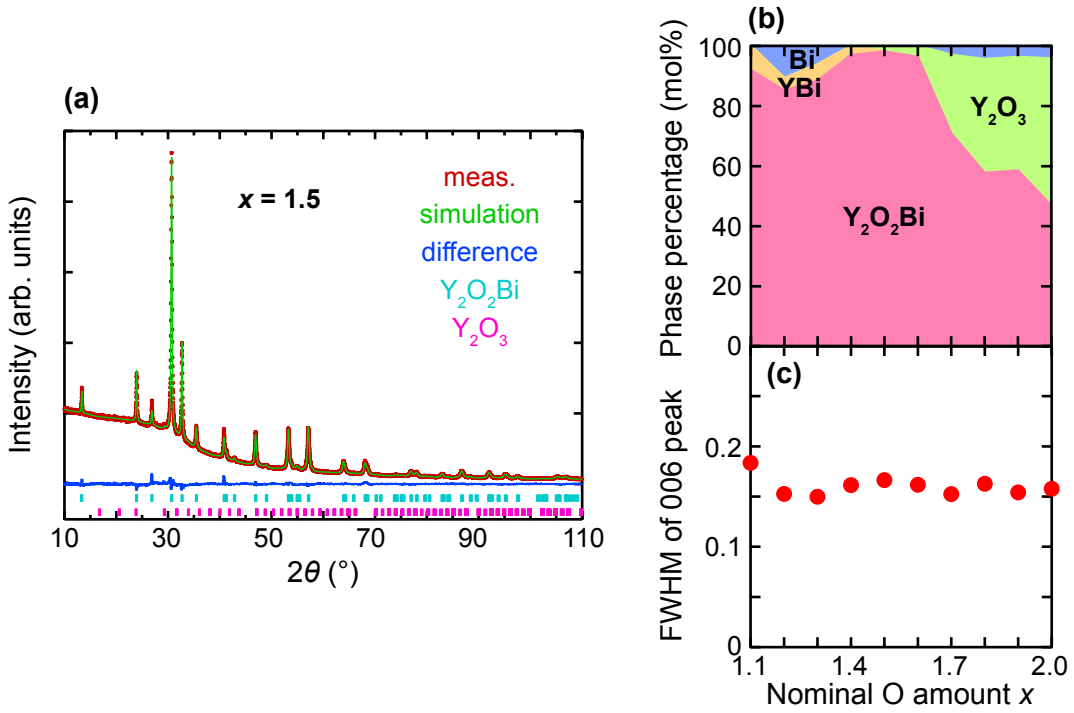

Figure 4.3: (a) Typical result of Rietveld refinement for $x = 1.5$. (b) Phase diagram for Y_2O_2Bi samples. (c) The FWHM of 006 peaks in 2θ-θ patterns for Y_2O_2Bi samples.

by inductively coupled plasma mass spectroscopy and Rietveld refinement. The lattice constants for reductive samples were similar to those of Y_2O_2Bi polycrystalline powder ($a = 3.8734$, $c = 13.2469$ Å) [58], indicating their ideal composition (inset of Fig. 4.2). On the other hand, the c-axis showed abrupt expansion for $x = 1.5$ followed by gradual increase with almost constant a-axis toward $x = 2.0$ (inset of Fig. 4.2). This expansion was possibly caused by O incorporation between Bi^{2-} square net and adjacent Y termination layers implied by jump of those distance between samples $x = 1.4$ and $x = 1.5$ in contrast with continuously changed distance between Y termination layer and adjacent O layer (Fig. 4.4). The FWHM of 006 diffraction peaks in 2θ-θ patterns showed similar values among all Y_2O_2Bi samples, indicating that O was homogeneously incorporated into Y_2O_2Bi framework in each sample without deterioration of the crystalline quality (Fig. 4.3c). Thus, I succeeded in introducing chemical control of structure by varying the amount of O in Y_2O_2Bi. This incorporation process into hidden interstitial site was essentially different from conventional intercalation technique into van del Waals gap: the carrier doping was critical for tuning physical properties in the latter case [2,4,33,34], while the structural control was essential in the former case as discussed later.

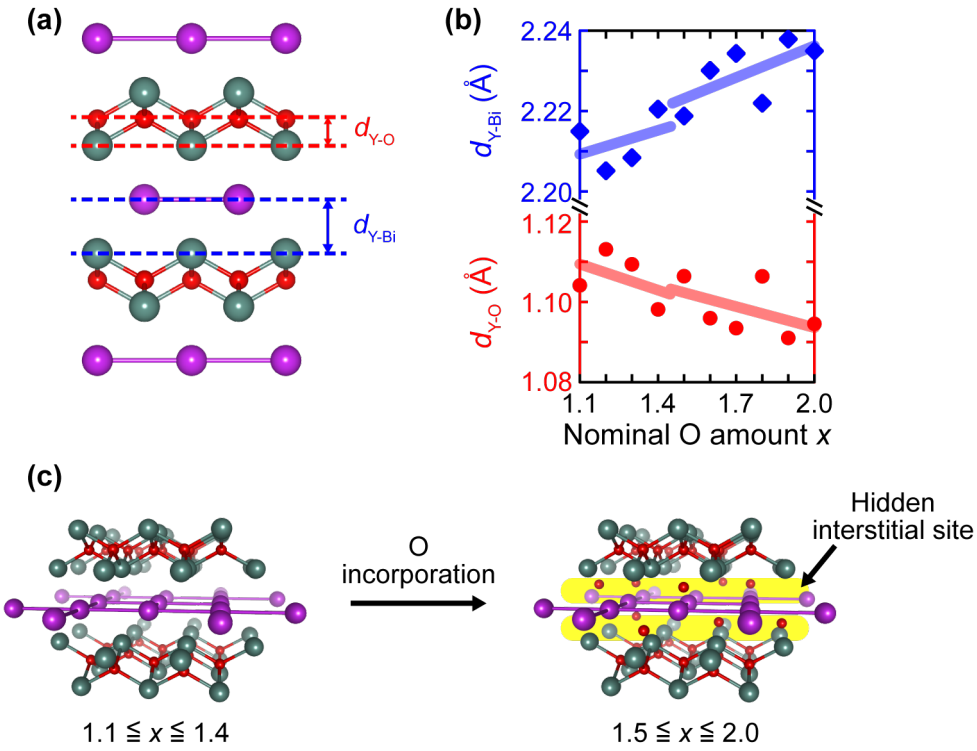

Figure 4.4: (a) Crystal structure of Y_2O_2Bi along [100] direction. The d_{Y-O} (d_{Y-Bi}) denotes the distance between Y termination layer and adjacent O (Bi) layer. (b) The sample dependence of d_{Y-O} and d_{Y-Bi}. Thick lines correspond to the least square fitting lines. (c) Schematic image of the local crystal structure around Bi^{2-} square net without (left) and with (right) O incorporation into Wyckoff position 8*g* site (0, 0.5, 0.09).

Table 4.2: Summary of structural data in Y_2O_2Bi samples

x	1.1	1.2	1.3	1.4	1.5	1.6	1.7	1.8	1.9	2.0
Space group	*I4/mmm*	*I4/mmm*	*I4/mmm*	*I4/mmm*	*I4/mmm*	*I4/mmm*	*I4/mmm*	*I4/mmm*	*I4/mmm*	*I4/mmm*
a (Å)	3.87327(11)	3.87183(12)	3.87183(17)	3.87215(11)	3.87217(18)	3.8730(2)	3.87278(14)	3.87329(2)	3.87317(14)	3.87297(13)
c (Å)	13.2363(4)	13.2329(4)	13.2311(6)	13.2345(4)	13.2607(6)	13.2643(7)	13.2713(5)	13.2734(8)	13.2758(5)	13.2780(5)
V (Å^3)	198.573(10)	198.375(11)	198.348(15)	198.431(10)	198.828(16)	198.964(18)	199.050(13)	199.095(19)	199.156(12)	199.168(12)
Y z[‡]	0.33266(14)	0.33336(14)	0.33309(15)	0.33222(11)	0.33268(15)	0.33187(13)	0.33164(13)	0.3326(2)	0.33143(13)	0.33168(15)
Purity (mol%)	91.9	85.1	88.4	96.9	98.1	96.3	70.9	57.7	58.5	46.8
R_{wp}	2.844	2.828	3.298	2.600	2.595	2.875	1.999	2.406	2.078	2.238
R_e	1.587	1.592	1.590	1.626	1.609	1.614	1.579	1.574	1.577	1.581
S	1.792	1.776	2.074	1.599	1.613	1.781	1.266	1.528	1.318	1.416

[‡]Wyckoff positions: Bi on the 2*a* site (0, 0, 0), Y on the 4*e* site (0, 0, *z*), and O on the 4*d* site (0, 0.5, 0.25).

4.4 Emergence of bulk superconductivity

4.4.1 Magnetic properties

Figure 4.5a shows the χ-T curves in zero-field cooling (ZFC) and field cooling (FC) at 5 Oe. No diamagnetic signal was observed for reductive samples ($1.1 \leq x \leq 1.4$), whereas large diamagnetic signals due to the Meissner effect were observed around 2 K for oxidative samples ($1.5 \leq x \leq 2.0$) corresponding to the superconducting transition. The critical temperature T_c was monotonically increasing function of nominal amount of O, i.e., x. The magnetization curve at 2 K for $x = 1.9$ indicated the type-II superconductivity with a lower critical magnetic field of 18 Oe deduced from the magnetization minimum (inset of Fig. 4.5a). Shielding volume fractions calculated from the magnetization curves for oxidative samples confirmed bulk superconductivity of Y_2O_2Bi (Fig. 4.5b). The shielding volume fraction over 100 % was caused by the polycrystalline nature of the samples.

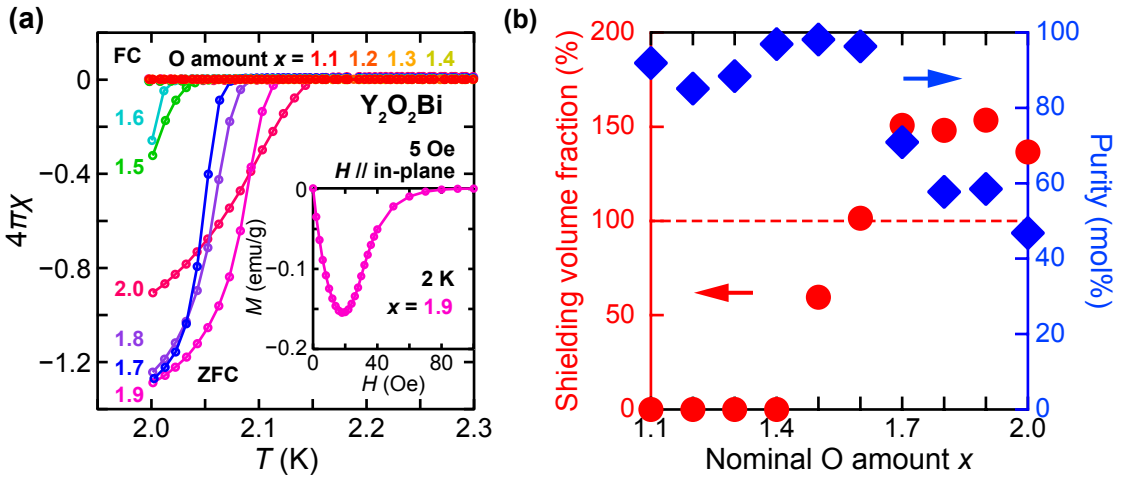

Figure 4.5: (a) The χ-T curves with ZFC and FC process at 5 Oe. Inset shows magnetization curve at 2 K for $x = 1.9$. (b) Evolution of shielding volume fraction and Y_2O_2Bi phase purity.

4.4.2 Electrical transport properties and two-dimensional superconductivity

Hereafter, we mainly discuss the properties of $x = 1.6$ because of the highest purity of Y_2O_2Bi phase (96.3 mol%) and the bulk superconductivity with sufficiently high shielding volume fraction (Fig. 4.5b). Figure 4.6a shows the ρ-T curves at various magnetic fields. The sample showed metallic behavior (inset of Fig. 4.6a), similar to that of previous report [58]. Onset of superconductivity and zero-resistance at 0 Oe were observed at 2.04 K and at 2.01 K, respectively, and the T_c decreased with increasing magnetic field. The superconducting parameters of T_c, upper critical field H_{c2} ($T = 0$ K), and coherence length ξ ($H_{c2} = \Phi_0/2\pi\xi^2$, Φ_0: the flux quantum) changed monotonically for oxidative samples as observed in magnetic measurement from 2.02 K, 574 Oe, and 75.8 nm to 2.21 K, 1864 Oe, and 42.0 nm, respectively, as summarized in Fig. 4.6b,c and Table 4.3.

Electrical transport properties in Y_2O_2Bi exhibited two-dimensional superconductivity, supporting the superconducting Bi^{2-} square net. Figure 4.7a shows voltage-current

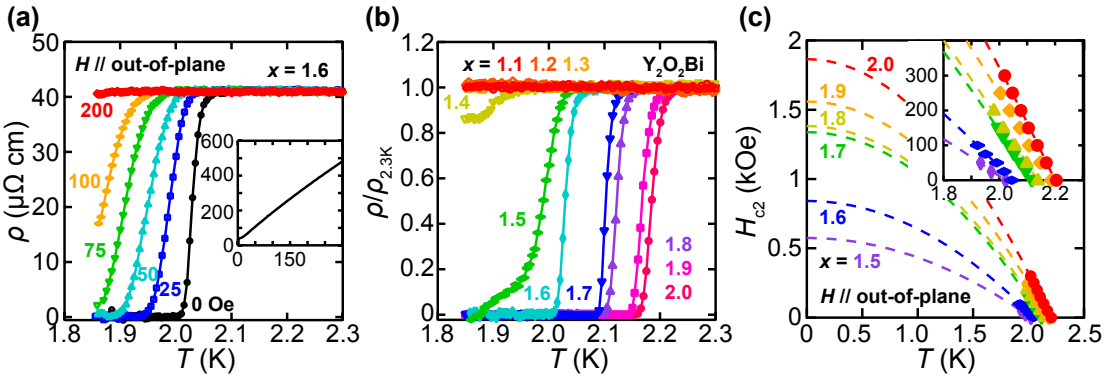

Figure 4.6: (a) The ρ-T curves near T_c and in the range of 1.85–300 K (inset) for $x = 1.6$. (b) Normalized ρ-T curves near T_c for all samples. (c) Temperature dependence of upper critical fields for $1.5 \leq x \leq 2.0$. Inset shows magnified view near T_c. Broken lines denote fitting result with Ginzburg-Landau theory $H_{c2}(T) = H_{c2}(0)[1 - (T/T_c)^2]$.

Table 4.3: Superconducting parameters for $1.5 \leq x \leq 2.0$.

x	1.5	1.6	1.7	1.8	1.9	2.0
T_c (K)	2.02	2.04	2.12	2.14	2.19	2.21
H_{c2} (Oe)	574	841	1338	1382	1559	1864
ξ (nm)	75.8	62.6	49.6	48.8	46.0	42.0

characteristics (V-I curves) near critical current around T_c. The V-I curves showed a transition of scaling law $V \propto I^{\alpha}$ above T_c from $\alpha = 1$ (ohmic law) to 3 and more with decreasing temperature. This tendency corresponded to the BKT transition at $T_{BKT} = 2.02$ K as seen in Fig. 4.7b [15,16]. This value was in good coincidence with T_{BKT} independently derived from the ρ-T curve according to the relationship $R(T) \propto \exp[-b(T/T_{BKT}-1)^{-1/2}]$, in which b is the material constant (Fig. 4.7c) [17]. These results confirmed two-dimensional superconductivity of Y_2O_2Bi, indicating weak coupling between superconducting layers, i.e., Bi^{2-} square nets, as observed in cuprate [18,19] and Fe-based [20,21] superconductors.

The two-dimensionality was also manifested in angular dependent magnetoresistance as shown in Fig. 4.8a, indicating higher H_{c2} under in-plane magnetic field. Irreproducible ρ at $\theta = 0°$ between forward and backward sweeps might be attributed to decreased effective field due to flux pinning effect in insulating $[Y_2O_2]^{2+}$ layer and/or grain boundary. Figure 4.8b shows the ρ-T curves under out-of-plane and in-plane magnetic field, demonstrating higher H_{c2} under in-plane magnetic field. This result is consistent with that of Fig. 4.8a, supporting two-dimensional superconductivity of Y_2O_2Bi.

The appearance of the two-dimensional superconductivity is probably owing to the sufficiently high crystalline orientation of large sized crystal. Figure 4.8c shows XRD patterns of powder and pellet forms for $x = 1.6$. The Y_2O_2Bi 00l diffraction peaks were

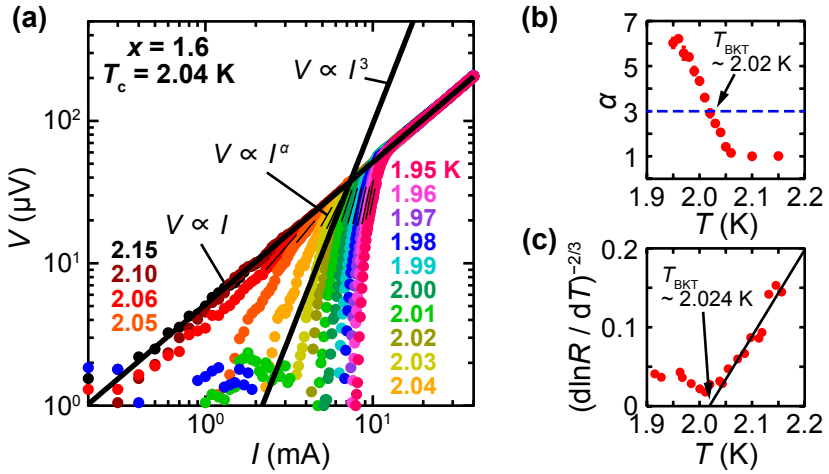

Figure 4.7: (a) V-I curves at various temperatures near T_c. Black lines denote the fitting result with $V \propto I^{\alpha}$ scaling law. (b) Temperature dependence of the exponent α. (c) Temperature dependence of $(\mathrm{d}\ln R/\mathrm{d}T)^{-2/3}$.

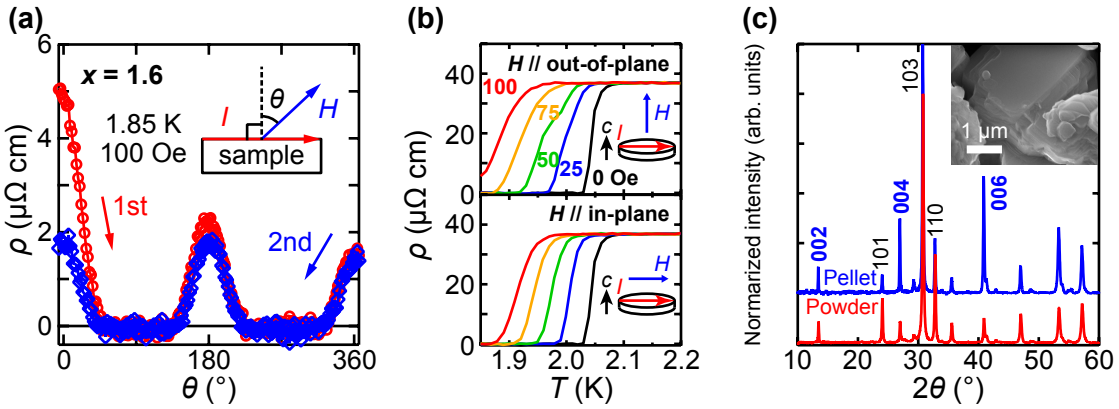

Figure 4.8: (a) Angular dependent MR at 1.85 K and 100 Oe. Inset shows measurement configuration. (b) The ρ-T curves under out-of-plane (upper) and in-plane magnetic field (bottom). The pellet surface normal corresponds to the c-axis orientation. (c) XRD patterns of pellet (blue) and powder (red) forms for $x = 1.6$, representing the preferential c-axis orientation. Inset shows scanning electron microscopy image of the pellet.

significantly enhanced in the pellet form, indicating the dominant c-axis orientation of Y_2O_2Bi crystal normal to the pellet surface. The apparently larger crystalline size than coherence length was confirmed by scanning electron microscopy (inset of Fig. 4.8c).

4.4.3 Specific heat measurement

Figure 4.9a shows the specific heat plotted as C/T vs T^2. A large jump in the specific heat was observed at T_c for each magnetic field, evidencing again the bulk superconductivity. An upturn below about 0.6 K was due to a Schottky anomaly originating from ^{209}Bi nuclei ($I = 9/2$). From the curve fitting of the normal state at 1000 Oe with the following equation, $C = \gamma_N T + \beta T^3 + \delta T^5 + AT^{-2}$, where $\gamma_N T$, $\beta T^3 + \delta T^5$, and AT^{-2} correspond to the electronic, phonon, and nuclear contributions, respectively, the Sommerfeld constant $\gamma_N = 2.71\,\mathrm{mJ\,mol^{-1}\,K^{-2}}$, $\beta = 0.582\,\mathrm{mJ\,mol^{-1}\,K^{-4}}$, $\delta = 0.0536\,\mathrm{mJ\,mol^{-1}\,K^{-6}}$, and $A = 0.325\,\mathrm{mJ\,mol^{-1}\,K}$ were obtained. From the difference in the electronic specific heat C_{el} between superconducting and normal states, the specific heat jump at T_c was evaluated to be $\Delta C_{el}/\gamma_N T_c = 1.68$ (Fig. 4.9b), which was comparable to the Bardeen-Cooper-Schrieffer weak coupling limit 1.43.

The fitting parameters obtained for the specific heat data lead to important insights. The Sommerfeld constant γ_N is directly related to the density of states at the Fermi Level, $D(\varepsilon_F)$, $\gamma = \pi 2 k_B^2 D(\varepsilon_F)/3$, where k_B is the Boltzmann constant. The value of

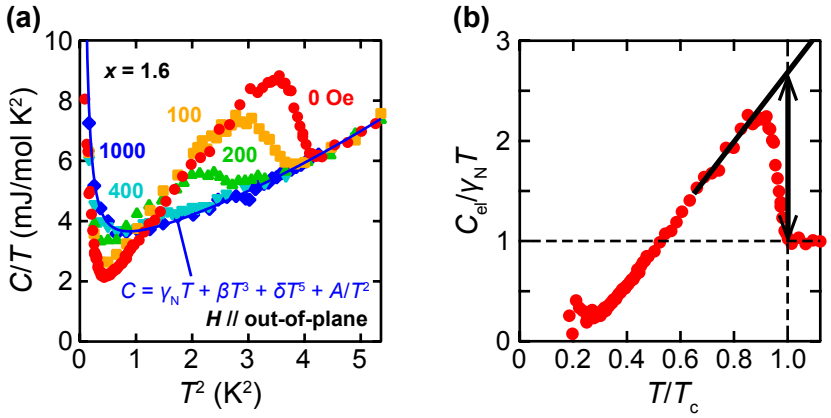

Figure 4.9: (a) The specific heat plotted as C/T vs T^2 under various magnetic fields for $x = 1.6$. (b) Electronic contribution of specific heat $C_{\rm el}$ divided by $\gamma_{\rm N}T$ as a function of normalized temperature $T/T_{\rm c}$, where specific heat jump was evaluated to be $\Delta C_{\rm el}/\gamma_{\rm N}T_{\rm c} = 1.68$ (vertical arrow). $T_{\rm c}$ was derived from the ρ-T curve.

$D(\varepsilon_{\rm F})$ was obtained as 3.4×10^{21} eV^{-1} cm^{-3}, which is quite larger than that of bismuth metal, 3×10^{16} eV^{-1} cm^{-3} [134], but smaller than that of normal metals, such as Li metal, 33×10^{21} eV^{-1} cm^{-3} [135]. The Debye temperature $\Theta_{\rm D}$ was calculated to be 256 K using the relationship $\beta = 12\pi^4 Rr/5\Theta_{\rm D}^3$, where R is the gas constant and r is the number of atoms in the chemical formula. Assuming that Y_2O_2Bi is a BCS-type superconductor, the electron-phonon coupling constant λ can be calculated from McMillan's formula [136]:

$$T_{\rm c} = \left(\frac{\Theta_{\rm D}}{1.45}\right) \exp\left(-\frac{1.04(1+\lambda)}{\lambda - \mu^*(1+0.62\lambda)}\right) \tag{4.1}$$

where μ^* is the Coulomb pseudo-potential. Supposing the value of $\mu^* = 0.13$, which is a typical value for the low $T_{\rm c}$ metals, the substitution of the experimental values of $\Theta_{\rm D} = 256$ K and $T_{\rm c} = 2.04$ K leads to $\lambda = 0.53$. The obtained λ is in the weak-coupling regime, and hence supports the analysis of the specific heat jump. The nuclear term AT^{-2} arises from the hyperfine splitting of the nuclear levels of ^{209}Bi ($I = 9/2$) due to the interaction between the nuclear quadrupole moment and the electric field gradient. Thus, the coefficient A can lead to the quadrupole coupling constant, e^2qQ, through the following equation [134],

$$A = \frac{R}{80}\frac{(2I+2)(2I+3)}{2I(2I-1)}\left(\frac{e^2qQ}{kT}\right)^2. \tag{4.2}$$

The substitution results in $e^2qQ/k = 4.13 \times 10^{-2}$ K or, in terms of the frequency, 826 MHz, which is reasonable for bismuth compounds [137–139].

The estimated thermal effective mass was $m^*_{\rm th} \approx 0.6m_{\rm e}$ calculated from the relationship $m^*_{\rm th} = m_{\rm e}\gamma_{\rm N}/\gamma_{\rm e}$, where $m_{\rm e}$ and $\gamma_{\rm e}$ are the mass and Sommerfeld constant of free-electron, respectively, indicating light conducting carriers in Bi^{2-} square net. The $\gamma_{\rm e}$ was calculated from the relationship $\gamma_{\rm e} = m_{\rm e}(N_{\rm e}/\hbar^2)(\pi/3n)^{2/3}k_{\rm B}^2$, where $N_{\rm e}$ is the number of electrons, $\hbar$ is the Dirac's constant, and n is the density of electrons. Here, we adopted $N_{\rm e} = 6 \times 10^{24}$ mol^{-1}, which was the number of carriers per 1 mole of Y_2O_2Bi estimated from the carrier density discussed later.

The specific heat data was applied to analyze the superconducting gap structure. The field dependence of electronic specific heat coefficient $\gamma(H)$ which derived from the intercept of C/T plotted by T^2, shows $\gamma(H) \propto H$ and $H^{1/2}$ dependence in full-gap and nodal superconductors, respectively [140]. In order to evaluate the relationship, the nuclear contribution AT^{-2} was subtracted from the C/T (Fig. 4.10a). The C/T became negative at the lowest temperature (inset of Fig. 4.10a), indicating the difficulty of quantitative discussion. Figure 4.10b shows preliminary analysis of electronic specific heat $C_{\rm el}$. In general, full-gap superconductor shows the following $C_{\rm el}(T)$ dependence at $T \ll T_{\rm c}$,

$$C_{\rm el}(T) = A \exp\left(-\frac{\Delta_0}{k_{\rm B}T}\right) + \gamma_{\rm n}T \tag{4.3}$$

where Δ_0 is the superconducting gap and $\gamma_{\rm n}T$ is the contribution from the non-superconducting

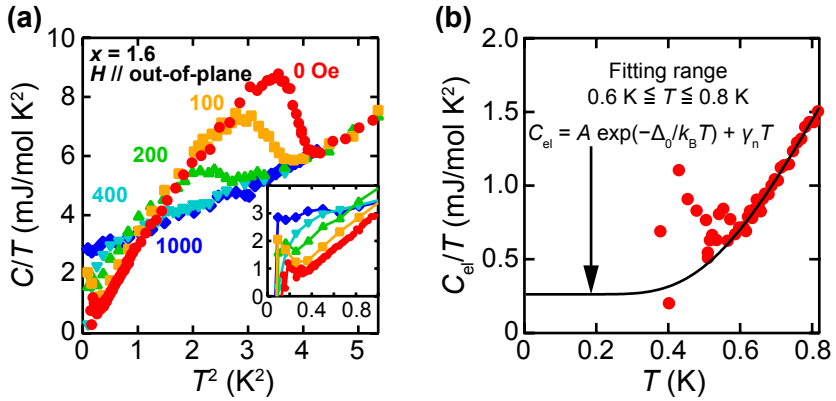

Figure 4.10: (a) T^2 dependence of C/T after subtracting nuclear specific heat. (b) Temperature dependence of electronic specific heat $C_{\rm el}$ at very low temperature. Black line denotes the fitting curve assuming full-gap model in the range of 0.6 K $\leq T \leq$ 0.8 K.

phase such as impurities. We performed above fitting in the range of 0.6 K $\leq T \leq$ 0.8 K, resulting in Δ_0 = 0.26 meV and $2\Delta_0/k_BT_c$ = 3.00, where the latter was smaller than the BCS limit of 3.54. The superconducting volume fraction derived from $1 - \gamma_n/\gamma_N$ was 90.3 %, showing good coincidence with the phase purity 96.3 mol% (Fig. 4.3b).

4.5 Mechanism of superconductivity

Carrier doping is a powerful technique to induce superconductivity. However, the similar shape of ρ-T curves and RRR irrespective to the samples ruled out the possibility of carrier doping as an effect of O incorporation. Figure 4.11a,b shows ρ-T curves and T_c vs RRR plot for non-superconducting ($1.1 \leq x \leq 1.4$) and superconducting ($1.5 \leq x \leq 2.0$) samples. Samples for $1.1 \leq x \leq 1.6$ showed similar ρ and RRR values. In addition, the ρ-T curves of all samples showed very similar shape despite more than two decades change in ρ value. These results represent that the carrier density was not significantly changed for all samples, suggesting that the O incorporation did not cause the carrier doping. The decrease in conductivity and RRR for $1.7 \leq x \leq 2.0$ with increased nominal amount of O was mainly attributed to decreased Y_2O_2Bi volume (Fig. 4.3b), and increased inter-net distance resulted in decreased inter-net conductance.

Indeed, carrier density showed almost constant values between non-superconducting and superconducting samples. Figure 4.11c shows the carrier density of high purity samples ($1.3 \leq x \leq 1.6$) derived from Hall resistance vs magnetic field at 100 K. These

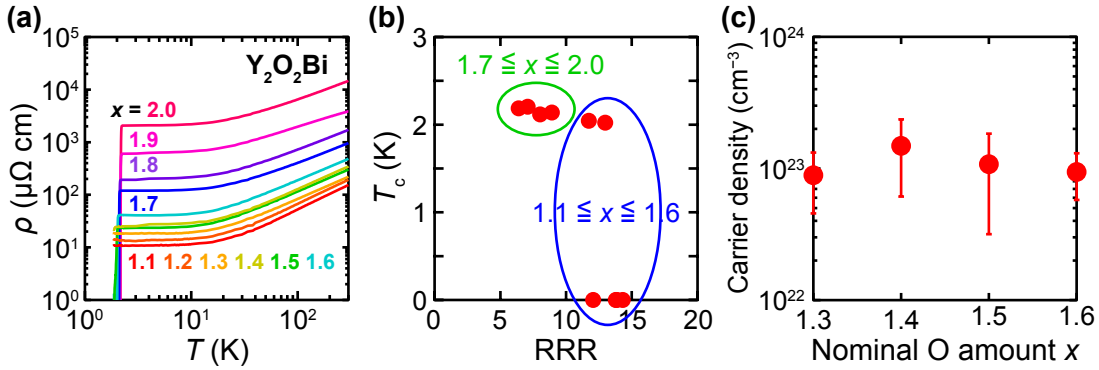

Figure 4.11: (a) The ρ-T curves and (b) T_c as a function of RRR defined as ρ(300 K)/ρ(T_c or 1.85 K) of Y_2O_2Bi samples. Samples for $1.1 \leq x \leq 1.6$ and $1.7 \leq x \leq 2.0$ are located in blue and green circles, respectively. (c) Sample dependence of carrier density derived from Hall resistance vs magnetic field at 100 K.

samples showed *p*-type conduction with rather constant carrier density ($\geq 10^{22}\,\mathrm{cm}^{-3}$) without systematic dependence of O content,[§] which is consistent with previous result [58] and electronic configuration of Bi^{2-}. Since the concentration of incorporated O has to be within several percent ($\sim 10^{20}\,\mathrm{cm}^{-3}$) considering the small *c*-axis expansion in comparison with atomic intercalation into layered compounds [141], this result indicates negligible role of the incorporated O as the carrier dopant.

Alternative scenario to induce superconductivity in Y_2O_2Bi is the enhanced two-dimensionality of the Bi^{2-} square net as a result of the abruptly expanded *c*-axis, because the expansion is concomitant with the emergence of the superconductivity for $1.5 \leq x \leq 2.0$. Figure 4.12a shows the T_c as a function of the inter-net distance d ($d = c/2$). No superconducting signatures were observed for $d \leq 6.62$ Å except for the slight resistance-drop at about 1.9 K in case of $d \approx 6.62$ Å ($x = 1.4$ in Fig. 4.6b). The partial volume superconductivity emerged at $d = 6.63$ Å with $T_c = 2.02$ K, evidenced by small shielding volume fraction (Fig. 4.5b) and broad resistance-drop ($x = 1.5$ in Fig. 4.6b). Then, the full volume superconductivity emerged for $d > 6.63$ Å with large shielding volume fraction (Fig. 4.5b) and sharp resistance-drop ($1.6 \leq x \leq 2.0$ in Fig. 4.6b). Here, T_c was approximately proportional to d. This result suggests that the superconductivity was

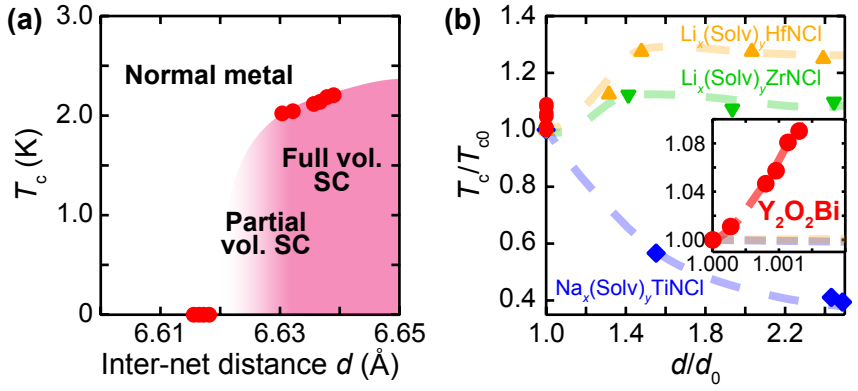

Figure 4.12: (a) Phase diagram with T_c as a function of inter-net distance $d = c/2$. Partial and full volume superconductivity was defined from the shielding volume fraction (Fig. 4.3b). (b) The evolution of T_c as a function of normalized Bi^{2-} inter-net and *M*N interlayer distance for Y_2O_2Bi and $A_x(Solv)_yMNCl$ compounds, respectively. T_{c0} and d_0 were defined from those of $x = 1.5$ in this study, and those of Li_xHfNCl, Li_xZrNCl, and Na_xTiNCl [142], respectively.

[§]Their very low Hall resistance with the significant scattering resulted in the large error bars and probably overestimation of the carrier density.

induced by reducing inter-net coupling, i.e., enhancing two-dimensionality of the Bi^{2-} square net. The emergence of superconductivity via enhanced two-dimensionality of conduction layer was scarcely seen in other superconductors, indicating that this concept would be a novel route to induce superconductivity in layered compounds.[¶]

Similar tendency of the enhanced T_c without further carrier doping was observed in $A_x(Solv)_yMNCl$ (A: alkali metals, Solv: organic molecules, and M: Ti, Zr, Hf) with increasing interlayer distance d between double honeycomb MN layers by intercalating organic molecules into the van del Waals gap [4,142,143]. Figure 4.12b shows the relative change in T_c as a function of normalized Bi^{2-} inter-net and MN interlayer distance for $Y_2O_2Bi$and $A_x(Solv)_yMNCl$, respectively. The T_c of Y_2O_2Bi increased much faster as a function of the normalized distance than those of $A_x(Solv)_yMNCl$ without saturation (inset of Fig. 4.12b), implying a peculiar feature of the superconductivity of monatomic Bi^{2-} square net.

4.6 Possible homologous series $Y_nO_nF_{n-2}Bi$ with higher T_c

Observed T_c in polycrystalline Y_2O_2Bi was around 2 K, which was slightly lower than the onset T_c in Y_2O_2Bi epitaxial thin film ($T_c \approx 4$ K, Subsection 3.3.4). Enhanced T_c with increasing Bi^{2-} inter-net distance suggests the possible formation of homologous series $Y_nO_nF_{n-2}Bi$ (Fig. 4.13) because of the incidental F doping into the film (Subsection 3.3.2). The F doping was indispensable to retain the homologous framework for $n \geq 3$ due to the charge neutrality. Same framework of blocking layer for $n = 3$ ($[Y_3O_3F]^{2+}$) was observed in $[Eu_3F_4]^{2+}$ layer of structurally similar $Eu_3F_4Bi_2S_4$ [144].

In order to synthesize Y_3O_3FBi in form of polycrystalline powder, stoichiometric amount of mixed starting materials (Bi, Y, Y_2O_3, YF_3) were heated in evacuated quartz tube at higher temperature than usual case, 1100 and 1400 °C,[‖] which was applied to

[¶]In case of ionic and molecular intercalation into van der Waals gap as reported in graphite, chalcogenides, nitride halides and so on, carrier doping or intercalated components were essential to induce the superconductivity [2], rather than increased interlayer distance.

[‖]Heating at 1400 °C caused deformation of quartz tube, suggesting higher temperature treatment would be impossible.

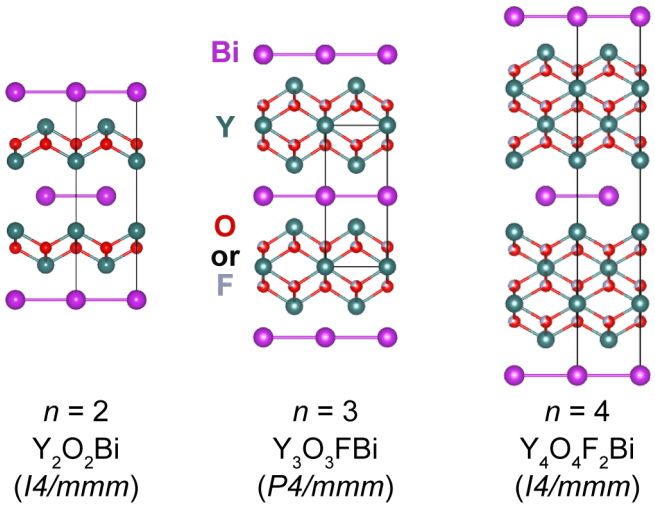

Figure 4.13: Crystal structures of homologous series $Y_nO_nF_{n-2}Bi$ ($2 \leq n \leq 4$). Black lines denote unit cells.

obtain other homologous series [145]. However, the products were just the mixture of Y_2O_2Bi, Y_2O_3, and YOF, indicating difficulty to synthesize Y_3O_3FBi in bulk form. This is consistent with the very small superconducting volume in Y_2O_2Bi epitaxial thin film. Alternative technique such as high pressure synthesis would be desired to achieve homologous series $Y_nO_nF_{n-2}Bi$ phase.

4.7 Conclusion

I succeeded in inducing superconductivity at 2 K in Y_2O_2Bi which has been already concluded as non-superconducting in previous reports. This is the fist report of superconducting Bi square net, which was evidenced by the BKT transition indicating two-dimensional superconductivity. The superconductivity emerged by increasing inter-net distance via O incorporation into hidden interstitial site without carrier doping, which was scarcely observed in other superconductors, suggesting unconventional superconducting mechanism. These concepts would be a novel route to induce superconductivity in layered compounds, shedding light on hidden superconducting compounds. The emergent two-dimensional superconductivity of Bi^{2-} square net with strong spin-orbit coupling could be associated with exotic superconductivity like topological superconductivity, leading to possible application in quantum computer.

Chapter 5

本章については、5 年以内に雑誌等で刊行予定のため、非公開。

Chapter 6

本章については、5 年以内に雑誌等で刊行予定のため、非公開。

Chapter 7

General conclusion

In this thesis, I developed novel synthetic routes for both epitaxial thin films and polycrystalline powders of R_2O_2Bi compounds in order to explore the detailed physical properties of unusual Bi^{2-} square net. These approaches enabled to discover and characterize the different fascinating phenomena from those of well-studied Bi^{-} square net in $AMBi_2$ compounds.

In the thin film study, I succeeded in obtaining Y_2O_2Bi epitaxial thin film for the first time by developing two SPE methods. Reductive SPE utilized direct reaction between (Y,Bi) powders and Y_2O_3 amorphous thin film. This method indicates that preferential reduction of Bi by strong reductant Y was essential to achieve Y_2O_2Bi phase, although surface residues hampered the fundamental evaluation of physical properties. Therefore, this concept was applied to the improved multilayer SPE method where all reaction precursors changed to thin film form, enabling the fabrication of high quality epitaxial thin films with flat surface and without any residues. The multilayer SPE method could be universally applied to obtain other R_2O_2Bi epitaxial thin films such as Ce_2O_2Bi and Dy_2O_2Bi, which will accelerate the study about Bi^{2-} square net in future. The unusual reductive state of Bi^{2-} square net was directly confirmed in Y_2O_2Bi epitaxial thin film by XPS measurement. Furthermore, strong interaction between two-dimensional electronic nature and strong spin-orbit coupling in Bi^{2-} square net was observed in electrical transport properties, demonstrating the possible emergence of topological insulating behavior in future study.

In the study about polycrystalline powders, I discovered two-dimensional super-

conductivity of Bi^{2-} square net in R_2O_2Bi compounds which was concluded as non-superconducting in previous studies. This superconductivity was universally induced in R_2O_2Bi compounds by enlarging c/a via O incorporation, which corresponded to the enhancement of two-dimensionality of Bi^{2-} square net. Furthermore, rich electronic phases appeared depending on R^{3+} in R_2O_2Bi, including the CDW instability whose presence was contradict to the previous theoretical report. The competition among superconductivity, AF ordering, and CDW in Tb_2O_2Bi suggested the unconventional superconductivity of Bi^{2-} square net. These phenomena were possibly originating from the different influence of each R^{3+} on Bi^{2-} square net. Therefore, R^{3+} substitution and c/a control were crucial to engineer the properties of Bi^{2-} square net, and R_2O_2Bi would provide intriguing platform to investigate the interplay between two-dimensional superconductivity and strong spin-orbit coupling.

The main findings in this study were the discovery of novel properties (e.g. superconductivity and two-dimensional electronic nature with strong spin-orbit coupling) and the establishment of exploring techniques (e.g. novel SPE methods and chemical control of c/a via O incorporation by CaO mixing and F substitution). The latter would be applicable not only R_2O_2Bi compounds but also other layered compounds, probably shedding the light on hidden layered compounds. Establishment of these concepts would be the most valuable result in this study because they would contribute to the progress of rich physics in layered compounds.

Appendix A

本付録については、5 年以内に雑誌等で刊行予定のため、非公開。

Appendix B

本付録については、5 年以内に雑誌等で刊行予定のため、非公開。

Appendix C

本付録については、5 年以内に雑誌等で刊行予定のため、非公開。

Appendix D

本付録については、5 年以内に雑誌等で刊行予定のため、非公開。

Acknowledgements

First of all, I would like to show my greatest appreciation to my supervisor Prof. Dr. Tetsuya Hasegawa who provided me wonderful experimental environment and incisive comments. In addition, he always encouraged me thorough the daily discussion and by taking me for drinking. Those experiences were very pleasant time for me. My study in Ph.D. course was successfully performed thanks to his tremendous support.

My deepest appreciation goes to Prof. Dr. Tomoteru Fukumura. His insightful advise and constructive suggestion always helped me to conduct experiments. Fruitful discussion with him motivated me and gave deep knowledge. Furthermore, he also gave me the great opportunity for not only the life in Sendai but also the daily fun time with alcohol. I sincerely hope that he will be careful about drinking too much.

I would like to express special thanks to Dr. Taniyuki Furuyama, Dr. Daichi Oka, Dr. Hideyuki Kawasoko, and Ms. Madoka Suzuki, who are/were the staffs in Fukumura group in Tohoku University. Thanks to them, I successfully completed my study and had a very fruitful time in Sendai.

I am also thanks to Dr. Yasushi Hirose, Dr. Akira Chikamatsu, Dr. Hideyuki Kamisaka, Mr. Shoichiro Nakao, Dr. Kei Shigematsu, Mrs. Mie Umino, and Mrs. Miki Komazawa for their useful comments and warm encouragement, who are/were the staffs in Hasegawa Group.

Special thanks to Dr. Daisuke Ogawa, Dr. Jie Wei, Dr. Shungo Kojima, Dr. Thantip S. Krasienapibal, Mr. Shun Inoue, Mr. Kenichi Kaminaga, Mr. Kyouhei Yamatake, Mr. Yutaka Uchida, Mr. Dai Kutsuzawa, Mr. Sho Shitanda, Mr. Yuichi Takahashi, Mr. Takuma Takeda, Mr. Shunsuke Shibata, Mr. Shintaro Fukuda, Ms. Fatima Zainab, Mr. Yuta Koshimoto, Mr. Daichi Saito, Mr. Yuki Saba, Mr. Kyohei Terakado, Mr. Noriyuki Ishigane, Mr. Hiroki Senmaru, Mr. Masaya Honda, Mr. Kota Matsumoto, Mr. Taku Ya-

mamoto, and Mr. Subaru Yusa for their supports in experiment and daily discussion, who are/were the members of Fukumura group in both the University of Tokyo and Tohoku University. Especially, Mr. Takeda, Mr. Shibata, Mr. Terakado, Mr. Ishigane, Mr. Honda, and Mr. Matsumoto worked together with me for the study about R_2O_2Bi compounds. I was very pleased with their help. In addition, it is a very good memory to work with drinking beer and talking about baseball at Hongo almost every night with Dr. Ogawa, Dr. Kojima, and Mr. Shibata.

I would like to express my gratitude to Ms. Mayuko Oka, Ms. Kaori Kurita, and Mr. Ryosuke Takagi who are my contemporaries at Hasegawa group. Although our studies were not so related to each other, I was very impressed when all of them gathered at Prof. Fukumura's celebration. I also thank other members of Hasegawa Group in the University of Tokyo for their persistent help.

I am deeply grateful to Prof. Dr. Hitoshi Kawaji and Dr. Suguru Kitani for their kind cooperation in conducting specific heat measurement. Thanks to them, my study has been a wonderful achievement.

I am also grateful to Prof. Dr. Masahiro Yamashita and Dr. Shinya Takaishi who lent me a glovebox for my study in Tohoku University. Thanks to them, I was able to resume the experiment about bulk polycrystalline samples from a relatively early time in Sendai.

A part of specific measurements was performed by using a facility of the Cryogenic Research Center, the University of Tokyo.

XPS measurements were performed by using a facility of Nano-Engineering Research Center, Institute of Engineering innovation, School of Engineering, the University of Tokyo.

The low temperature X-ray diffraction measurement was performed by using a facility of the Institute for Solid State Physics, the University of Tokyo. I also thanks to Dr. Takeshi Yajima for his kind help to conduct the measurement.

A part of magnetic measurements was performed by using a facility of the Center for Low Temperature Science, Tohoku University.

I would like to give special thanks to the Advanced Leading Graduate Course for Photon Sciences (ALPS) program to provide scholarship. I also thank Prof. Takeaki Ozawa who is my secondary supervisor in ALPS program for his encouragement.

Finally, I am deeply grateful to my family and friends for their understanding, moral support, and warm encouragement. Thank you very much.

References

[1] J. G. Bednorz, K. A. Müller, *Zeitschrift für Physik B Condensed Matter* **64**, 189 (1986).

[2] R. A. Klemm, *Layered Superconductors Vol. 1* (Oxford University Press, 2012).

[3] A. P. Mackenzie, Y. Maeno, *Rev. Mod. Phys.* **75**, 657 (2003).

[4] S. Yamanaka, K.-i. Hotehama, H. Kawaji, *Nature* **392**, 580 (1998).

[5] N. Reyren, *et al.*, *Science* **317**, 1196 (2007).

[6] Y. Kamihara, T. Watanabe, M. Hirano, H. Hosono, *Journal of the American Chemical Society* **130**, 3296 (2008).

[7] K. Momma, F. Izumi, *Journal of Applied Crystallography* **44**, 1272 (2011).

[8] R. J. Cava, R. B. van Dover, B. Batlogg, E. A. Rietman, *Phys. Rev. Lett.* **58**, 408 (1987).

[9] M. K. Wu, *et al.*, *Phys. Rev. Lett.* **58**, 908 (1987).

[10] H. Maeda, Y. Tanaka, M. Fukutomi, T. Asano, *Japanese Journal of Applied Physics* **27**, L209 (1988).

[11] R. Zhi-An, *et al.*, *Chinese Physics Letters* **25**, 2215 (2008).

[12] M. Rotter, M. Tegel, D. Johrendt, *Phys. Rev. Lett.* **101**, 107006 (2008).

[13] X. Wang, *et al.*, *Solid State Communications* **148**, 538 (2008).

[14] F.-C. Hsu, *et al.*, *Proceedings of the National Academy of Sciences* **105**, 14262 (2008).

[15] V. Berezinskii, *Soviet Journal of Experimental and Theoretical Physics* **32**, 493 (1971).

[16] J. M. Kosterlitz, D. J. Thouless, *Journal of Physics C: Solid State Physics* **6**, 1181 (1973).

[17] B. Halperin, D. R. Nelson, *Journal of Low Temperature Physics* **36**, 599 (1979).

[18] N.-C. Yeh, C. C. Tsuei, *Phys. Rev. B* **39**, 9708 (1989).

[19] Q. Li, M. Hücker, G. D. Gu, A. M. Tsvelik, J. M. Tranquada, *Phys. Rev. Lett.* **99**, 067001 (2007).

[20] R. Schneider, A. Zaitsev, D. Fuchs, *et al.*, *Journal of Physics: Condensed Matter* **26**, 455701 (2014).

[21] Z. Lin, *et al.*, *Scientific reports* **5** (2015).

[22] M. Tinkham, *Introduction to Superconductivity 2nd edit.* (Dover Publication, INC., 2004).

[23] G. Ghiringhelli, *et al.*, *Science* p. 1223532 (2012).

[24] J. Chang, *et al.*, *Nature Physics* **8**, 871 (2012).

[25] J. Dong, *et al.*, *EPL (Europhysics Letters)* **83**, 27006 (2008).

[26] H. Hosono, *et al.*, *Science and Technology of Advanced Materials* (2016).

[27] Y. Ando, A. N. Lavrov, S. Komiya, K. Segawa, X. F. Sun, *Phys. Rev. Lett.* **87**, 017001 (2001).

[28] L. Dubrovinsky, *et al.*, *Nature* **525**, 226 (2015).

[29] M. S. Torikachvili, S. L. Bud'ko, N. Ni, P. C. Canfield, *Phys. Rev. Lett.* **101**, 057006 (2008).

[30] M. Z. Hasan, C. L. Kane, *Rev. Mod. Phys.* **82**, 3045 (2010).

[31] Y. Ando, *Journal of the Physical Society of Japan* **82**, 102001 (2013).

[32] A. Isaeva, B. Rasche, M. Ruck, *physica status solidi (RRL)-Rapid Research Letters* **7**, 39 (2013).

[33] Y. Hor, *et al.*, *Physical review letters* **104**, 057001 (2010).

[34] S. Sasaki, *et al.*, *Physical review letters* **107**, 217001 (2011).

[35] Y.-L. Wang, *et al.*, *Phys. Rev. B* **84**, 075335 (2011).

[36] T. Shirasawa, *et al.*, *Phys. Rev. B* **89**, 195311 (2014).

[37] Z. Liu, *et al.*, *Journal of the American Chemical Society* **137**, 10512 (2015).

[38] P. Cucka, C. Barrett, *Acta Crystallographica* **15**, 865 (1962).

[39] D. Cox, A. Sleight, *Solid State Communications* **19**, 969 (1976).

[40] K. Gschneidner, J. Bünzli, V. Pecharsky, *Handbook on the Physics and Chemistry of Rare Earths*, no. vol. 36 in Handbook on the Physics and Chemistry of Rare Earths (Elsevier Science, 2006), chap. 227.

[41] R. Benz, *Acta Crystallographica Section B: Structural Crystallography and Crystal Chemistry* **27**, 853 (1971).

[42] G. Lee, M. A. Farhan, J. S. Kim, J. H. Shim, *Physical Review B* **87**, 245104 (2013).

[43] E. Brechtel, G. Cordier, H. Schäfer, *Zeitschrift für Naturforschung B* **35**, 1 (1980).

[44] A. Wang, *et al.*, *Phys. Rev. B* **94**, 165161 (2016).

[45] D.-C. Pan, Z.-M. Sun, J.-G. Mao, *Journal of Solid State Chemistry* **179**, 1016 (2006).

[46] X. Lin, W. E. Straszheim, S. L. Bud' ko, P. C. Canfield, *Journal of Alloys and Compounds* **554**, 304 (2013).

[47] F. Han, *et al.*, *Physical Review B* **88**, 144511 (2013).

[48] C. Jesus, M. Piva, P. Rosa, C. Adriano, P. Pagliuso, *Journal of Applied Physics* **115**, 17E115 (2014).

[49] C. Petrovic, S. Bud' ko, J. Strand, P. Canfield, *Journal of magnetism and magnetic materials* **261**, 210 (2003).

[50] E. M. Seibel, W. Xie, Q. D. Gibson, R. Cava, *Journal of Solid State Chemistry* **230**, 318 (2015).

[51] O. Y. Zelinska, A. Mar, *Journal of Alloys and Compounds* **451**, 606 (2008).

[52] G. Cordier, H. Schäfer, *Zeitschrift für Naturforschung B* **32**, 383 (1977).

[53] A. F. May, M. A. McGuire, B. C. Sales, *Phys. Rev. B* **90**, 075109 (2014).

[54] E. Brechtel, G. Cordier, H. Schäfer, *Journal of the Less Common Metals* **79**, 131 (1981).

[55] R. Benz, W. Zachariasen, *Acta Crystallographica Section B: Structural Crystallography and Crystal Chemistry* **26**, 823 (1970).

[56] J. Charvillat, W. Zachariasen, *Inorganic and Nuclear Chemistry Letters* **13**, 161 (1977).

[57] J. Nuss, M. Jansen, *Journal of Alloys and Compounds* **480**, 57 (2009).

[58] H. Mizoguchi, H. Hosono, *Journal of the American Chemical Society* **133**, 2394 (2011).

[59] J. Nuss, M. Jansen, *Zeitschrift für anorganische und allgemeine Chemie* **638**, 611 (2012).

[60] R. t. Shannon, *Acta Crystallographica Section A: Crystal Physics, Diffraction, Theoretical and General Crystallography* **32**, 751 (1976).

[61] E. Zintl, *Angewandte Chemie* **52**, 1 (1939).

[62] G. A. Papoian, R. Hoffmann, *Angewandte Chemie International Edition* **39**, 2408 (2000).

[63] K. Deller, B. Eisenmann, *ZEITSCHRIFT FUR NATURFORSCHUNG SECTION BA JOURNAL OF CHEMICAL SCIENCES* **31**, 29 (1976).

[64] H. Kim, C.-J. Kang, K. Kim, J. H. Shim, B. I. Min, *Phys. Rev. B* **91**, 165130 (2015).

[65] O. V. Magdysyuk, J. Nuss, M. Jansen, *Acta Crystallographica Section B: Structural Science, Crystal Engineering and Materials* **69**, 547 (2013).

[66] H. Kim, C.-J. Kang, K. Kim, J. Shim, B. Min, *Physical Review B* **93**, 125116 (2016).

[67] J. Park, *et al.*, *Physical review letters* **107**, 126402 (2011).

[68] Y. Feng, *et al.*, *Scientific Reports* **4**, 5385 (2014).

[69] K. Wang, *et al.*, *Physical Review B* **84**, 220401 (2011).

[70] A. A. Abrikosov, *Phys. Rev. B* **58**, 2788 (1998).

[71] J. He, D. Wang, G. Chen, *Applied Physics Letters* **100**, 112405 (2012).

[72] K. Wang, L. Wang, C. Petrovic, *Applied Physics Letters* **100**, 112111 (2012).

[73] K. Wang, D. Graf, C. Petrovic, *Phys. Rev. B* **87**, 235101 (2013).

[74] H. Masuda, *et al.*, *Science advances* **2**, e1501117 (2016).

[75] L. Li, *et al.*, *Phys. Rev. B* **93**, 115141 (2016).

[76] Y. Guo, *et al.*, *Physical Review B* **90**, 075120 (2014).

[77] S. J. Ray, L. Alff, *physica status solidi (b)* (2016).

[78] S. Borisenko, *et al.*, *arXiv preprint arXiv:1507.04847* (2015).

[79] W. Luo, H. Xiang, *Nano letters* **15**, 3230 (2015).

[80] M. H. Jung, A. H. Lacerda, T. Takabatake, *Phys. Rev. B* **65**, 132405 (2002).

[81] F. Han, *et al.*, *Phys. Rev. B* **92**, 045112 (2015).

[82] H. Mizoguchi, *et al.*, *Physical review letters* **106**, 057002 (2011).

[83] S.-W. Kim, *et al.*, *Journal of Applied Physics* **116**, 073901 (2014).

[84] P. Rosa, C. Jesus, C. Adriano, Z. Fisk, P. Pagliuso, *Journal of Physics: Conference Series* (IOP Publishing, 2015), vol. 592, p. 012063.

[85] Y. Fujimori, S.-i. Kan, B. Shinozaki, T. Kawaguti, *Journal of the Physical Society of Japan* **69**, 3017 (2000).

[86] X. Zhu, H. Lei, C. Petrovic, Y. Zhang, *Phys. Rev. B* **86**, 024527 (2012).

[87] R. Retzlaff, *et al.*, *Phys. Rev. B* **91**, 104519 (2015).

[88] K. Vinod, *et al.*, *Solid State Communications* **192**, 60 (2014).

[89] Z. Zołnierek, R. Troć, *Journal of Magnetism and Magnetic Materials* **8**, 210 (1978).

[90] S. Ohashi, *et al.*, *Review of scientific instruments* **70**, 178 (1999).

[91] 和佐清孝, 早川茂, スパッタ技術 (共立出版, 1988).

[92] 金原粲, スパッタリング現象　基礎と薄膜・コーティング技術への応用 (東京大学出版会, 1984).

[93] 中井泉, 泉富士夫, eds., 粉末 *X* 線解析の実際 第 *2* 版 (朝倉書店, 2009).

[94] 坪田雅己, 伊藤孝憲, *RIETAN-FP* で学ぶリートベルト解析 (情報機構, 2012).

[95] F. Izumi, K. Momma, *APPLIED CRYSTALLOGRAPHY XX* (Trans Tech Publications, 2007), vol. 130 of *Solid State Phenomena*, pp. 15–20.

[96] 日本表面科学会, ed., ナノテクノロジーのための走査プローブ顕微鏡 (丸善出版, 2002).

[97] 日本表面科学会, ed., *X* 線光電子分光法 (丸善出版, 1998).

[98] 保母敏行, ed., 高純度化技術大系 第 *1* 巻 分析技術 (フジ・テクノシステム, 1996).

[99] 日本分析化学会, ed., 分析化学便覧 (丸善出版, 2011).

[100] 日本化学会, ed., 第 *5* 版 実験化学講座 *7* 電気物性，磁気物性 (丸善出版, 2004).

[101] G. Grosso, G. P. Parravicini, 固体物理学（下） (吉岡書店, 2005).

[102] 大塚洋一, 小林俊一, eds., 丸善実験物理学講座 *(11)* 輸送現象測定 (丸善出版, 1999).

[103] 日本化学会, ed., 第 *5* 版 実験化学講座 *6* 温度・熱・圧力 (丸善出版, 2005).

[104] 物理学辞典編集委員会, ed., 物理学辞典 三訂版 (培風館, 2005).

[105] H. Hiramatsu, *et al.*, *Applied Physics Letters* **81** (2002).

[106] K. Nomura, *et al.*, *Science* **300**, 1269 (2003).

[107] T. B. Massalski, H. Okamoto, P. R. Subramanian, L. Kacrpzak, eds., *Binary Alloy Phase Diagrams 2nd edit.* (ASM International, 1990).

[108] P. L. Wang, T. Kolodiazhnyi, J. Yao, Y. Mozharivskyj, *Journal of the American Chemical Society* **134**, 1426 (2012).

[109] J. F. Moulder, W. F. Stickle, P. E. Sobol, K. D. Bomben, *Handbook of X-Ray Photoelectron Spectroscopy A Reference Book of Standard Spectra for Identification and Interpretation of XPS Data* (Physical Electronics, Inc., 1995).

[110] M. G. Morgan, M. Wang, W. Y. Chan, A. Mar, *Inorganic chemistry* **42**, 1549 (2003).

[111] O. Y. Zelinska, A. Mar, *Inorganic chemistry* **47**, 297 (2008).

[112] P. de Rouffignac, J.-S. Park, R. G. Gordon, *Chemistry of materials* **17**, 4808 (2005).

[113] M. Wang, *et al.*, *Crystal Growth & Design* **7**, 2106 (2007).

[114] Y. Mizuguchi, *et al.*, *Journal of the Physical Society of Japan* **81**, 114725 (2012).

[115] T. Koga, J. Nitta, T. Akazaki, H. Takayanagi, *Physical review letters* **89**, 046801 (2002).

[116] H.-T. He, *et al.*, *Physical review letters* **106**, 166805 (2011).

[117] L. Bao, *et al.*, *Scientific reports* **2** (2012).

[118] S. Hikami, A. I. Larkin, Y. Nagaoka, *Progress of Theoretical Physics* **63**, 707 (1980).

[119] S. Zhang, *et al.*, *Applied Physics Letters* **101**, 202403 (2012).

[120] R. Dey, *et al.*, *Applied Physics Letters* **104**, 223111 (2014).

[121] H. Tang, D. Liang, R. L. Qiu, X. P. Gao, *Acs Nano* **5**, 7510 (2011).

[122] O. Prakash, A. Kumar, A. Thamizhavel, S. Ramakrishnan, *Science* p. aaf8227 (2016).

[123] H. D. Stromberg, D. R. Stephens, *Journal of Physics and Chemistry of Solids* **25**, 1015 (1964).

[124] B. Brandt, N. I. Ginzburg, *Contemporary Physics* **10**, 355 (1969).

[125] J. Wittig, *Zeitschrift fuer Physik* **195**, 215 (1966).

[126] M. Tian, *et al.*, *Nano letters* **6**, 2773 (2006).

[127] C. Vossloh, M. Holdenried, H. Micklitz, *Physical Review B* **58**, 12422 (1998).

[128] K. Watanabe, K. Noto, N. Toyota, Y. Muto, *Journal of the Physical Society of Japan* **53**, 1444 (1984).

[129] S. Shibata, R. Sei, T. FUkumura, T. Hasegawa, *submitted* .

[130] X.-L. Qi, S.-C. Zhang, *Rev. Mod. Phys.* **83**, 1057 (2011).

[131] Y. Nakashima, H. Yui, T. Sasagawa, *Physica C: Superconductivity* **470**, 1063 (2010).

[132] N. Takeshita, T. Sasagawa, T. Sugioka, Y. Tokura, H. Takagi, *Journal of the Physical Society of Japan* **73**, 1123 (2004).

[133] Y. Kohama, *et al.*, *Chemical Physics Letters* **421**, 558 (2006).

[134] H. K. Collan, M. Krusius, G. R. Pickett, *Phys. Rev. Lett.* **23**, 11 (1969).

[135] D. L. Martin, *Proceedings of the Royal Society of London A: Mathematical, Physical and Engineering Sciences* **263**, 378 (1961).

[136] W. L. McMillan, *Phys. Rev.* **167**, 331 (1968).

[137] Y. A. Buslaev, E. Kravchenko, V. Pachomov, V. Skorikov, G. Semin, *Chemical Physics Letters* **3**, 455 (1969).

[138] C. A. Nanney, J. P. Garno, *Phys. Rev. Lett.* **28**, 1169 (1972).

[139] H. G. Robinson, H. G. Dehmelt, W. Gordy, *Phys. Rev.* **89**, 1305 (1953).

[140] G. Volovik, *ZhETF Pisma Redaktsiiu* **58**, 457 (1993).

[141] E. Morosan, *et al.*, *Nature Physics* **2**, 544 (2006).

[142] Y. Kasahara, K. Kuroki, S. Yamanaka, Y. Taguchi, *Physica C: Superconductivity and its Applications* **514**, 354 (2015).

[143] T. Takano, T. Kishiume, Y. Taguchi, Y. Iwasa, *Phys. Rev. Lett.* **100**, 247005 (2008).

[144] H.-F. Zhai, *et al.*, *Journal of the American Chemical Society* **136**, 15386 (2014).

[145] H. Ogino, *et al.*, *Applied Physics Letters* **97**, 2506 (2010).

[146] S. Baran, R. Duraj, A. Hoser, B. Penc, A. Szytuła, *Acta Physica Polonica A* **123**, 98 (2013).

[147] 近角聰信, 強磁性体の物理（上）第 *23* 版 (裳華房, 2008).

[148] D. Gignoux, D. Schmitt, *Journal of magnetism and magnetic materials* **100**, 99 (1991).

[149] C. Adriano, *et al.*, *Journal of Applied Physics* **117**, 17C103 (2015).

[150] E. DiMasi, M. Aronson, J. Mansfield, B. Foran, S. Lee, *Physical Review B* **52**, 14516 (1995).

[151] N. Ru, *et al.*, *Physical Review B* **77**, 035114 (2008).

[152] J. Hamlin, *et al.*, *Physical review letters* **102**, 177002 (2009).

[153] A. F. Kusmartseva, B. Sipos, H. Berger, L. Forro, E. Tutiš, *Physical review letters* **103**, 236401 (2009).

[154] A. A. Abrikosov, 金属物理学の基礎（上） (吉岡書店, 1994).

[155] L. D. Landau, V. Ginzburg, *Zh. Eksp. Teor. Fiz.* **20**, 1064 (1950).

[156] B. T. Matthias, E. Corenzwit, *Phys. Rev.* **107**, 1558 (1957).

[157] M. J. Winiarski, *et al.*, *Physical Chemistry Chemical Physics* **18**, 21737 (2016).

[158] M. Sturza, *et al.*, *Phys. Rev. B* **89**, 054512 (2014).

[159] D. C. Johnston, *Advances in Physics* **59**, 803 (2010).

[160] K. Kodama, *et al.*, *Physical Review B* **83**, 214512 (2011).

[161] G.-y. Adachi, N. Imanaka, *Chemical reviews* **98**, 1479 (1998).

[162] L. Balicas, *et al.*, *Phys. Rev. Lett.* **95**, 196407 (2005).